Analysis of the Sun-Earth Lagrangian environment for the New Worlds Observer

Master Thesis

Carlos Marc Alberto Deccia

Delft University of Technology

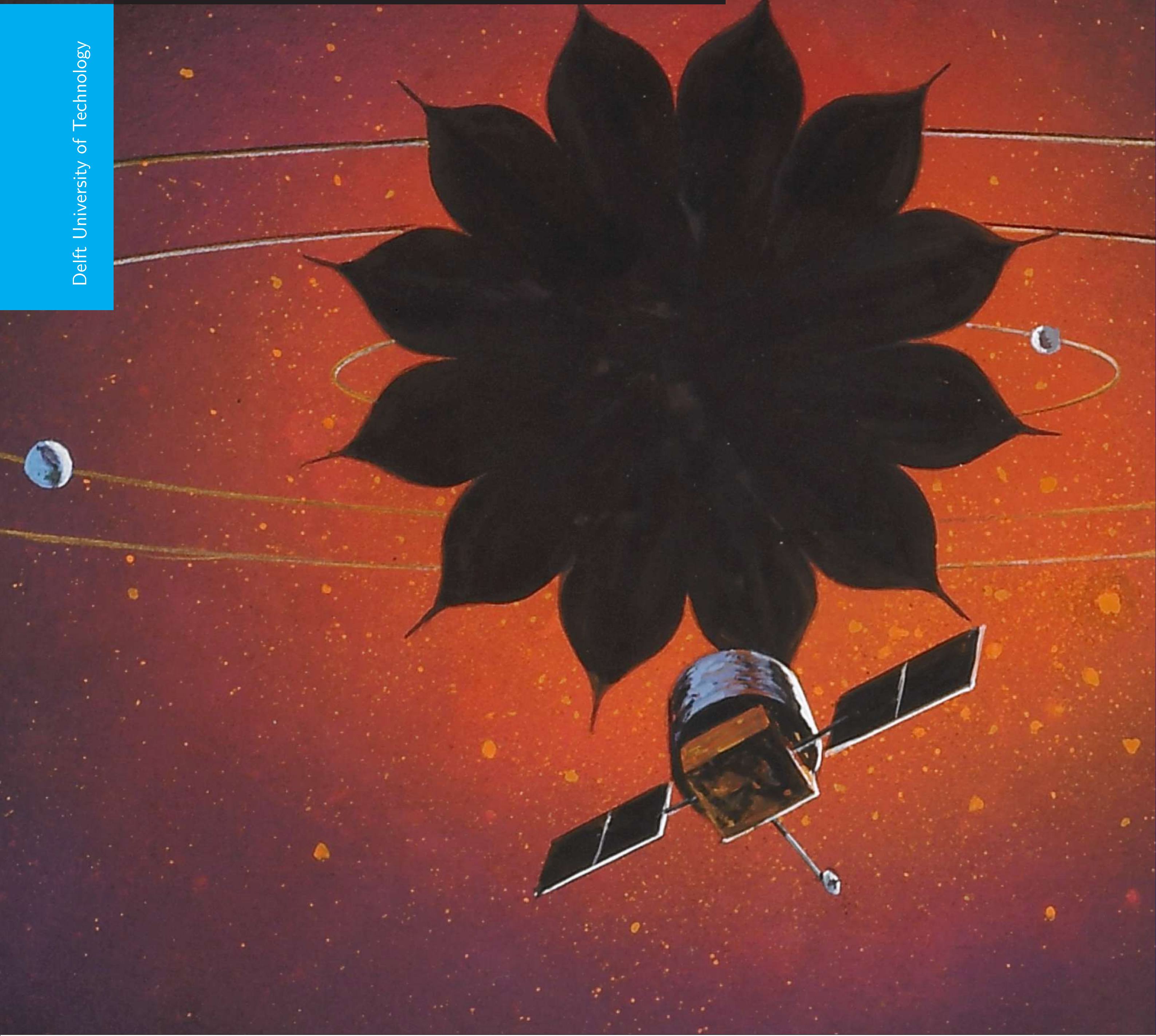

TU Delft Delft University of Technology

Challenge the future

Cover Picture: Starshade – Artist's concept of the New Worlds Observatory. The dark, flower-shaped object in the center is the star shade. 2008. Courtesy of NASA and Northrop Grumman.

Analysis of the Sun-Earth Lagrangian environment for the New Worlds Observer

Master Thesis

by

Carlos Marc Alberto Deccia

in partial fulfillment of the requirements for the degree of

Master of Science
in Aerospace Engineering

at the Delft University of Technology,
to be defended publicly on June 07, 2017 at 2:00 PM.

Supervisors:	Ir. R. Noomen,	Delft University of Technology
	Dr. J. Parker,	University of Colorado Boulder
	Dr. W. Cash,	University of Colorado Boulder
	Dr. G. H. Born,	University of Colorado Boulder
Thesis committee:	Ir. R. Noomen,	Delft University of Technology
	Dr. D. M. Stam	Delft University of Technology
	Dr. A. Cervone	Delft University of Technology
	Dr. W. Cash,	University of Colorado Boulder

Delft University of Technology

“If habitable planets are common, NWO will discover them. If life in the Universe is abundant, NWO will find it.”

— *W. Cash*

Contents

Notations

Greek symbols

α Solar exclusion angle $[rad]$

β Angle of sunlight incidence $[rad]$

γ Distance to the systems barycenter [-]

θ Angular habitable zone $[rad]$

μ Gravitational parameter $[m^3 s^{-2}]$

List of symbols

a Acceleration $[ms^{-2}]$

B Bolometric magnitude of the observed star [-]

c Speed of light (299792458) [1] [m/s]

d Distance $[m]$

L Lagrangian point $[-]$

l Length $[m]$

L Luminosity $[Js^{-1}]$

M Magnitude $[-]$

M Mass $[kg]$

m Apparent magnitude $[-]$

P Orbital period $[s]$

r Distance of the planet to the parent star $[m]$

r Radius $[m]$

r Parameter $[-]$

r Distance $[m]$

R Reflectivity $[-]$

S Area of the spacecraft that is exposed by the solar radiation pressure $[m^2]$

t Time $[s]$

U Potential function $[m^2 s^{-2}]$

V Velocity $[ms^{-1}]$

W Power density of a beam of sunlight $[W/m^2]$

x Cartesian position component in x-direction $[m]$

$\dot{x}$ Cartesian velocity component in x-direction $[ms^{-1}]$

$\ddot{x}$ Cartesian acceleration component in x-direction $[ms^{-2}]$

y Cartesian position component in y-direction $[m]$

$\dot{y}$ Cartesian velocity component in y-direction $[ms^{-1}]$

$\ddot{y}$ Cartesian acceleration component in y-direction $[ms^{-2}]$

z Cartesian position component in z-direction $[m]$

$\ddot{z}$ Cartesian acceleration component in z-direction $[ms^{-2}]$

SUBSCRIPTS

1 Primary

2 Secondary

EM Earth-Moon

g Gravitational

HBZ Habitable zone

i Inner

i Satellite

j Perturbing body

L Lagrangian point

max Maximum

n Normalized

o Outer

SE Sun-Earth

SR Solar radiation

$Star$ Star

Sun Solar

sys System

GLOSSARY

ASMCS Astrophysics Strategic Mission Concept Studies

AU Astronomical unit (149597870700 m) [2]

BOSS Big Occulting Steerable Satellite

CR3BP Circular Restricted Three-Body Problem

ICE International Cometary Explorer

ISEE-3 International Sun-Earth Explorer-3

IWA Inner Working Angle

NASA National Aeronautics and Space Administration

NIAC NASA Innovative Advanced Concepts

NWO New Worlds Observer

PCR3BP Planar Circular Restricted Three-Body Problem

RK4 Runge-Kutta 4

RK78 Runge-Kutta 7(8)

$\boldsymbol{S^3}$ Star Shade Spacecraft

STM State Transition Matrix

STS Science Telescope Spacecraft

Acknowledgements

First, I would like to thank my parents. I know that what I was working on sounded confusing at times, but I am glad you never gave up on me and helped me to keep my feet on the ground. Thank you. To Anouk and her newfound interest in space engineering.

I owe a big debt of gratitude to Ron Noomen and Eduardo Villalba. Their guidance, motivation and the ever challenging conversations, that emerged from such novel work, allowed me to better myself as a person and as a researcher. This development had a tremendous effect on my work bringing it to new levels. Ron is one of the most motivated educators I know. His approach to question everything is the one that made sure I had a rock solid basis. This is the essence of the scientific method and is not only a key for good research but can and should be applied in everyday life. I will always remember and cherish our conversations, both on this research topic as well as life in all its facets. Eduardo was the first to introduce me to the novel approach of free drift that I explore in this work. Thank you for that and for always pushing me to think out of the box.

A big thank goes to Webster Cash for his insights in the New Worlds Observer (NWO) mission proposal; your continuous motivation and excitement motivated me go to further than meets the eye.

George Born, for believing in me and for giving me the opportunity to continue my development as a researcher and Carol Born for welcoming me to Boulder like a long lost family member and for your ongoing moral support.

Last but definitely not least I would like to thank Jeff Parker, Kate Davis, Jeannette Heiligers, Collin Bezrouk, Nathan Perish and so many more. You all played, in your own way, a key component in my progress. Thank you.

1

INTRODUCTION

Exoplanets have been detected for more than 15 years. [3] In the vast majority of instances this has been accomplished through indirect observation. Such methods include among others the observation of radial velocity, transit photometry and timing variations. [4] These techniques allow for the vast majority of exoplanet detections up to date. An example for a very successful detection that has been achieved recently is the TRAPPIST-1 system. Here seven exoplanets have been detected, three of which are within the so-called habitable zone (see Section 2.3) . A comparison of this newly found system to our Solar System can be seen in Figure 1.1.

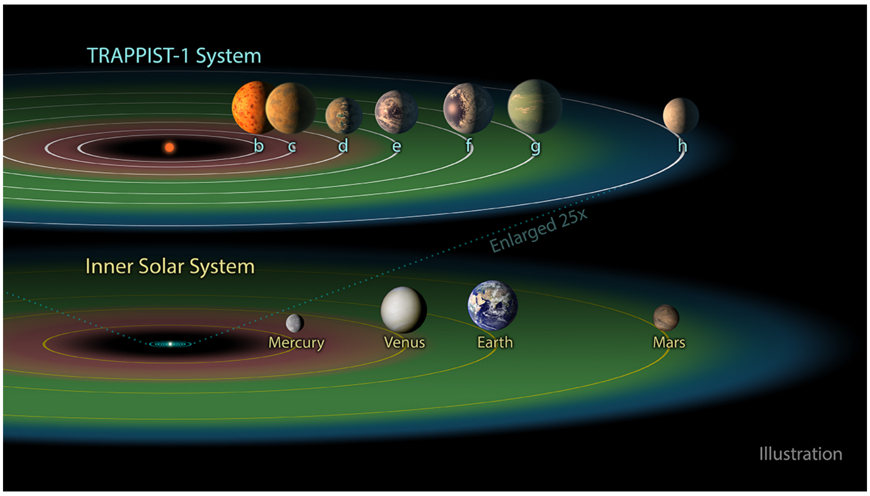

Figure 1.1: A comparison between our Solar System and the seven TRAPPIST-1 planets. The scale of the TRAPPIST-1 system has been enlarged by a factor of 25 for visualization purposes. [5]

As successful as these methods are, they rely on indirect observations of exoplanets. As part of this thesis we want to focus on planets that can potentially harbor life. Such planets are called (Earth-like) planets and are situated in the habitable zone around its parent star. Indirect methods like the ones introduced previously can provide us with estimates of a planet's size and orbit for (Earth-like) planets. Yet, the fact alone that a planet lies in the habitable zone and that it has the right size is not a guarantee but an indication of possible habitability. In order to have absolute certainty a direct analysis of the atmosphere is needed. Direct observations would allow for a first-hand spectroscopy of the atmosphere in order to search for biosignatures. [6] These biosignatures are markers created through biological processes and are indicative for life. Such elements include oxygen, ozone, nitrous oxide and methane.

The difficulty with direct observations is that the brightness of the parent star hinders the observation of an (Earth-like) planet in the same system. In order to allow for direct observations of (Earth-like) exoplanets the New Worlds Observer (NWO) has been proposed. [7] NWO is a space-based observatory that will search for (Earth-like) planets that are located in the habitable zone in neighboring stellar systems. For the purpose of this work NWO consists of two spacecraft: a 4 m aperture-diameter diffraction-limited telescope and a Starshade, which is 50 m in diameter. [7] The Starshade, also called occulter, will fly in formation with the telescope separated by a nominal distance of 70,000 km. [7] Positioned between the star observed and the telescope it casts a shadow blocking the incoming starlight to the telescope. This setup allows for the telescope to observe much fainter objects orbiting the star, which were previously not directly visible. The direction of observation of NWO has to be pointed between 45° and 105° relative to the Sun. Note that these angles are not as one would expect symmetric around the nominal situation of 90°. These limits are specified in order to avoid

These angle are required in order to avoid direct sunlight to enter the telescope and disturb the onboard navigation systems. More specifically these angles follow from the position of the startrackers and the Sunlights reflectivion of the Starshade itself. This would interfere with the observation campaign.

A further in-depth explanation on why these are the nominal angles given can be found in Section 2.4.2. As part of this thesis the Lagrangian point environment is analyzed, and how it can be used for future mission planning in context of the NWO mission proposal.

This work analyses the following research question:

"Can the dynamical environment of a lagrangian point be used to redirect the pointing vector of the NWO in order to aid in its operation during its observation campaign?"

A variety of additional reserach subquestions have been posed in order to help to answer the main question, that has been stated previously. These are:

- What constraints need to be considered when using the Starshade during observation?
- What is the effect of the constraints on the dynamical environment experienced by the spacecraft?
- What is the stability of specific NWO configurations?
- What are favorable positions and orientations to mantain the nominal NWO configuration?
- How does the ΔV change when only the Starshade or when both the Starshade and the telescope are using the dynamical environment?
- How does the use of the dynamical environment, when changing pointing target, compare to a case when it is not used?
- How much ΔV is needed to put the NWO orientation back to the nominal situation?
- How much ΔV is saved when using the dynamical environment to reorient NWO?

This includes taking all the required parameters into account in order to allow for a successful observation mission. In order to show the executed work in a structured setup, this thesis has been organized as described in the following paragraph.

After this introduction of the mission, **Chapter 2** introduces the background of the proposed NWO mission; describing both previous exoplanet detection efforts as well as the concept of the Starshade. **Chapter 3** gives an overview of the astrodynamical concepts that form the basis of this work. A special emphasis is given to the circular restricted three body problem and dynamical systems theory. In the following **Chapter 4** both the software tools and methods are introduced in order to model Lagrangian orbits as well as the reasoning behind the target selection is shown. **Chapter 5** gives a full analysis on the effect that the constraints have on the results that follow from this work; this includes a sensitivity analysis on the constraints. **Chapter 6** focuses on the velocity needed to bring the spacecraft back to nominal conditions. In this chapter the reader will be guided through an in-depth analysis of the results. Last but not least **Chapter 7** gives conclusions and recommendations that follow from this work with an overview of future applications of this thesis and possible future research branches that have been made possible from the obtained results.

2

BACKGROUND

The detection of the very first exoplanet in the early 90's around pulsar PSR B1257+12 by Alexander Wolszczan and Dale Frail [8] gave birth to an observation race similar to the days of the gold rush. Especially in the last few years a multitude of confirmed exoplanets has been detected, almost on a daily basis. Up to this date 3461 exoplanets have been detected. [9] An overview of the number of planets as well as the observation methods can be seen in Figure 2.1. Note that the year 2017 has covered the first 2.5 months only.

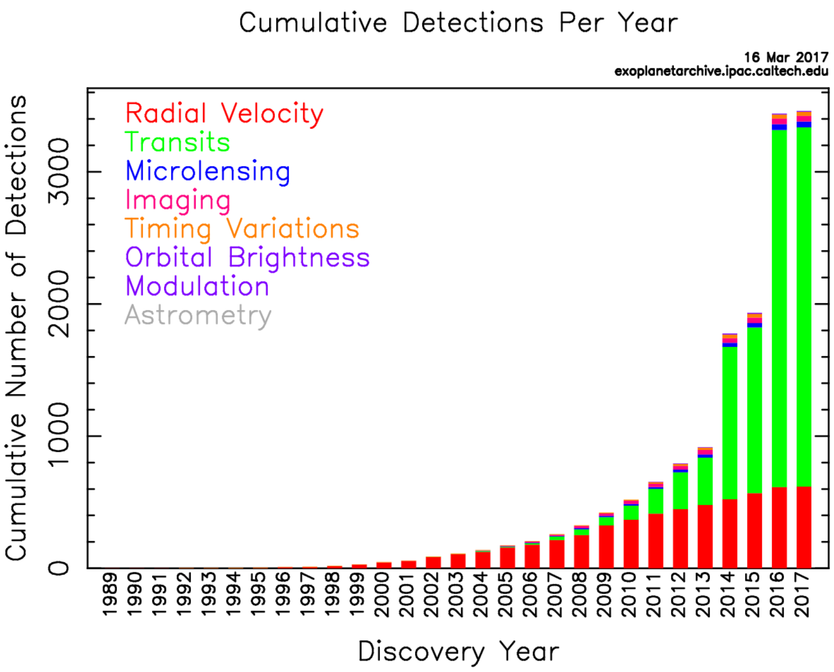

Figure 2.1: Cumulative histogram of the exoplanets discovered as a function of discovery year and detection method. [9]

The two most successful observation methods are the transit and the radial velocity method. Both of these methods use indirect observation in order to find exoplanets. The transit method uses the measurement of the decrease in luminosity due to the exoplanet passing between its parent star and the observer on Earth in order to determine both the size and the orbital period of the exoplanet. On the other hand the radial velocity detections rely on variations in radial velocity of the parent star to detect exoplanets around it. Both of these methods are limited by the precision of the instruments they use. The last decade has seen a decrease in size of possible observable exoplanets. As can be seen in Figure 2.2, the first two Earth-sized exoplanets have already been detected using the radial velocity method.

This indirect detection of Earth-sized planets is very encouraging as a first step in the search for life outside our Solar System. Yet, the detection of extraterrestrial life on exoplanets around parent stars is dependent on the observation of biomarkers such as oxygen, ozone, methane and nitrous oxide. To allow for this type of

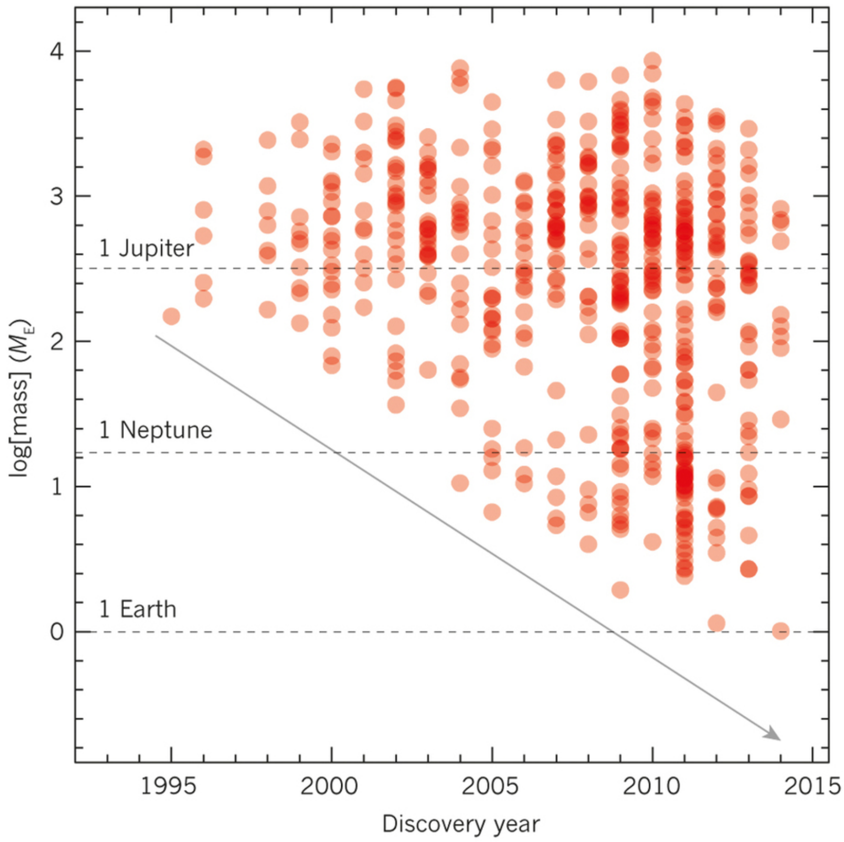

Figure 2.2: Exoplanet discoveries as a function of time using radial velocity. Each circle represent a discovered exoplanet. Darker circles stand for multiple exoplanets discovered that share similar mass characteristics. [10]

biomarker detection direct exoplanet observation is key to allow the use of spectroscopy.
An external occulter mission is a type of space mission the main focus of which is the observation of faint objects around a star outside our Solar System. This approach allows for direct observations of exoplanets and their possible biomarkers using imaging and high-contrast spectroscopy. In this work the main focus lays on the detection of Earth-like exoplanets. These are planets that can be found within the habitable zone (see Section 2.3) and are similar to Earth both in size, orbit characteristics and atmosphere. This chapter shall introduce the background of this specific direct exoplanet detection method.

2.1. OCCULTER MISSION PROPOSALS

The concept of an occulter mission is based on the use of a telescope in connection with a shade that works as an occulter. This shade obscures the starlight in order to allow for fainter objects, like planets, to be visible. The same principle appears during solar eclipses which allows for the Sun's corona to be visible from Earth. The obscuring shade should be large enough to block the incoming starlight but small enough to allow for the planets faint reflected light to reach the telescope. Therefore the size of the shade has to be larger than the telescope's aperture. A very large telescope occulter separation allows for exoplanets to be visible by supressing the incoming starlight from its parent star. A variety of occulter missions have been proposed in the past. A list with their characteristics can be found in Table 2.1.

Table 2.1: Details of direct exoplanet detection mission proposals.

Name	Proposed location	Disk diameter [m]	Telescope occulter separation [km]	Telescope aperture [m]	Earth-like planet detection range [parsec]	Reference
Unspecified	Unspecified	75	$2.5 \cdot 10^5$	10.16	< 5	[11]
BOSS	Sun-Earth L2	70	$10^4 - 10^5$	8	< 5	[12]
NWO	Sun-Earth L2	50	$70 \cdot 10^3$	4	<10	[13]

The NWO design has been proposed and selected as part of the NASA Innovative Advanced Concepts (NIAC) proposal call in 2005. [14] The proposal has been part of an Astrophysics Strategic Mission Concept Studies (ASMCS). These studies are performed by the National Aeronautics and Space Administration (NASA) in order to study the science and engineering needed to possibly fly a mission such as NWO. The efforts surrounding NWO are currently focused on decreasing the size of the occulter while keeping the same quality of scientific return. If this decrease in size can be achieved, it could lead to the deployment of multiple occulters at the same time decreasing the manuevers needed to change targets considerably.

2.2. CORONAGRAPH AND STARSHADE

The main function of a coronagraph and occulter is one and the same: to block starlight in order to allow for faint objects in the vicinity of the star to be visible. The difference lies in the location of the occulting shield. A coronagraph is fitted with an occulting shield inside the telescope. Its main use is to block the Sun's incoming light and allow to observe the corona of our star. A Starshade also uses an occulting shield but in contrast to a coronagraph it is located outside the body of the telescope. Figure 2.3 shows a sketch of how a Starshade-based NWO would observe an exoplanet. Using an external occulter like in the case of the Starshade reduces

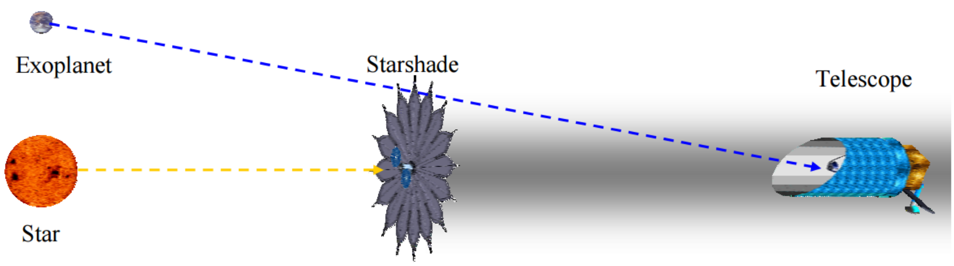

Figure 2.3: NWO concept. [7]

the incoming light to the telescope. This then decreases the background light that is scattered on the focal plane and enhances the planet detection capability. Due to the external occulter no additional optical surfaces and apertures are needed as in the case of the coronagraph. The reduction of this extra barrier reduces the scattered light further and decreases the signal lost during observations. An additional advantage of Starshade in comparison to the coronagraph is that the polishing tolerances of the primary mirror and supporting optics can be less strict in order to achieve higher contrast and fainter detection limits than can be achieved with a coronagraph. This relaxation of measurement requirements leads to a lower level of required technology development. [7]

2.3. HABITABLE ZONE SIZE

The area interesting for Earth-like planet detection is typically named the habitable zone. This area around a star is directly related to where the temperature emanated by the star would allow for liquid water to be found. In addition to the star's luminosity, planetary atmosphere and geological processes have an influence on the habitability of a planet. [15] For a first-order analysis the habitable zone can be defined as limited by the orbits of Venus and Mars as shown in Equation 2.1. This equation is based on the distances from the Sun where liquid water can be stable. These equations inherently assume that water is necessary for the development of life on a planet. This might not be necessarily the case for extraterrestial life. Yet, for a first-order analysis this is a valid assumption.

$$\begin{aligned} r_{i,HBZ} &= 0.7 \cdot \sqrt{\frac{L_{Star}}{L_{Sun}}} \\ r_{o,HBZ} &= 1.5 \cdot \sqrt{\frac{L_{Star}}{L_{Sun}}} \end{aligned} \tag{2.1}$$

Here $r_{i,HBZ}$ and $r_{o,HBZ}$ represent the inner and outer radii of the habitable zone expressed in astronomical unit (AU), whereas L_{Star} and L_{Sun} are the luminosity of the observed star and our Sun respectively. The introduced AU allows the magnitude of the distances to be easier quantified. A small star-planet angular separation allows for the telescope to resolve planets that have a semi-major axis of up to 0.5 AU. This allows for high-contrast direct imaging of Earth-like planets. This is achieved by starlight suppression of several orders of magnitude while not obstructing incoming light of planets residing at small angular separations. In this way all planets beyond the Inner Working Angle (IWA), which is defined by the minimum angular separation, are visible to the telescope. The starlight suppression is the fraction of incident starlight that enters the telescope. This has been observed in experimental setups to be between 10 and 100 times less than the planet contrast limit, which defines the least brightest planet that can be observed next to a star. [16] In order to compute the IWA, the linear expression Equation 2.1 has been transformed into an angular relation in Equation 2.2. Here θ represents the angular HBZ size and can be expressed in terms of the apparent magnitude alone [16], r_{HBZ} is the average radius of the habitable zone, d is the distance to the observer and $M_{B,Star}$ and $M_{B,Sun}$ the bolometric magnitude of the observed star and of the Sun respectively.

$$\theta = \frac{r_{HBZ}}{d} = \frac{\sqrt{\frac{L_{Star}}{L_{Sun}}}}{d} = \frac{\sqrt{10^{-\left(\frac{M_{B,Star}-M_{B,Sun}}{5}\right)}}}{d} \tag{2.2}$$

If we assume that $M_{B,Star}$ is approximately equal to $M_{B,Sun}$, then we can make use of the approximation given in Equation 2.3.

$$M_{B,Star} = m - 5log(d) - 5 \tag{2.3}$$

This leads to the rule of thumb in Equation 2.4 with m being the apparent magnitude of the observed star. The angle θ resulting from this equation is expressed in milliarcsecond.

$$\theta \approx 10^{-\frac{m}{5}} = 10^{-\frac{6.5}{5}} = 0.501as \tag{2.4}$$

When making use of this rule of the thumb in Equation 2.4 the apparent magnitude of star that can be observed for an inner working angle of 50 mas is of $m \approx 6.5$.

This selection allows for the visibility of at least part of the habitable zone of over 500 possible targets, which are mostly F, G and K stars. These are the most similar to our own Sun. This would increase the chances to find

Earth-like planets. [16] The inner working angle required to gain visibility of the habitable zone is described by Equation 2.5. Here r stands for the distance of the planet to the parent star and d for the distance of the system to the observer. This parameter is independent of the telescopes aperture. As can be seen from Equation 2.5 the IWA required for an exoplanet observation is linearly dependent on the distance of the same exoplanet to its parent star.

$$\text{IWA} = sin\left(\frac{r}{d}\right) \approx \left(\frac{r}{d}\right) \tag{2.5}$$

As an example we select a star at a distance d of 10 parsec, where one parsec is equal to $3.086 \cdot 10^{16}$ m. [17] When using an IWA of 0.05 arcsec the closest planet that can be observed is at a distance of 0.5 AU from its parent star, as shown in Equation 2.6. Using the same equation and mantaining the IWA at 0.05 arcsec we can compute that for a system that is 30 parsec far from ours we can directly observe up to a distance of 1.5 AU from its parent star, which is the edge of our Solar Systems habitable zone.

$$r = 0.05\ arcsec \cdot 10pc = 0.5AU \tag{2.6}$$

This means that planets orbiting any Star that is located within 10 parsec can be observed up to a distance of 0.05 AU from its parent star. This allows for a complete observation of the habitable zone provided that they have a star similar to our Sun. For stellar systems that are up to 30 parsecs away NWO can resolve the observations up to a distance of 1.5 AU. This allows for observations of stellar systems up to 30 parsecs of at least part of their habitable zone.

2.4. HARDWARE

A preliminary study determined the hardware characteristics that follow from the mission requirement of IWA of 50 mas for the Starshade-based NWO mission. The proposed concept includes a telescope with a mirror of 4 m in diameter and Starshade that is 50 m in diameter. The nominal size of the Sun-Earth L2 Lagrangian point orbit has been selected to be 800000 km with a Starshade-telescope separation of 70000 km. [16] This mission design will be used as a baseline for this thesis. The one change that has been made from this baseline mission design is the selection of a high-thrust propulsion system instead of a low-thrust one. This choice has been mainly done due to the higher power available at a moments notice of the high-thrust system. This might be useful in order to counteract the non-linear dynamical environment at Sun-Earth L2. The NWO mission concept is composed of two main elements; the Science Telescope Spacecraft (STS) and the Star Shade Spacecraft (S^3). The following Sections 2.4.1 and 2.4.2 shall give a brief overview on some of the hardware characteristics that define each spacecraft.

2.4.1. SCIENCE TELESCOPE SPACECRAFT

The use of the Starshade approach decouples the aperture of the Science Telescope Spacecraft (STS) needed from the IWA. In order to give a first-order analysis on the required aperture size a series of simulations has been executed on a pole-on view of our Solar System at a distance of 10 parsec. The results can be seen in Figure 2.4. Here the aperture has been varied from 1.2 up to 10 m. In the case of 1.2 m the zodiacal light hinders all possible resolution needed for planetary detection. The zodiacal light originates from the reflection of the starlight on the ice and dust that lies in the ecliptic plane of the Solar System. With an increasing aperture the effects of the zodiacal light diminish allowing for a distinct detection of a simulated Earth-like planet, which is represented as the pale blue dot. A selection of a 10 m telescope would give stunning images. Yet, it is unlikely that such a telescope will be ready in the next decade. [18] Therefore the choice has fallen to the 4 m telescope which is a reasonable trade-off for a telescope that can be available in the next 10 years. A preliminary study showed that the primary mirror of the STS can be both produced as a monolithic piece or as a multi-piece mirror. A final selection on the mirror type has not been made yet. [7] The aperture size of the telescope is not constrained by the specifications of the IWA nor of the collection area, but is rather dependent on the ability of the telescope to resolve Earth-like planetary objects.
Figure 2.5 shows a preliminary design of such an STS. Here the STS bus connects the telescope to the solar arrays that provide power to the spacecraft. The STS has a Sun shade in order to be able to point closer to the Sun without having rays of sunlight enter the mirror and hinder the observation process.

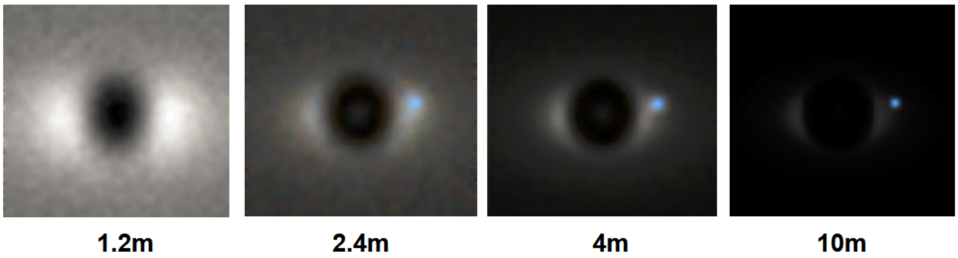

Figure 2.4: Simulation of a varying telescope aperture from 1.2 to 10 m on a 10 parsec star system analogous to ours viewed pole-on. The white interfering brightness is due to the zodiacal light. [7]

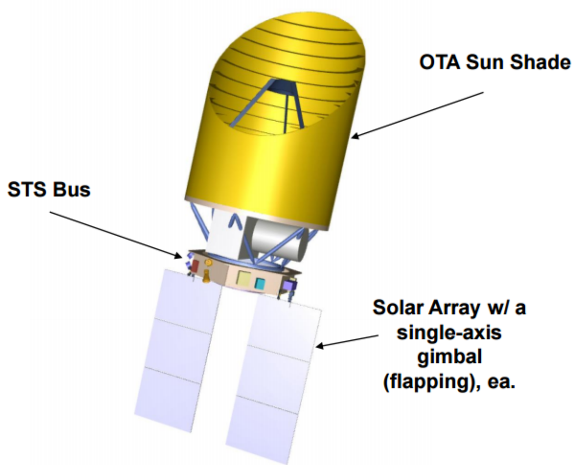

Figure 2.5: Preliminary design of a 4 m STS. [7]

2.4.2. Star Shade Spacecraft

In the context of this thesis the Star Shade Spacecraft will be refered to using the abbreviation S^3 or simply as Starshade. This spacecraft is the key characteristic of the NWO mission proposal. A deployed image of the Starshade can be seen in Figure 2.6. Four years of simulations have determined the optimal number of petals to be 16 and the shape of the Starshade petals to be the one shown in Figure 2.6. [7] The main reason for this number and shape is to minimize the diffraction of incoming star light at the edges of the Starshade.

If this effect of diffraction would have not been taken into consideration, the Starshade would need to increase in size and be situated further away from the observer in order to achieve similar results. This design developed by Webster Cash in 2006 [13] allows for the decreased size of the Starshade occulter when compared to the other proposed designs (see Section 2.1). This results in a 10^9 starlight suppression factor in order to allow for an unblocked view on the habitable zone of a neighbouring star system at a distance of 10 parsec. [7]

The Starshade orientation relative to the Sun and the telescope is restricted by two angles as seen in Figure 2.7. The first is the orientation of the Starshade relative to the Sun. No observations shall be taken at solar exclusion angles (α) lower than 45°. These requirements have been set so that the Sun light would not interfere during comunication and observation mission phases. The angle of 45° relative to the Sun follows from a constraint due to the startrackers position on the Starshade. By constraining the Starshade to have a relative Sun incidence angle of lower than 45°, this prevents the startrackers from being obstructed by incoming sunlight and can therefore operate continuously. For the case of angles of α between 45° and 90° the Starshade rotates in order to be always perpendicular to the pointing vector as can be seen in Figure 2.7.

In preliminary analysis [7] when the angle α reaches values beyond 90° it has been decided not to rotate the Starshade perpendicular to the pointing vector. This has been chosen in order to avoid the possibility of sunlight to reflect from the Starshade into the telescope aperture. This lack of rotation can be seen in Figure 2.7. This gives unsymmetric angle constraints relative to a nominal angle α of 90°.

The formation between STS and S^3 has a nominal relative distance of 70000 km. Due to the lack of rotation of the Starshade for angles α beyond 90°, the Starshade's allowable pointing error margin will dictate the limit-

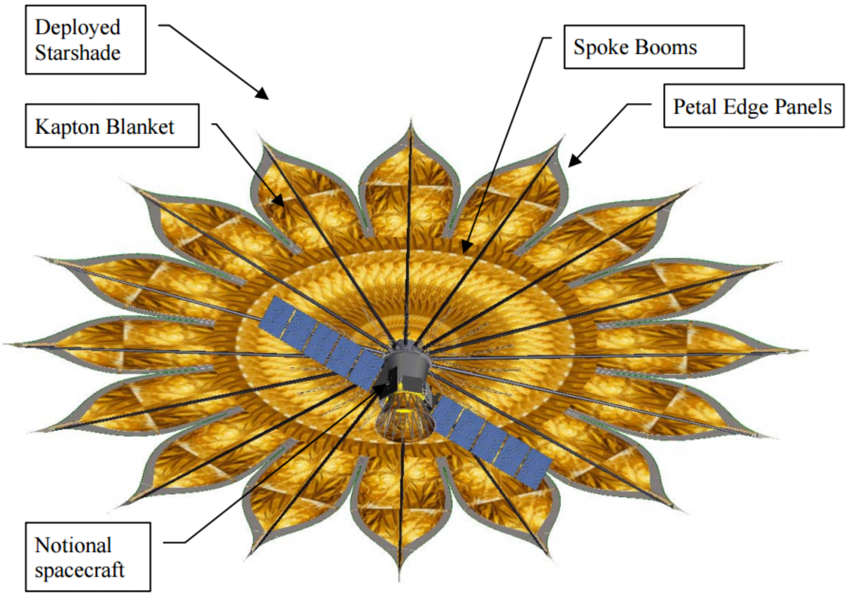

Figure 2.6: Preliminary design of a 16 petal 50 m S^3. [7]

ing angle constraint. The pointing direction to the Starshade allows for an allowable pointing error margin of 15°. Within this error margin useful observations can be made. And due to the Starshade's parallel position to the Sun-Earth-L2 line possible reflections of the Sun's lightrays into the STS should be prevented. From these two limiting factors previous preliminary studies [7] have set the boundaries of acceptable angles for α at 45° and 105° from the Sun-Earth-L2 line. The angle of 105° follows from the addition of 15° to a nominal angle α of 90° in relation to the Sun-Earth-L2 line. These given angles from the previous study on NWO as part of an exoplanet detection mission are given as shown in Figures 2.8 and 2.9.

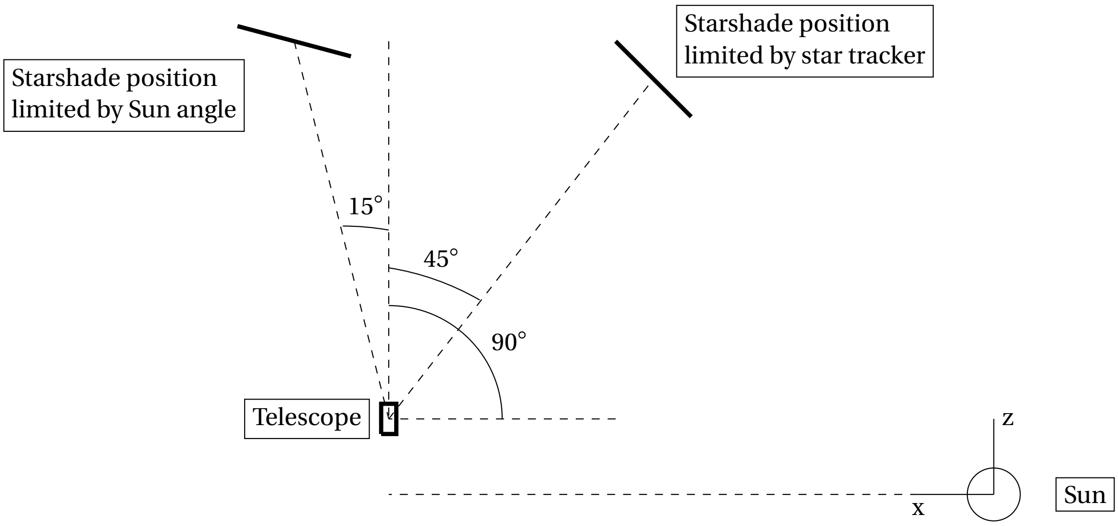

Figure 2.7: Sketch representing the relative Starshade angle constraints to the nominal case of α equal 90°. The x-axis coincides with the Sun-Earth-L2 line. The origin of the angles shown in this figure are at the telescope itself. The figure is not to scale, but a sketch to give further clarification on the constraining angles.

An overview of these parameters can be seen in Figure 2.8. For a better overview of these constraints an overview in an inertial frame is given in Figure 2.9. The Starshade has a dark side that is pointed towards the telescope in order to avoid interfering reflections of star light that might originate behind the telescope. The front side of the Starshade is covered with a blanket of kapton to provide for thermal insulation. This shall prevent excessive temperature gradients on the Starshade satellite.

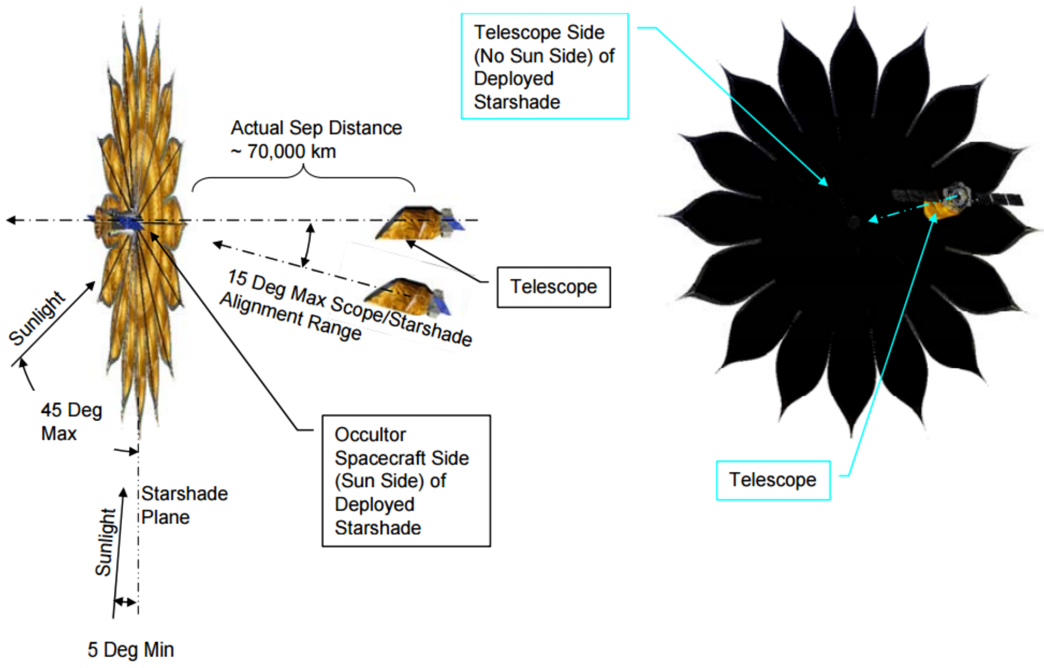

Figure 2.8: Relative alignment angle margin errors of the Starshade relative to the telescope. [7]

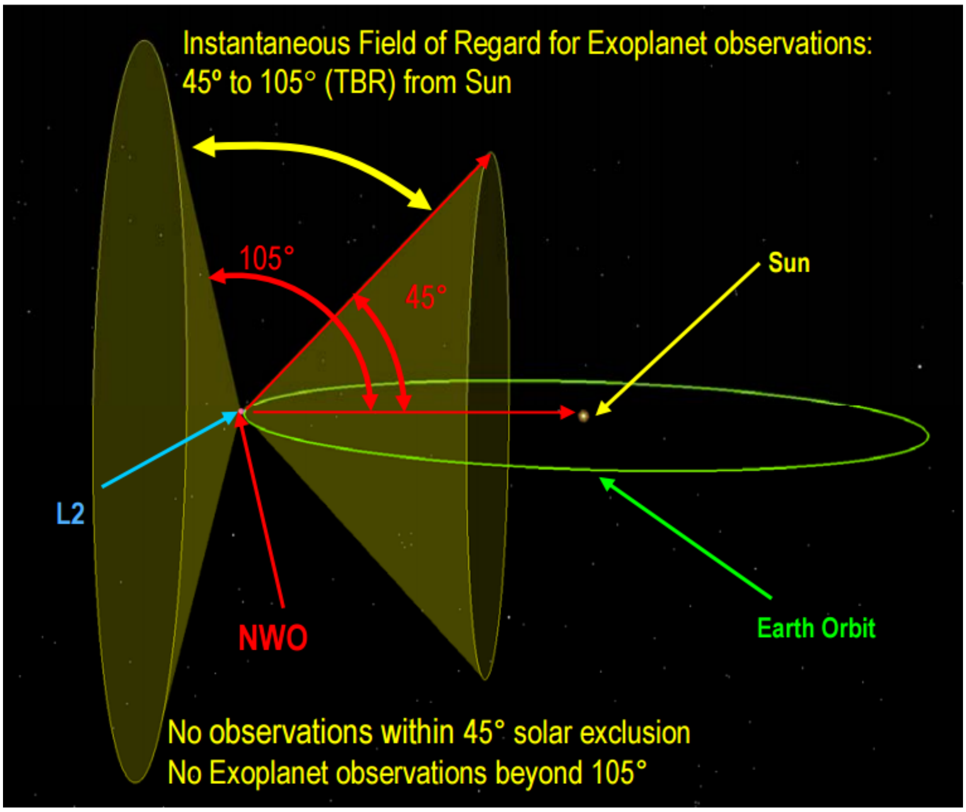

Figure 2.9: Relative observation angle margins of the Starshade relative to Sun's position. [7]

2.4.3. FORMATION FLYING SENSORS

NWO's formation is required to stay aligned during observations within ±1 m orthogonal relative to the direction of observation. The error margin in the direction of the line of sight is ±20% of the nominal distance of 70000 km. In order to allow such high precision in cross-track direction three sensors shall be used: RF tracking, an astrometric sensor and a shadow sensor. The RF tracking gives a coarse alignment correction information that brings the relative position within 50 km. The astrometric sensor reduces that uncertainty up to 2 m with information to allow for medium-sized steps. Lastly the shadow sensor provides information for the fine alignment correction up to 0.1 m. [16] These steps are presented in Figure 2.10. Due to the high relative position accuracy required, low-acceleration environments such as Sun-Earth and Earth-Moon Lagrangian points are an ideal candidate for this mission proposal. A further investigation on these points is given in Chapter 3.

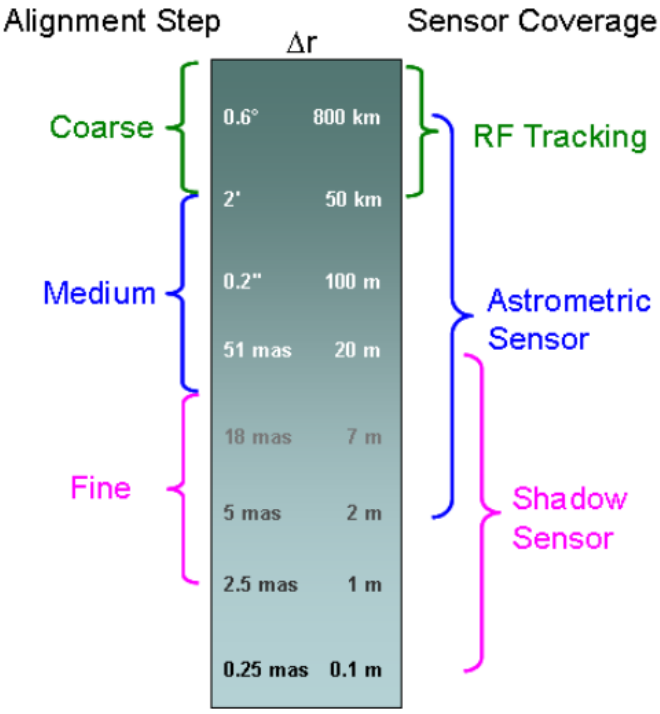

Figure 2.10: Relative alignment capabilities of the on-board sensors. [7]

2.5. CONCLUSIONS

This chapter gave an overview on the NWO and its baseline mission characteristics. The presented design for a low-thrust NWO mission was designed for a 800000 km Sun-Earth L2 orbit with a relative separation of 70000 km. The size of the Starshade is 50 m in diameter whereas the telescope has a 4 m diameter mirror. This configuration allows to detect Earth-like planets in a 10 parsec distance system up to 0.5 AU from its parent star, which is well inside the relative habitable zone. For more distant stars part of the habitable zone can still be visible. The Starshade's position perpendicular to the pointing vector of the telescope has to be within ±1 m, but can vary ±20% in the pointing vector direction. This position is ensured with the use of on-board instruments. Due to this high sensitivity low-acceleration environments such as Lagrangian points are ideal for this mission design. The original design used low-thrust propulsion in order to change the pointing direction of NWO from one target star to the next.

3

ASTRODYNAMICS

This chapter will give an overview of the fundamental concepts of astrodynamics used in the progress of this work. Starting with a description of the assumptions on the reference frames and coordinates sets used, the equations of motion that describe the Circular Restricted Three-Body Problem (CR3BP) have been setup. Finally the Lagrangian points location and the relevant periodic orbits shall be analyzed.

3.1. ASSUMPTIONS

In a three-body problem, three bodies are considered. Their motion can be predicted if their masses and initial states, which constitute position and velocity, are known. In this setup the bodies are considered point masses and the only acting forces are the ones that the bodies exert on each other, i.e. gravitational forces only. The equations of motions can be derived starting from Newton's second law of motion and its law of gravitation. For the case of a CR3BP it is further assumed that one of the three bodies, in this case the spacecraft, is much smaller than the other two. This leads to the assumption that the gravitational attraction of the much smaller body on the other two massive bodies can be neglected. When comparing the mass of a spacecraft with that of a moon or a planet this is a valid assumption. Additionally the two massive bodies are assumed to rotate in circular bodies around the barycenter of the system. [19]

3.2. REFERENCE FRAMES AND COORDINATE SYSTEMS

For this work two reference frames are utilized: the pseudo-inertial and the rotational reference frame. A graphical representation can be found in Figure 3.1. The axes ξ, η and ζ represent the pseudo-inertial refer-

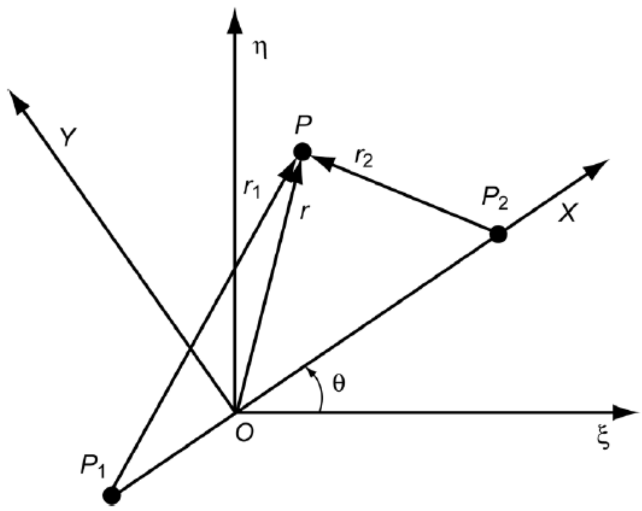

Figure 3.1: Inertial and rotating reference frames in the circular restricted three-body problem. [19]

ence frame, whereas the axes X,Y and Z define the rotational frame. The point P in Figure 3.1 represents the third body which is in our case a spacecraft in a Sun-Earth or Earth-Moon system, with neglegible mass. The origin of both reference systems coincides in the barycenter of the system: point O. The dominant masses of this system are defined as P1 and P2. These move in the XY-plane. Their motion is described by a constant angular velocity $\omega = \frac{d\theta}{dt}$. The angle θ describes the angular orientation between the axes X and ζ as shown in Figure 3.1. The distances r_1 and r_2 represent the distances from the spacecraft located in point P from the main masses P1 and P2 respectively. The distance of the spacecraft relative to the origin is designated by r.

3.2.1. NORMALIZATION

All used parameters in the CR3BP have been normalized using the following unitary values:

- The distance between the main masses P1 and P2
- The sum of the masses P1 and P2
- The rotation rate of the system

All mentioned values will have the value of one except for the orbital period of the system which will acquire the value of 2π. In order to dimensionalize non-dimensional values Equations 3.1 are used.

$$\begin{aligned} l_n &= \frac{l}{d_{sys}} \\ t_n &= \frac{t}{P_{sys}} \cdot 2\pi \\ V_n &= \frac{V \cdot P_{sys}}{d_{sys} \cdot 2\pi} \\ a_n &= \frac{a \cdot P_{sys}^2}{d_{sys} \cdot 4\pi} \end{aligned} \tag{3.1}$$

These equations clarify the normalization of length (l), time (t), velocity (V) and acceleration (a). The subscript n defines one of the previously mentioned parameters in normalized form. d_{sys} represents the distance between the primary and secondary body P1 and P2. Depending on the case this can vary (e.g. Earth-Moon or Sun-Earth). Finally P_{sys} defines the orbital period of the system selected.

3.3. CIRCULAR RESTRICTED THREE BODY PROBLEM

The assumptions mentioned in Section 3.1 lead to the creation of the CR3BP. Due to the near-circularity of the bodies' motion these assumptions model the regarded systems to a highly appropriate degree. The CR3BP functions as a basis for the evaluation of the trajectories developed. The simplifications applied to the motion of the system, in which the spacecraft operates, allow for a quick identification of useful trajectories. In this next subsection the necessary equations of motions shall be described.

3.3.1. EQUATION OF MOTIONS

In order to express the equations of motion in the CR3BP we make use of three expressions in Equation 3.2. These show the representation for the value of μ, r_1 and r_2 that will be used later on in Equation 3.3. The parameter μ stands for the system mass parameter, whereas the values of r_1 and r_2 are, as shown in Figure 3.1, the distances of the spacecraft to the primary and secondary body. The CR3BP dynamics depend only on the system-dependent body constant μ. This constant is composed of M_1 and M_2, which are the masses of the primary and secondary bodies respectively.

$$\begin{aligned} r_1 &= \sqrt{(x+\mu)^2 + y^2 + z^2} \\ r_2 &= \sqrt{(x-1+\mu)^2 + y^2 + z^2} \\ \mu &= \frac{M_2}{M_1 + M_2} \end{aligned} \tag{3.2}$$

The expression of the standard equations of motion that describe the CR3BP can be seen in Equation 3.3. Here $\ddot{x}$, $\dot{x}$ and x represent the acceleration, velocity and position in reference to the x-axis. For y and z an analogous representation has been chosen.

$$
\begin{aligned}
\ddot{x} &= 2\dot{y} + x - \frac{1-\mu}{r_1^3}(\mu + x) + \frac{\mu}{r_2^3}(1-\mu-x) \\
\ddot{y} &= -2\dot{x} + y - \frac{1-\mu}{r_1^3}y - \frac{\mu}{r_2^3}y \\
\ddot{z} &= -\frac{1-\mu}{r_1^3}z - \frac{\mu}{r_2^3}z
\end{aligned}
\tag{3.3}
$$

Equation 3.3 can be reformulated in a more concise formulation as stated in Equations 3.4 and 3.5. Here U represents a scalar potential function.

$$
U = \frac{x^2 + y^2}{2} + \frac{1-\mu}{r_1} + \frac{\mu}{r_2}
\tag{3.4}
$$

The partial differential of Equation 3.4 gives the expressions in Equation 3.5. These expression will be useful in Section 4.2 when developing the single-shooting algorithm that is used to numerically create trajectories in the Lagrangian environment.

$$
\begin{aligned}
\ddot{x} &= \frac{\partial U}{\partial x} + 2\dot{y} \\
\ddot{y} &= \frac{\partial U}{\partial y} - 2\dot{x} \\
\ddot{z} &= \frac{\partial U}{\partial z}
\end{aligned}
\tag{3.5}
$$

3.4. LAGRANGIAN POINTS

In the CR3BP there are five locations of equilibrium, where $\ddot{x} = \ddot{y} = \ddot{z}$. These are called Lagrangian points, also sometimes referred to as libration points. The points will be named in this work as follows. For a CR3BP that considers the Sun and Earth as the primary massive objects the nomenclature used is $SE - L_{1-5}$. In the case of a CR3BP in the Earth-Moon system $EM - L_{1-5}$ shall be used.

3.4.1. LOCATION OF LAGRANGIAN POINTS

In this section the computation of the exact Lagrangian point location with respect to their primary bodies shall be evaluated. To find the location of the libration points the position partials of Equation 3.5 will be set to zero as stated in Equation 3.6.

$$
\frac{\partial U}{\partial x} = \frac{\partial U}{\partial y} = \frac{\partial U}{\partial z} = 0
\tag{3.6}
$$

This simplifies Equation 3.3 to Equation 3.7.

$$
\begin{aligned}
0 &= x - \frac{1-\mu}{r_1^3}(\mu + x) + \frac{\mu}{r_2^3}(1-\mu-x) \\
0 &= \left(1 - \frac{1-\mu}{r_1^3} - \frac{\mu}{r_2^3}\right) y \\
0 &= \left(-\frac{1-\mu}{r_1^3} - \frac{\mu}{r_2^3}\right) z
\end{aligned}
\tag{3.7}
$$

In the CR3BP the distances are by definition positive and the mass of point P1 is defined to be bigger than P2. Therefore it can be assumed that $\mu \leq \frac{1}{2}$. Considering that the only way in which Equation 3.7 can be fulfilled is if z is equal zero, this leads to the conclusion that all libration points are located in the xy-plane. For the value of y there are two solutions; $y = 0$ and $y \neq 0$. This leads to two sets of libration points. The first set with $y = 0$ are due to their location on the x-axis defined as collinear points. These are named L_1, L_2 and L_3. L_1 is located between the two bodies P1 and P2. L_2 can be found on the far side of the secondary body P2 in relation to the systems barycenter. L_3 on the other hand is located opposite to P2 in relation to the systems barycenter. The second set are named L_4 and L_5. These points are located in equilateral triangles relative to

Table 3.1: The locations of the five Lagrange points in the Sun–Earth and Earth–Moon circular three-body systems. The positions are given in non-dimensional normalized units and kilometers with respect to the barycenter of the system. All z components for all Lagrangian points are equal zero and have therefore been excluded from this table. [20]

Lagrange point		Normalized position [-]		Un-normalized position [km]	
		x	y	x	y
Sun-Earth	$L1$	0.9899859823	0	148099795.0	0
	$L2$	1.0100752000	0	151105099.2	0
	$L3$	-1.0000012670	0	-149598060.2	0
	$L4$	0.4999969596	0.8660254038	74798480.5	129555556.4
	$L5$	0.4999969596	-0.8660254038	74798480.5	-129555556.4
Earth-Moon	$L1$	0.8369151324	0	321710.177	0
	$L2$	1.1556821603	0	444244.222	0
	$L3$	-1.0050626453	0	-386346.081	0
	$L4$	0.4878494157	0.8660254038	187529.315	332900.165
	$L4$	0.4878494157	-0.8660254038	187529.315	-332900.165

the primary and secondary body P1 and P2, see Figure 3.2. The locations of the $SE - L_{1-5}$ and $EM - L_{1-5}$ are given in Table 3.1 for both a normalized case as well as in km.
The position of the Earth-Moon libration points and of the $SE - L_1$ and $SE - L_2$ are shown in Figure 3.2.

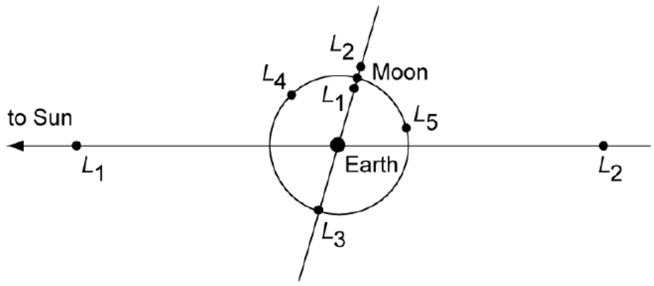

Figure 3.2: Positions of all Lagrangian points in the Earth-Moon system and the Sun-Earth libration points $SE - L_1$ and $SE - L_2$ (to scale). [19]

3.4.2. PERIODIC MOTION IN THE VICINITY OF A COLLINEAR LAGRANGIAN POINT

This current section shall describe the three different orbits that can be obtained around any of the collinear Lagrangian point L_1, L_2 or L_3. Due to the geometry of their location and in order to maximize times of observations while following the pointing limitations relative to greater bodies such as Sun, Earth and Moon only $EM - L_2$, $EM - L_3$ and $SE - L_2$ will be considered. $EM - L_1$, $EM - L_4$ and $EM - L_5$ and their corresponding points in the Sun-Earth system have been excluded since in their configurations Earth and Moon are not collinear, with the location of the Lagrangian point at the end of it. This automatically decreases the field of celestial sphere that can be observed if the pointing requirements described in Chapter 2 are to be fulfilled. $SE - L_3$ has been excluded because of its extended communication delays due its large distance from the Earth. The periodic motions around Libration point henceforth analyzed are the lyapunov, lissajous and halo orbits.

LYAPUNOV ORBITS

Lyapunov orbits are periodic and planar orbits. They follow from a first-order solution of the equations of motion in the CR3BP. A spacecraft following such an orbit would travel clockwise along it. A graphical representation can be found in Figure 3.3.
Their planar shape is not ideal for the case of the Starshade mission since the formation of the Starshade and the telescope will be able to only observe stars that are in the same plane of the lyaponov orbits, since they are only restricted to the same orbital plane. This would exclude any stars that are not in that plane, significantly decreasing the number of stars that are possible to be observed with this orbit selection.

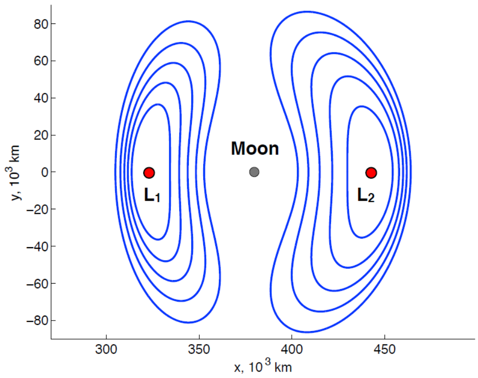

Figure 3.3: $EM - L_1$ and $EM - L_2$ lyaponov orbits. [21]

LISSAJOUS ORBITS

Unlike lyapunov orbits, lissajous orbits have an out-of-plane component in the CR3BP. Their behavior is not periodical, but only quasi-periodical as can be seen in Figure 3.4. This is due to a mismatch in out-of-plane and in-plane frequencies. Even though their xy-plane behavior can be periodic, their z-directional movement is not. This orbit instability means that a slight deviation from the equilibrium conditions will lead to an increasing divergence from its nominal conditions over time. An additional number of station-keeping maneuvers needs therefore to be implemented if this case were to be chosen.

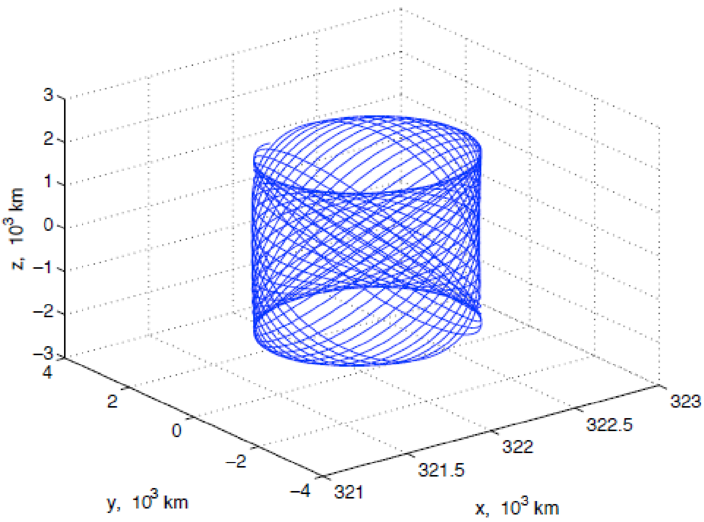

Figure 3.4: Lissajous orbits. [21]

HALO ORBIT

Halo orbits are both periodic and as can be seen in Figure 3.5, have a component in the z-direction. The previously mentioned mismatch between out-of-plane and in-plane frequencies is not the case for Halo orbits. This allows for a periodic solution in the CR3BP. This behavior makes them very interesting for exoplanet detection missions such as Starshade.

Halo orbits are divided into two major groups: northern and southern Halo orbits. Northern Halo's have for the majority of their orbit a positive value for their z-parameter. Southern Halo's on the other hand have a negative z-parameter for the majority of their orbit. Another interesting characteristic of Halo's is that the closer their x-parameter is to the Moon the larger is also their vertical z-component. Both of these behaviors can be seen in Figure 3.6.

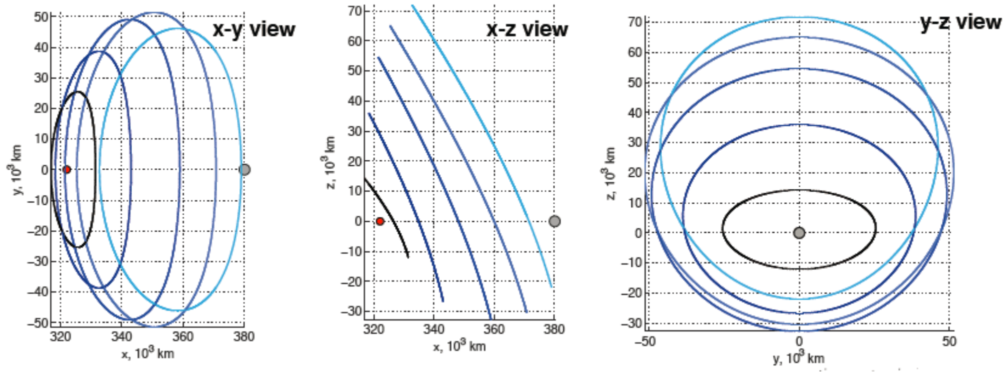

Figure 3.5: Family of northern $EM - L_2$ Halo orbits. [21]

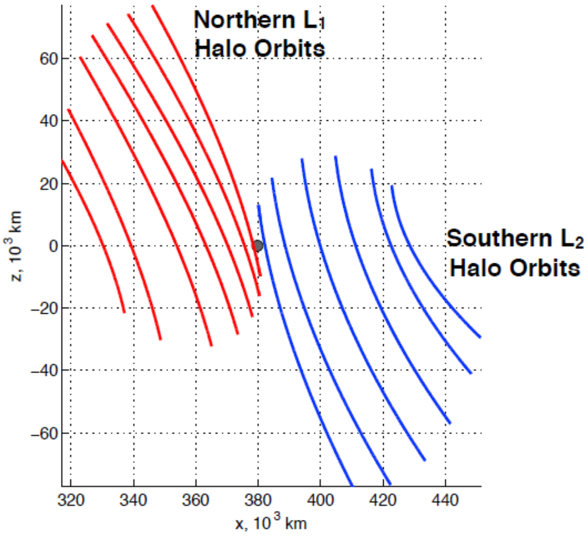

Figure 3.6: Northern $EM - L_1$ and southern $EM - L_2$ and Halo orbits. The grey circle in the center of the figure represents the Moon. [21]

3.5. PERTURBING FORCES

The motion of a celestial object is influenced by various perturbing forces. In this subsection the most relevant ones shall be briefly explained.

3.5.1. THIRD-BODY PERTURBATION

Third-body perturbations are accelerations that follow from the gravitational effect that bodies of the Solar System have on each other. In order to analyze if the incurred perturbation is large enough to be considered, it shall be computed using Equation 3.8. Here the index i defines the satellite and j the perturbing body. All distances r are with respect to the barycenter of the system that is being analyzed, whereas r_{ij} is the distance between the satellite and the perturbing body.

The variable $\bar{a}_g$ characterizes the acceleration of the third-body that is defined by using the gravitational parameter μ_j. For this first-order analysis all points have been assumed to be in the xy-plane. The perturbation has therefore been computed at the Lagrangian points rather than on an orbit around them. To give an estimate on the worst-case scenario, that a spacecraft experiences regarding third-body perturbations, $|a_g,max|$ has been computed for the perturbing bodies of the Sun and Moon in the cases of $SE - L_2$, $EM - L_2$ and $EM - L_3$. The results from this analysis are given in Table 3.2. The constants used can be found in reference material. [19]

$$\bar{a}_g = \mu_j \left(\frac{\bar{r}_j - \bar{r}_i}{r_{ij}^3} - \frac{\bar{r}_j}{r_j^3} \right) \tag{3.8}$$

Table 3.2: Acceleration of the Sun, Earth and Moon on a spacecraft at the $SE-L_2$, $EM-L_2$ and $EM-L_3$ points.

Location	$\bar{a}_g[m/s^2]$		
	Sun	Earth	Moon
$SE-L_2$	2.336E-04	7.0181E-10	3.370E-07
$EM-L_2$	3.721E-05	7.3589E-05	3.509E-05
$EM-L_3$	3.234E-05	3.2344E-05	3.895E-07

3.5.2. SOLAR RADIATION PRESSURE

A spacecraft orbiting around the Sun experiences a radiation force caused by the impact of the Sun's photons, called solar radiation pressure. The equation that describes this acceleration is given by Equation 3.9, where a_{SR} stands for the perturbing acceleration due to solar radiation pressure, R the reflectivity, W the power density of the beam of sunlight, S the area of the spacecraft that is exposed to the solar radiation, c the speed of light, M the mass of the object and β the incidence angle of the sunlight.

$$a_{SR} = (1+R)\frac{W\cdot S}{c\cdot M}cos^2(\beta) \tag{3.9}$$

For m we estimate a spacecraft mass of 5000 kg [7] whereas R has the value of 1 in their respective units are assumed, whereas for β a maximum of 45° and for S 1963.5 m^2 follows from the diameter of 50 m set due to the characteristics of the Starshade [7]. Using these inputs the approximations for the solar radiation pressure in the vicinity of the Lagrangian points can be computed as stated in Table 3.3.

Table 3.3: Solar radiation pressure on Earth, $SE-L_2$, $EM-L_2$ and $EM-L_3$.

Location	$a_{solarradiation}[m/s^2]$
$SE-L_2$	4.493E-11
$EM-L_2$	4.612E-11
$EM-L_3$	4.608E-11

3.5.3. TOTAL PERTURBATION

As seen in Sections 3.5.1 and 3.5.2 a spacecraft in orbit at the Lagrangian points is perturbed by solar radiation pressure and third-body perturbations. The solar radiation pressure has the same magnitude for all three considered collinear libration points. When considering third-body perturbations we see that the perturbating accelerations originating from third-bodies in the Earth-Moon Lagrangian points are higher than in the Sun-Earth system. Due to the difference in magnitude between these two perturbing forces the third-body perturbations are the driving accelerations, see Table 3.4. In order to further analyze the movement of the spacecraft along the natural gradient of the Lagrangian point, the point with the lowest acceleration, $SE-L_2$, has been selected for further analysis.

Table 3.4: Total perturbing acceleration on an spacecraft at the collinear libration points $SE-L_2$, $EM-L_2$ and $EM-L_3$.

Location	Perturbing object	$\bar{a}[m/s^2]$
$SE-L_2$	Moon & Solar rad.	3.370E-07
$EM-L_2$	Sun & Solar rad.	3.721E-05
$EM-L_3$	Sun & Solar rad.	3.234E-05

4
METHODS

In this chapter we will first give an overview of the method used to create Lagrangian point orbits and a differential correction algorithm. Following this a new method shall be introduced called free drift. This shall be used in order to investigate whether the NWO concept can make extensive use of the non-linear dynamics of the system at hand. One of the first researchers to analyze the possibility of designing a Lagrangian-based mission was Farquhar. [22] Due to a lack of a general solution a semi-analytical method was developed. [23, 24] This lead to the development of the first libration-based mission, International Sun-Earth Explorer-3 (ISEE-3). [25] This satellite was intended for magnetospheric research and therefore located between Earth and Sun, at $SE-L1$ as can be seen in Figure 4.1.

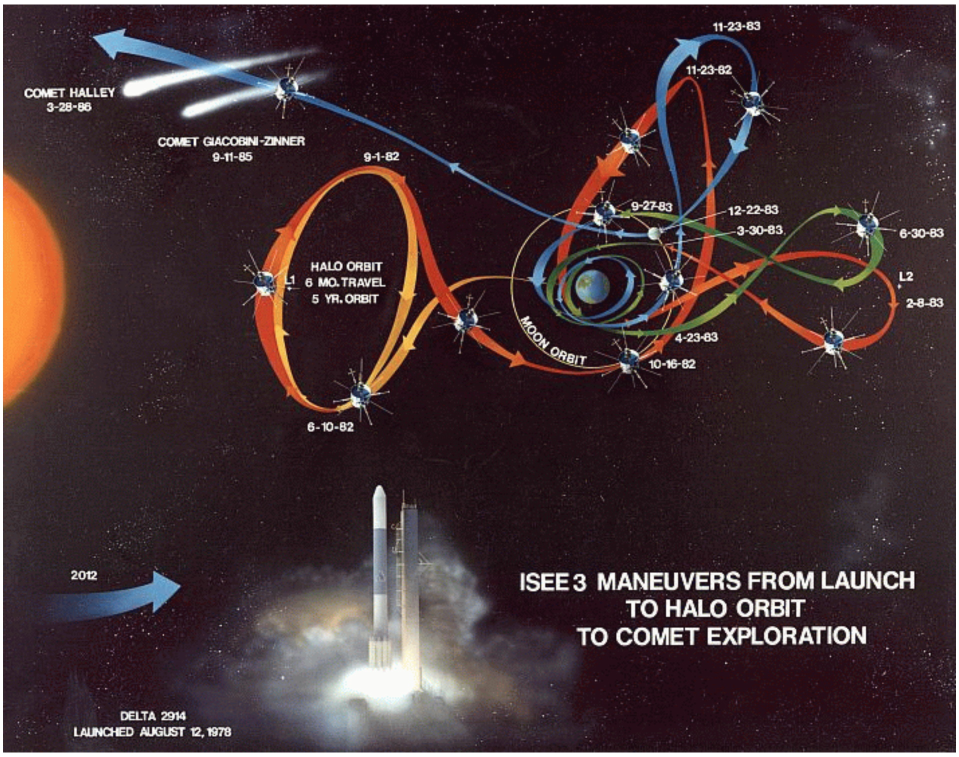

Figure 4.1: Manuveuring sequence to take International Cometary Explorer (ICE) from the Sun Earth L1 point to its encounters with Comets Giacobini-Zinner and Halley. Artist rendition of the mission ISEE-3. [26]

Using linear analysis it has been possible to predict periodic and quasi-periodic orbits. Third-order approximations in combination with the Lindstedt-Poincaré method allow for further insights in the behavior of these type of orbits. [23] Since the method developed by Richardson [25] is an approximation a more precise method needs to be used. Due to the highly non-linear behavior around the Lagrangian points, higher-precision methods need an initial estimation of the points that are to be evaluated. For this purpose the solution by Richardson can be used as an input for such a higher-precision method, like a differential correction approach. This produces then the desired orbit to the degree of accuracy required for a realistic mission design.

4.1. RICHARDSON-CARY APPROXIMATION

Linearizing Equation 3.3 gives Equation 4.1. This solution shows a periodic nature. The motion of x and y are coupled and independent of z. On the other hand the motion in z is simply harmonic and not related to both x and y.

$$\begin{aligned} \ddot{x} - 2\dot{y} - (1+2c_2)x &= 0 \\ \ddot{y} + 2\dot{x} + (c_2 - 1)y &= 0 \\ \ddot{z} + c_2 z &= 0 \end{aligned} \tag{4.1}$$

Here c_2 is a constant coefficient expressed in Equation 4.2 with γ_L being the representation of the normalized distance from the analyzed Lagrangian point to the barycenter of the system.

$$c_2 = \left[\frac{1-\mu}{(1 \pm \gamma_L)^3} + \frac{\mu}{\gamma_L^3} \right] \tag{4.2}$$

When solving Equation 4.1 a solution can be found, in Equation 4.3. Here A_x and A_z characterize the amplitudes, λ and ν the frequencies and ϕ and ψ the phase angles of the in-plane and out-of-plane motion.

$$\begin{aligned} x &= -A_x cos(\lambda t + \phi) \\ y &= kA_x sin(\lambda t + \phi) \\ z &= A_z sin(\nu t + \psi) \end{aligned} \tag{4.3}$$

A Halo-type orbit is generated when the frequencies ν and λ are equal. [24] This is the case when the amplitudes A_x and A_z are large enough for nonlinear contributions to make the eigenfrequencies ν and λ equal. A third-order approximation of the Planar Circular Restricted Three-Body Problem (PCR3BP) for a periodic orbit is then found using the Lindstedt-Poincaré method. [27] Even though the Richardson approach using the Lindstedt-Poincaré method leads to good first-order results numerical issues at higher-order expansions reduce the viability of this method for high accuracy and precision applications. In Section 4.2 a numerical approach shall be shown which allows for higher order of accuracy and precision.

4.2. DIFFERENTIAL CORRECTION

This section explains the numerical method called differential correction. It can be used to numerically generate a Halo orbit and to build trajectories around Lagrangian points. The method for this numerical integration is called the single-shooting algorithm. Due to the highly unstable region around the Lagrangian points the shooting method needs quite an accurate initial guess in order to be able to propagate a state. The Richardson method described in Section 4.1 provides for such an estimate. The process described in this section follows the procedure explained by Parker and Anderson. [28]

SINGLE-SHOOTING ALGORITHM

In this numerical approach the State Transition Matrix (STM) is applied to adapt the initial conditions in order to satisfy a certain convergence to the required solution. As a first step let the state be defined as a vector containing all state variables as shown in Equation 4.4.

$$\mathbf{X} = \begin{bmatrix} x \\ y \\ z \\ \dot{x} \\ \dot{y} \\ \dot{z} \end{bmatrix} \tag{4.4}$$

The STM in Equation 4.5 is a 6x6 matrix that includes all the partial derivatives of the state. The initial state of the STM has the form of an identity matrix as shown in Equation 4.6.

$$\boldsymbol{\Phi}(t,t_0)=\frac{\partial\mathbf{X}(t)}{\partial\mathbf{X}(t_0)}=\begin{bmatrix}\frac{\partial x}{\partial x_0} & \frac{\partial x}{\partial y_0} & \frac{\partial x}{\partial z_0} & \frac{\partial x}{\partial \dot{x}_0} & \frac{\partial x}{\partial \dot{y}_0} & \frac{\partial x}{\partial \dot{z}_0}\\ \frac{\partial y}{\partial x_0} & \frac{\partial y}{\partial y_0} & \frac{\partial y}{\partial z_0} & \frac{\partial y}{\partial \dot{x}_0} & \frac{\partial y}{\partial \dot{y}_0} & \frac{\partial y}{\partial \dot{z}_0}\\ \frac{\partial z}{\partial x_0} & \frac{\partial z}{\partial y_0} & \frac{\partial z}{\partial z_0} & \frac{\partial z}{\partial \dot{x}_0} & \frac{\partial z}{\partial \dot{y}_0} & \frac{\partial z}{\partial \dot{z}_0}\\ \frac{\partial \dot{x}}{\partial x_0} & \frac{\partial \dot{x}}{\partial y_0} & \frac{\partial \dot{x}}{\partial z_0} & \frac{\partial \dot{x}}{\partial \dot{x}_0} & \frac{\partial \dot{x}}{\partial \dot{y}_0} & \frac{\partial \dot{x}}{\partial \dot{z}_0}\\ \frac{\partial \dot{y}}{\partial x_0} & \frac{\partial \dot{y}}{\partial y_0} & \frac{\partial \dot{y}}{\partial z_0} & \frac{\partial \dot{y}}{\partial \dot{x}_0} & \frac{\partial \dot{y}}{\partial \dot{y}_0} & \frac{\partial \dot{y}}{\partial \dot{z}_0}\\ \frac{\partial \dot{z}}{\partial x_0} & \frac{\partial \dot{z}}{\partial y_0} & \frac{\partial \dot{z}}{\partial z_0} & \frac{\partial \dot{z}}{\partial \dot{x}_0} & \frac{\partial \dot{z}}{\partial \dot{y}_0} & \frac{\partial \dot{z}}{\partial \dot{z}_0}\end{bmatrix} \tag{4.5}$$

$$\boldsymbol{\Phi}(t_0,t_0)=\boldsymbol{I}_{6x6} \tag{4.6}$$

To propagate the STM Equation 4.7 is used, where the matrix $A(t)$ is defined in Equation 4.8.

$$\dot{\boldsymbol{\Phi}}(t,t_0)=\boldsymbol{A}(t)\boldsymbol{\Phi}(t,t_0) \tag{4.7}$$

$$\boldsymbol{A}(t)=\frac{\dot{\boldsymbol{X}}(t)}{\boldsymbol{X}(t)} \tag{4.8}$$

When in the CR3BP the matrix $\boldsymbol{A}(t)$ can be expressed as in Equation 4.9. The matrices $\boldsymbol{\Omega}$ and $\boldsymbol{U}_p$ are expressed in Equations 4.10 and 4.11.

$$\boldsymbol{A}(t)=\begin{bmatrix}\boldsymbol{0}_{3x3} & \boldsymbol{I}_{3x3}\\ \boldsymbol{U}_p & 2\boldsymbol{\Omega}\end{bmatrix} \tag{4.9}$$

$$\boldsymbol{\Omega}=\begin{bmatrix}0 & 1 & 0\\ -1 & 0 & 0\\ 0 & 0 & 0\end{bmatrix} \tag{4.10}$$

$$\boldsymbol{U}_p=\begin{bmatrix}U_{xx} & U_{xy} & U_{xz}\\ U_{yx} & U_{yy} & U_{yz}\\ U_{zx} & U_{zy} & U_{zz}\end{bmatrix} \tag{4.11}$$

The partial derivative that make up the U_p matrix are expressed in Equation 4.12.

$$\begin{aligned}
U_{xx}&=1-\frac{1-\mu}{r_1^3}-\frac{\mu}{r_2^3}+3\left[(x+\mu)^2\frac{1-\mu}{r_1^5}+(x+\mu-1)\frac{\mu}{r_2^5}\right]\\
U_{yy}&=1-\frac{1-\mu}{r_1^3}-\frac{\mu}{r_2^3}+3y^2\left[\frac{1-\mu}{r_1^5}+\frac{\mu}{r_2^5}\right]\\
U_{zz}&=-\frac{1-\mu}{r_1^3}-\frac{\mu}{r_2^3}+3z^2\left[\frac{1-\mu}{r_1^5}+\frac{\mu}{r_2^5}\right]\\
U_{xy}&=U_{yx}=3y\left[(x+\mu)\frac{1-\mu}{r_1^5}+(x+\mu-1)\frac{\mu}{r_2^5}\right]\\
U_{xz}&=U_{zx}=3z\left[(x+\mu)\frac{1-\mu}{r_1^5}+(x+\mu-1)\frac{\mu}{r_2^5}\right]\\
U_{yz}&=U_{zy}=3yz\left[\frac{1-\mu}{r_1^5}+\frac{\mu}{r_2^5}\right]
\end{aligned} \tag{4.12}$$

The single-shooting algorithm is shown in Figure 4.2. Here the starting values are represented by $\boldsymbol{X}(t_0)$. These follow a trajectory $T(t)$ until they reach a final state $\boldsymbol{X}(t_f)$. Both initial and final state are composed by the position and velocity vector R and V in their corresponding states. Since the final state does not correspond

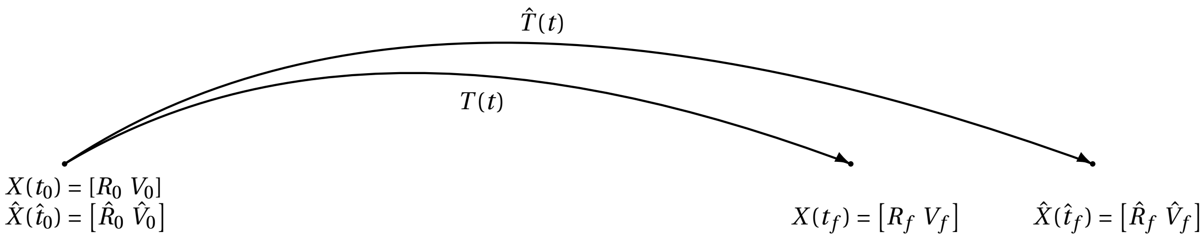

Figure 4.2: Overview of the single-shooting differential corrector.

to the final desired value there is a need for a change in the trajectory followed. In order to constrain the problem the initial and final position have been fixed. This allows for the initial and final velocity only to vary. A variation of the initial velocity from the nominal value can be interpreted as the application of a maneuver δV at the initial position R_0 in order to directly deviate the nominal $T(t)$ to a deviated trajectory $\hat{T}(t)$. The goal of the single-shooting algorithm is to reach from a starting value R_0 to a final value $\hat{R}_f$.
This numerical method can be also used to generate trajectories and halo orbits in non-linear dynamics. Figure 4.3 shows the integration steps during the generation of a halo orbit using the single-shooting algorithm in the CR3BP. Here the algorithm has been used to connect the two points that have a perpendicular x-z crossing. An example point is given by Equation 4.13.

$$\boldsymbol{X}_0 = \begin{bmatrix} x_0 & 0 & z_0 & 0 & \dot{y}_0 & 0 \end{bmatrix}^T \tag{4.13}$$

Such an approach has been described by Howell. [29] In this example four iterations allow for the residuals between nominal and final position to decrease below 10^{-14}. The used model consists of the Sun and Earths gravity model as the main bodies and the perturbing acceleration of the Moon as a third-body as well as solar radiation pressure. The algorithm stops at this instance because 10^{-13} has been chosen as a stopping condition. This condition has been chosen low enough to allow for good accuracy and precision but not too low in order to avoid reaching numerical imprecisions.

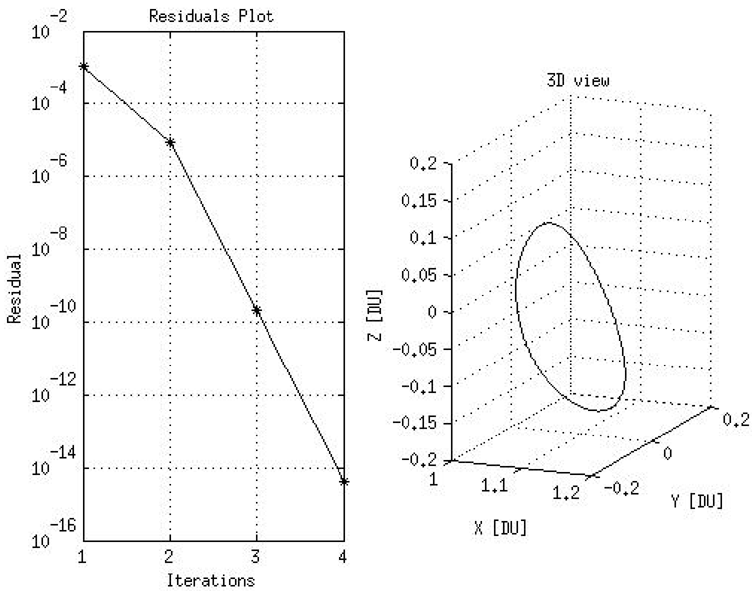

Figure 4.3: SE-L2 halo orbit created using a single-shooting algorithm in the CR3BP, including solar radiation and third-body perturbations. On the left plot the residual relations with increasing iterations is shown. The right plot shows a visualization of the halo orbit.

Equations 4.14, 4.15 and 4.16 show the relations required to derive the necessary ΔV to reach the desired position R_f. Expanding on the linearized expression in Equation 4.14, Equation 4.15 shows the relation between position, velocity and the STM.

$$\delta \boldsymbol{X} = \Phi(t_f, t_0)\Delta \boldsymbol{X} \tag{4.14}$$

$$\begin{bmatrix} \delta \boldsymbol{R}_f \\ \delta \boldsymbol{V}_f \end{bmatrix} = \begin{bmatrix} \Phi_{RR}(t_f, t_0) & \Phi_{RV}(t_f, t_0) \\ \Phi_{VR}(t_f, t_0) & \Phi_{VV}(t_f, t_0) \end{bmatrix} \begin{bmatrix} \Delta \boldsymbol{R}_0 \\ \Delta \boldsymbol{V}_0 \end{bmatrix} \tag{4.15}$$

When applying the immobility constraint to the initial position $\Delta R_0 = 0$ and with the unconstrained final velocity δV_f, Equation 4.15 can be transformed in Equation 4.16.

$$\Delta \boldsymbol{V}_0 = \left[\Phi_{RV}(t_f, t_0)\right]^{-1} \delta \boldsymbol{R}_f \tag{4.16}$$

Since linearized equations are used with the use of the STM, the used algorithm needs to be run until convergence. This convergence sets in when a preset convergence criterium is met as shown in Figure 4.3. The implementation of this numerical method has been verified as part of the course of the interplanetary mission design course at the University of Colorado Boulder. [21]

4.3. FREE DRIFT METHOD

In the context of this thesis we will use the free drift method in order to redirect the pointing vector that is constituted by the telescope and Starshade itself. For the purpose of this thesis free drift describes the free and therefore uncontrolled movement of a spacecraft. For this the Starshade and/or the telescope will drift uncontrolled as long as they meet the relative distance or angle constraints mentioned in Section 2.4.2. The starting location of this drift is noted by τ, where τ is equal to zero at the point of the Halo orbit where the value of z is highest. Such is the location “start of free drift” in Figure 4.4.

Once one or both constraints are met the free drift is interrupted and the Starshade and/or the telescope will be brought back to the nominal orbit. This trajectory back to the nominal orbit shall be named the return trajectory. Figure 4.4 shows a sketch that represents the two arcs that describe the whole drift maneuver; free drift arc and controlled trajectory back to the nominal orbit. Since this is a first-order analysis the travel time of the return trajectory has been selected to be equal to the time the spacecraft spent drifting freely.

This choice has been made due to the trade-off of having a very short return trajectory that would need a high ΔV to be performed, and a very long return trajectory which could lead for the spacecraft to wonder too far away from the nominal orbit. Essentially we would like to have the spacecraft drift away from the nominal Halo orbit, but once one of the constraints has been met it should return to the nominal orbit as soon as possible. If this return is too abrupt or takes too long to come back, the spacecraft would have to use additional ΔV in order to overcome the natural dynamics instead of using them to his advantage. For the purpose of the analysis of the dynamics in this thesis we make use of this first-order informed assumption of the return travel time to be equal to the drift time. A further analysis on this assumption can be found in Section 9.

The location of the spacecraft's return to the nominal orbit shall be the same as if this free drift maneuver had not been executed. During the free drift the natural non-linear dynamics at L2 will change the pointing direction of NWO. This free change in pointing vector is the key characteristic of the free drift method.

In the example in Figure 4.4 the Halo orbit is represented by a circular orbit. It should be noted that this is a simplification applied to ease in the graphical representation of the concept of free drift. For an accurate image of a Halo orbit please refer to Figures 3.5 or 5.1. In this image the free drift is initiated on the top of the halo orbit, at the location where τ equals zero. The spacecraft is from hereon not controlled in order to stay on the nominal halo orbit and enters an arc of free drift. This drift can be interrupted at any time by the controller at mission operations before a constraint has been met. Yet, when a constraint has been met a controlled return trajectory has to be initiated by applying two maneuver; one at the beginning and one at the end of the return trajectory, see Figure 4.4. Once the spacecraft is back on the original halo orbit it will be, as previously mentioned, located in the same location as if it would have not executed the drift method. This method can be applied either on the Starshade alone or on both the telescope and the Starshade simultaneously.

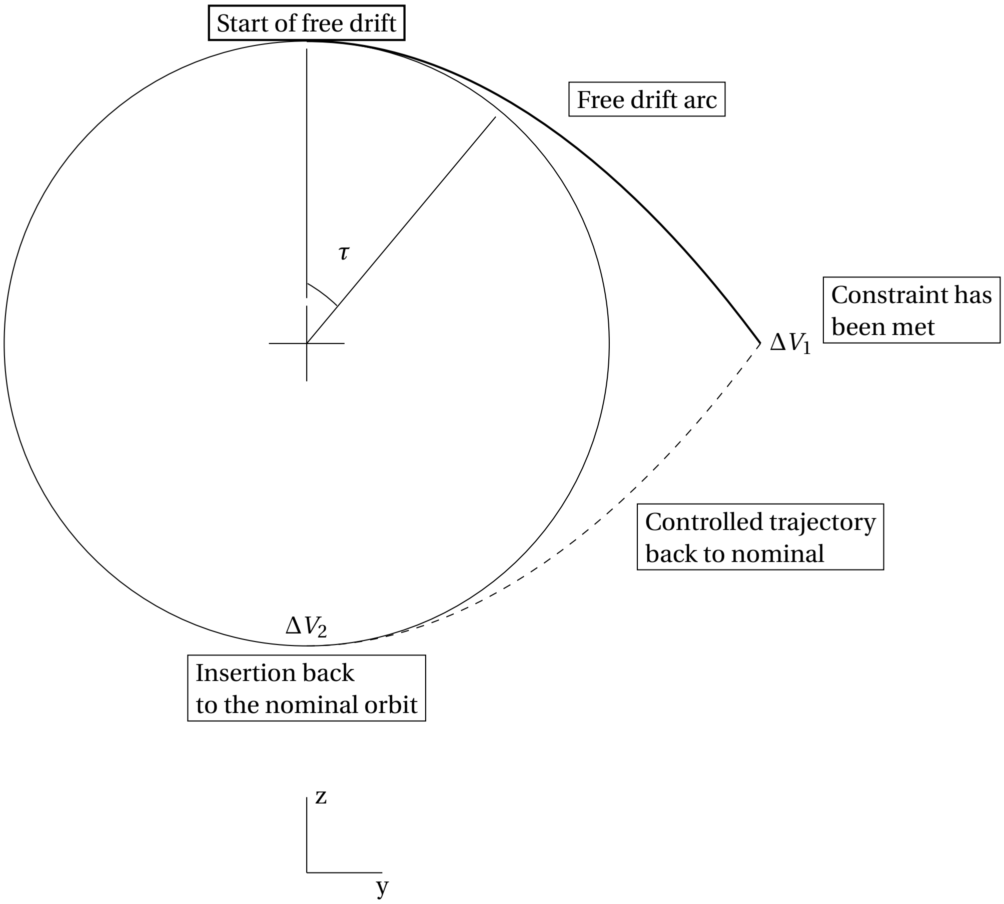

Figure 4.4: Sketch representing the free drift method. The figure is not to scale and is meant to give a visual representation of the free drift method.

4.3.1. PROPAGATION

Both the single shooting and the free drift method propagate the state of the spacecraft making use of an integrator. In order to reach the state of spacecraft at the next time epoch, the STM is used to propagate the state at the previous time step. For the purpose of this thesis we made use of a Runge-Kutta 4 (RK4) integrator. This selection was made due to its robustness and the ability to efficiently produce results with a small error. We express the RK4 by starting with Equation 4.17 and the incrementation step in Equation 4.18.

$$\boldsymbol{X}(t_0 + dt) \approx \boldsymbol{X}_0 + dt \cdot \boldsymbol{\Phi} \tag{4.17}$$

$$\boldsymbol{\Phi} = \frac{1}{6}(\boldsymbol{k}_1 + 2\boldsymbol{k}_2 + 2\boldsymbol{k}_3 + \boldsymbol{k}_4) \tag{4.18}$$

The parameters k mentioned in Equation 4.18 describe gradient information as shown in Equation 4.19.

$$\begin{aligned}
\boldsymbol{k}_1 &= f(t_0, \boldsymbol{X}_0) \\
\boldsymbol{k}_2 &= f(t_0 + \frac{dt}{2}, \boldsymbol{X}_0 + dt\frac{\boldsymbol{k}_1}{2}) \\
\boldsymbol{k}_3 &= f(t_0 + \frac{dt}{2}, \boldsymbol{X}_0 + dt\frac{\boldsymbol{k}_2}{2}) \\
\boldsymbol{k}_4 &= f(t_0 + dt, \boldsymbol{X}_0 + dt\boldsymbol{k}_3)
\end{aligned} \tag{4.19}$$

These parameters k give an average at the function derivative between the point at time t_0 and the next epoch. This is being done with the use of four gradient points. RK4 is a 4th-order-method and has therefore a local truncation error of the order of $O(h^5)$, which with a stepsize in the order of 10^{-3} results in an error of the order of 40 m. [30] Since this is a first-order analysis this magnitude in error is tolerable. Last but not least the computational time has been considered. Since convergence has been reached within a few steps and within in a reasonable time frame RK4 is an acceptable method and therefore higher order methods such as Runge-Kutta 7(8) (RK78) are not needed for this application. For a more in-depth analysis on the integration methods analysed the interested reader is referred to the literature study that has been completed prior to this thesis. [31]

4.4. NOMINAL STARSHADE SETUP

The nominal setup defines the setup that the telescope and the Starshade follow during their nominal path on the Halo orbit up to the start of the arc of free drift. This section gives an overview of the setup used in the simulations shown in Chapter 5. For the first analysis four different Starshade configurations have been chosen. These can be seen in Figure 4.5 and define the Starshade to be at four uniformly spaced positions around the telescope. The first possible location (SS-1) is above the telescope with an offset along the z-axis. The second location (SS-2) has an offset in the direction of the y-axis. All other configurations are equally spaced around the telescope as shown in Figure 4.5. Their nominal distance to the telescope is 70,000 km. The nominal Sun-L2 L2-Telescope-Starshade angle α is 90° for all Starshade configurations (i.e. SS1-4), as shown in Figure 4.6. In order to give a clearer understanding of the behaviour of the dynamics, for the remainder of this work we will make use of the angle β, which is equal to 90-α.

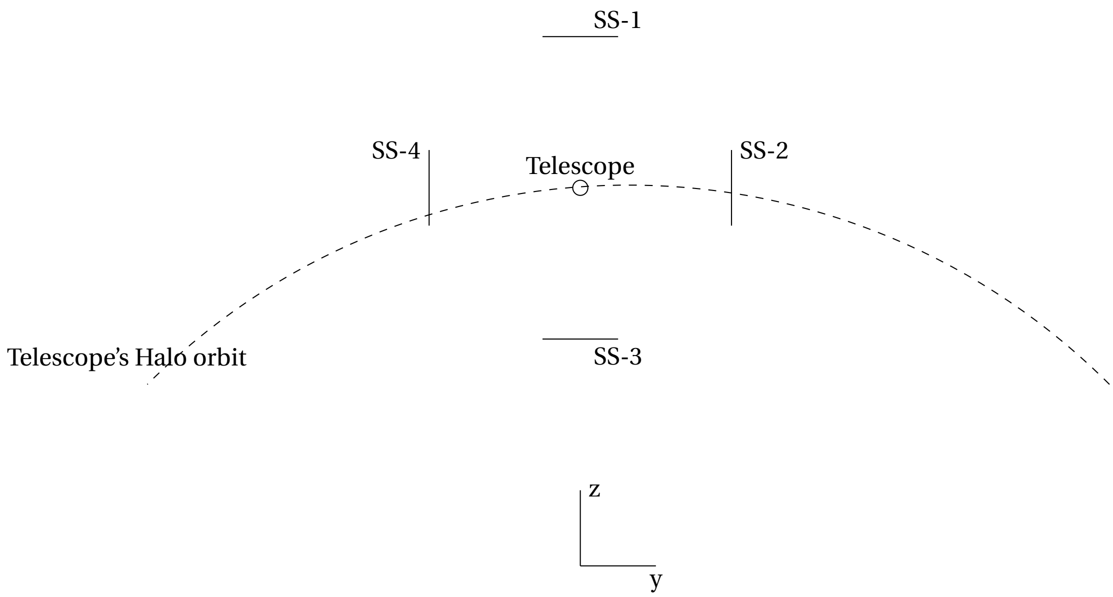

Figure 4.5: Sketch representing the Starshade configurations from the point of view of Earth (i.e. along the x-axis). This figure is not to scale.

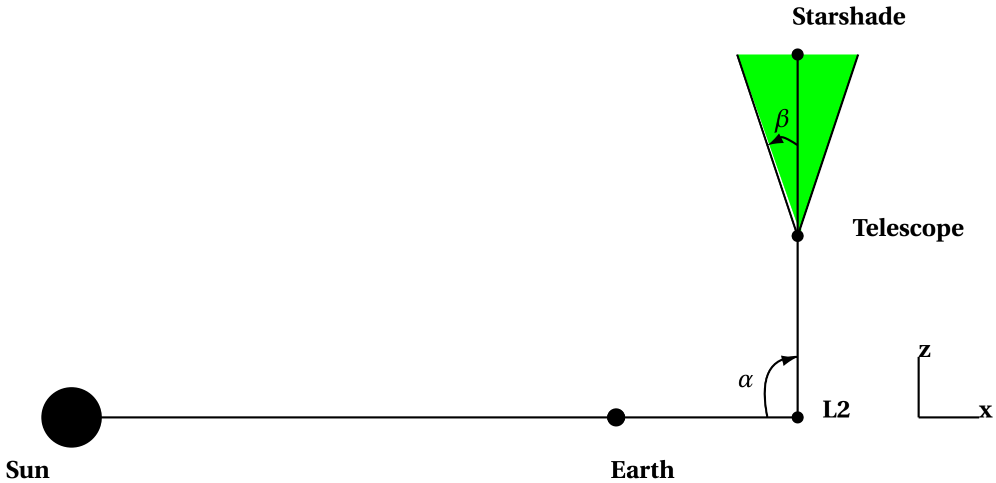

Figure 4.6: Sketch representing the angles α and β with respect to the Sun-Earth-L2 line. The green colored area shows the area where the angle constraint is met. The figure is not to scale. The location of the telescope is not necessarily exactly above the L2 point. The setup of the angles α and β is taken from [7]. This sketch is an adaptiation from [32].

5

CONSTRAINT ANALYSIS: TEST CASE

The next three chapters will give an overview of the constraint analysis that have been attained using the mission proposal described in Chapter 2, the dynamics of Chapter 3 and the methods and simulation setup described in Chapter 4. The constraint analysis describes the drift behavior for both the case of just the $\boldsymbol{S^3}$ and the case of the whole NWO (STS and $\boldsymbol{S^3}$), until one of the constraints, either relative distance or β have been met. Chapter 9 will analyze the ΔV needed for the return trajectory in order to return to the nominal orbit, as shown in Figure 4.4.

For the construction of the telescope's Halo orbit we made use of the Richardson-Cary approximation described in Section 4.1. All computations in this and all further chapters make use of a Sun-Earth L2 northern Halo orbit. An analogous computation could be done with a southern Halo orbit which would result in very similar results. For the Starshade's position we made use of the configurations described in Figure 4.5. For these we used the nominal position offset of 70000 km described in Section 2.4.2 and computed the velocity in such a way so that the Starshade would follow the telescope, with the same velocity of the STS, without having to deviate from its configuration. This positions the $\boldsymbol{S^3}$ on an artificial quasi-Halo orbit. An overview of telescope's Halo orbit and of the orbit of the four Starshade configurations can be seen in Figure 5.1. Here different colors have been chosen to give a clearer understanding of which configuration is being analyzed at any given moment. This choice of color and nomenclature for the various Starshade configurations will be used consistently throughout the entirety of this document. The SS-1 configuration defines the $\boldsymbol{S^3}$ to have the same cartesian position as the STS in x and y, but varies in z by the nominal distance of 70000 km. For the SS-2 configuration the position of the $\boldsymbol{S^3}$ varies from the STS in y by 70000 but is equal in both x and z. In the case of SS-3 the variation in position between $\boldsymbol{S^3}$ and STS is in negative z direction by 70000 km and equals in both x and y. Lastly, SS-4 is defined to be equal in x and z but varies between $\boldsymbol{S^3}$ and STS in negative y direction by 70000 km. This same color scheme and configuration is used throughout this thesis.

In this section we shall give an overview of the behavior that we expect the different Starshade configurations to have by analyzing the dynamics surrounding the nominal orbit which is defined by the telescope's Halo orbit.

Chapters 6 and 7 shall then analyze the numerical outcomes for the nominal case and compare them with the general behavior that we describe in this section. Chapter 6 describes the constraint analysis for the case where only $\boldsymbol{S^3}$ drifts, whereas Chapter 7 shows the constraint analysis if both spacecraft of NWO drift simultaneously. Chapter 8 finally gives some insight on the expected effects that a constraint variation in relative distance or angle has on the drifting time before a constraint has been met and the associated pointing vector variation.

5.1. SETUP AND ANALYSIS

In order to analyze the conditions near the nominal telescope halo orbit we have devised a test case. The configuration selected for this test case has been chosen in such a way that the Starshade configurations are close enough to the nominal Halo orbit to be in the linear regime of the Libration point. This selection is

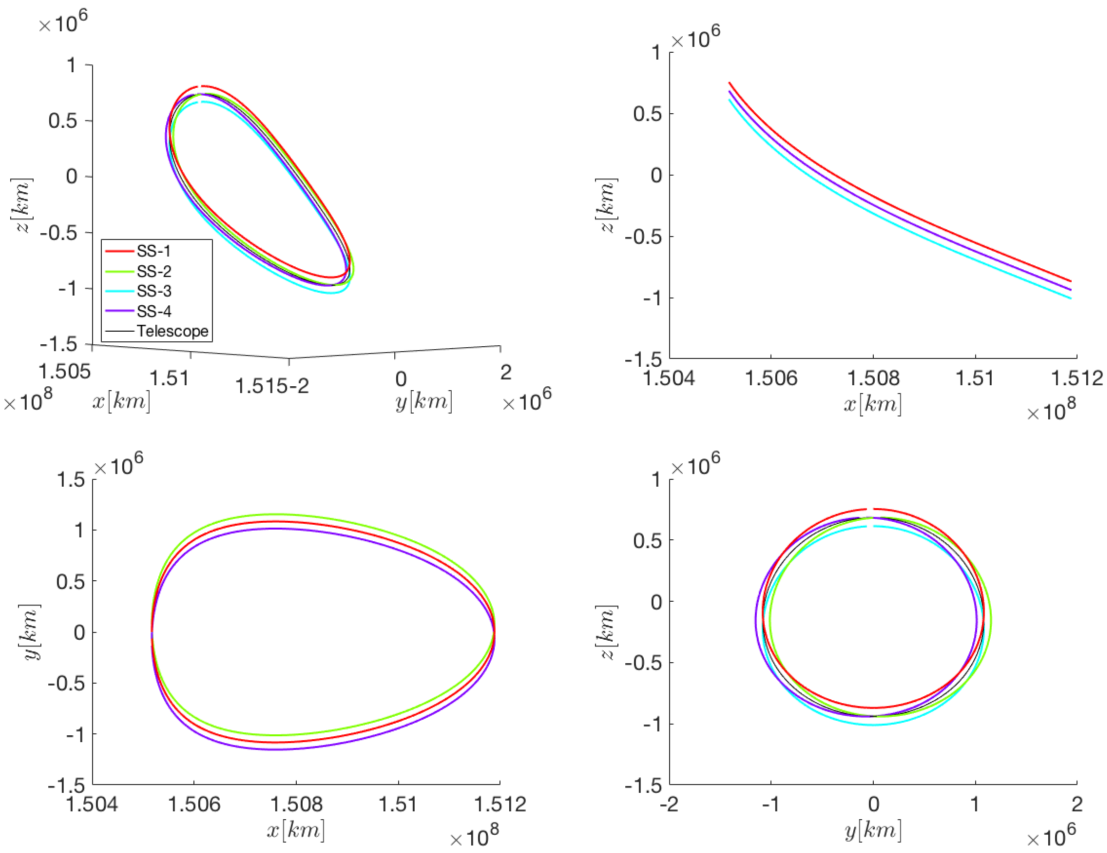

Figure 5.1: Family of northern $SE-L_2$ Halo orbits studied here. Both telescope and various Starshade location geometrics are shown in this figure.

important since this linear regime is predictable and allows us to indirectly verify the validity of the generated solutions and therefore of our code. The selected test case is described by the following items:

- Initial relative distance = 50 km
- Initial $\beta = 0°$
- Relative distance variation allowed: ≤ 200 % of the initial distance
- Angle variation allowed: $-2° \leq \beta \leq 2°$
- Starshade is allowed to drift
- Telescope does not deviate from the nominal halo orbit
- Four equally spaced Starshade configurations

As can be seen from this test case configuration the Starshade is chosen to be much closer to the nominal Halo orbit of the telescope. This distance is selected to show the different behavior of the various orbits of the Starshade configurations compared to the telescope's nominal orbit. The constraint for the relative distance has been selected in order to allow for some time of drift. If this constraint would have been chosen to be too strict the drift in the linear regime would not be observable at all. The initial β angle of 0° is the same as for our real case. The angle variation allowed has been constrained to just two degrees. The reasoning for this choice is analogous to the selection process for the relative distance allowable variation.
The first analysis using this test setup shall be the comparison of the potential described by Equation 3.4 for the case of STS and $\boldsymbol{S^3}$. This can be seen in Figure 5.2. As can be seen the potentials experienced by both STS

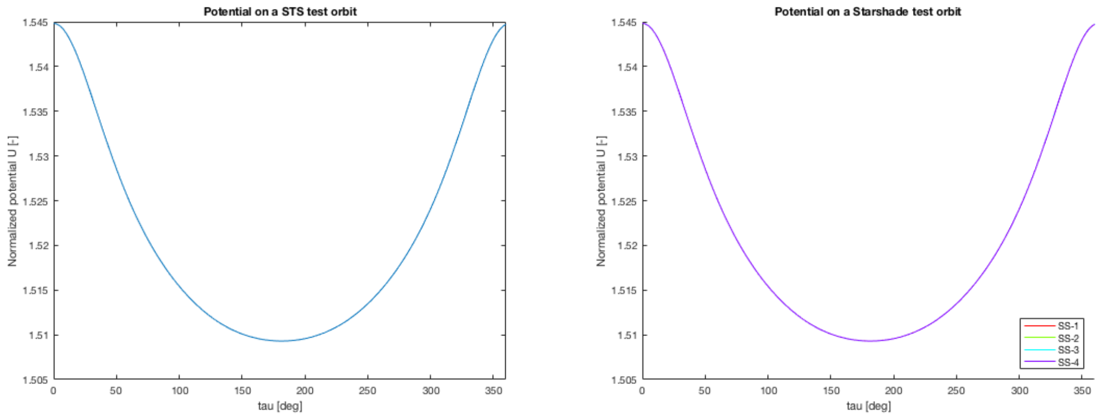

Figure 5.2: Comparison of the normalized potential experienced by the STS on the nominal orbit and the STS configurations along their test orbit.

and S^3 are nearly identical. The differences are too small to be visible in these plots, but will be more clearly visible once a full constraint analysis has been completed as can be seen in the later part of this section.

Figure 5.2 seem to show a nearly identical behavior for the normalized potential of the test orbits for the various Starshade configurations, yet they are not exactly the same. To show these diversity we will plot the differences of these potentials. The resulting difference in the potential between the different Starshade configurations in their nominal test orbit can be seen in Figure 5.3. Here we see that in the worst case scenario the difference in normalized potential does not exceed 0.05 % of the nominal value, shown in Figure 5.2 which is very good since it shows a very small deviation from the nominal normalized potential.

As a next step in our test case analysis we are interested to see if the selected test case is indeed close enough to the linear regime that the various S^3 configurations experience nearly identical magnitudes of potential, acceleration and velocity as they drift away from their nominal orbit. For this purpose we generated Figures 5.4, 5.5 and 5.6. Note that the values along the x-axis of Figure 5.4 equal to the value given in right plot in Figure 5.2. All these plots are as expected indistinguishable among each other which they are, indicating that the setup of the test condition is within the linear regime. If the conditions would have not been in the linear regime then the differences in the plots of Figure 5.4 would over time follow non-linear behaviors.

In the last step before continuing to the constraint analysis it is useful to know what is the difference between the acceleration needed to stay on target and the acceleration that the Starshade experiences due to third body perturbations. The acceleration due to the Moon, as the only third body present, has been selected here since it is the dominant perturbation force as shown in Section 3.5.1. The difference in acceleration due to the Moon and the acceleration needed to stay in a specific configuration (SS-1 to SS-4), as given in Section 4.4, is plotted in Figure 5.7. From this difference we should be able to infer information on the general behavior that is to be expected during the constraint analysis. This difference in accelerations shows that there is a symmetry to be expected around the middle of the Halo orbit.

Having verified that the deviations in the test case selected are small we can move on to the constraint analysis, which is explained in the next section.

5.2. CONSTRAINT ANALYSIS

Using the test setup explained in detail in the previous section we shall analyze the behavior of S^3 in the case it starts a free drift maneuver as described in Section 4.3. To do this we shall analyze the angle and relative distance constraints separately. For this and all subsequent constraint analyses it is assumed that once a constraint has been met the simulation will be stopped. This should be mentioned because there are cases where the spacecraft exceeds the constraint and after a period of time reenters the constraints. These cases are deemed to be out of the scope of this thesis and shall not be considered here.

Since this is a first-order test analysis the time interval analyzed has a daily temporal resolution. This means that if for example a constraint has been met within the first day, the plot will show one day as a maximum interval that can be reached. This has been chosen in order to minimize the computations; when computing the nominal case become quite cumbersome.

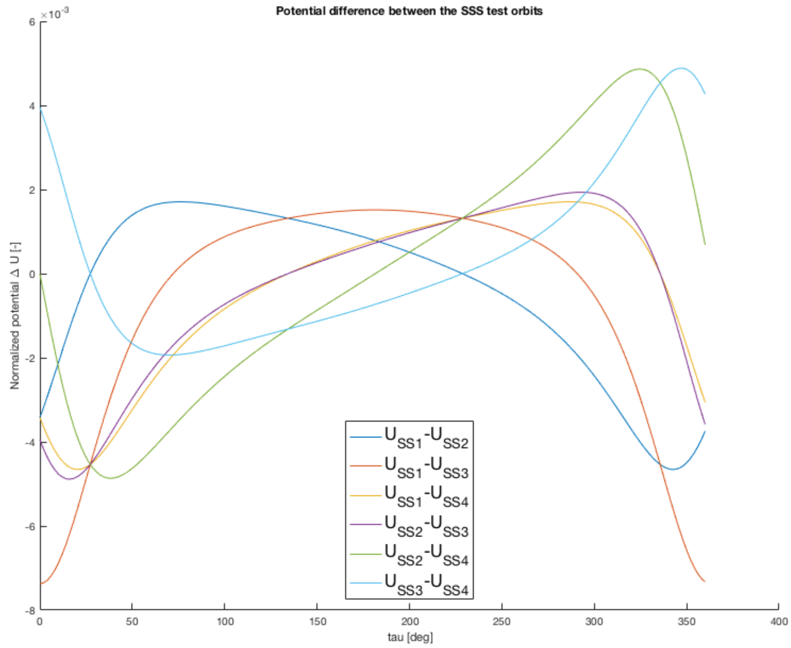

Figure 5.3: Difference in the potential between the different Starshade configurations.

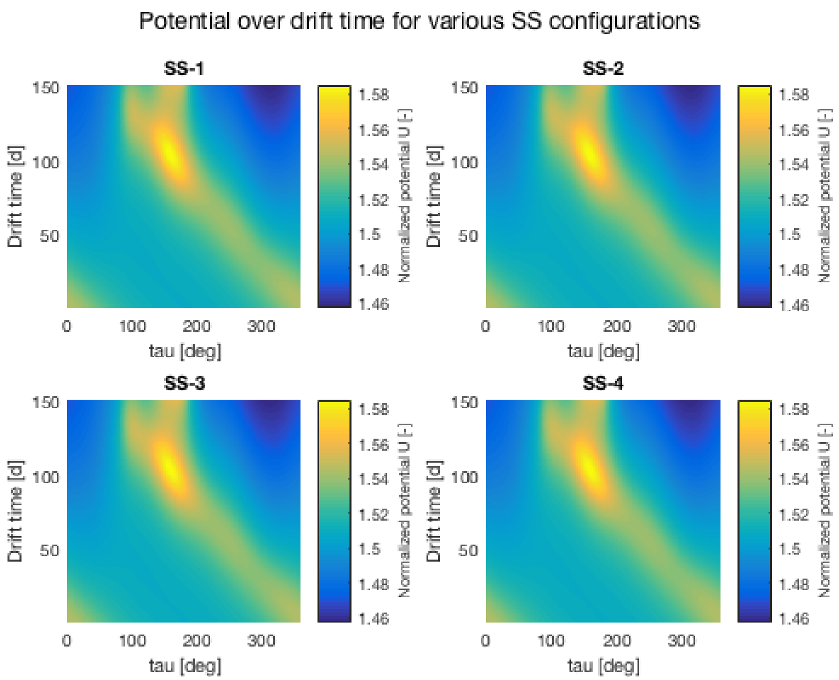

Figure 5.4: Normalized potential experienced over time of drift in relation to the initial drift location of τ for the test case using four different S^3 configurations.

That being said, let us analyze the relative distance constraint for the case that only the Starshade is drifting freely and the telescope remains on its nominal Halo orbit. The result can be seen in Figure 5.8. Here we can see the expected symmetry, that was foreshadowed in the previous section by Figure 5.7. The configurations SS-1 and SS-3 show a symmetric behavior along the x-axis of the Halo which runs at a value τ of 180°, with

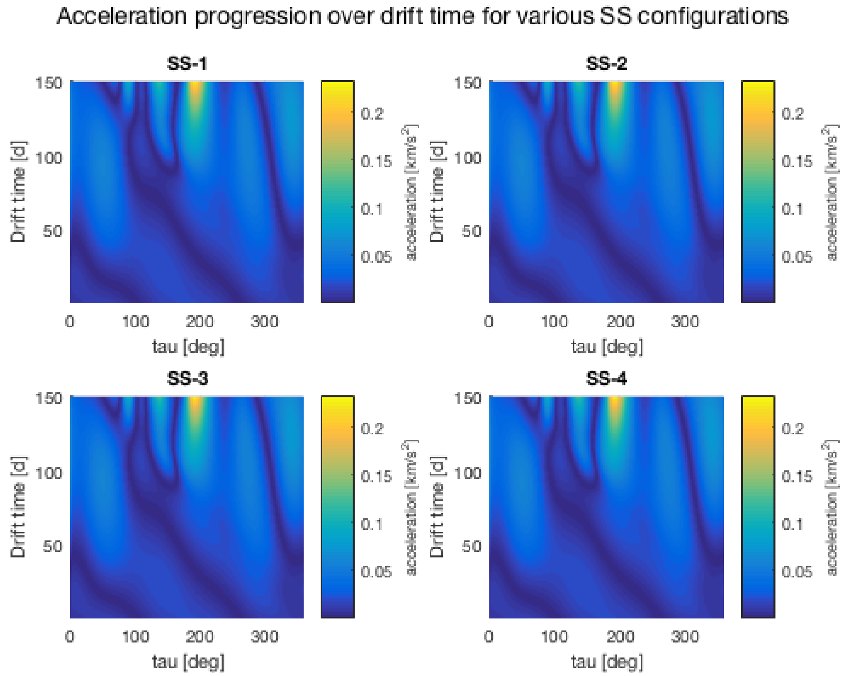

Figure 5.5: Acceleration experienced over time of drift in relation to the initial drift location of τ for the test case using four different S^3 configurations.

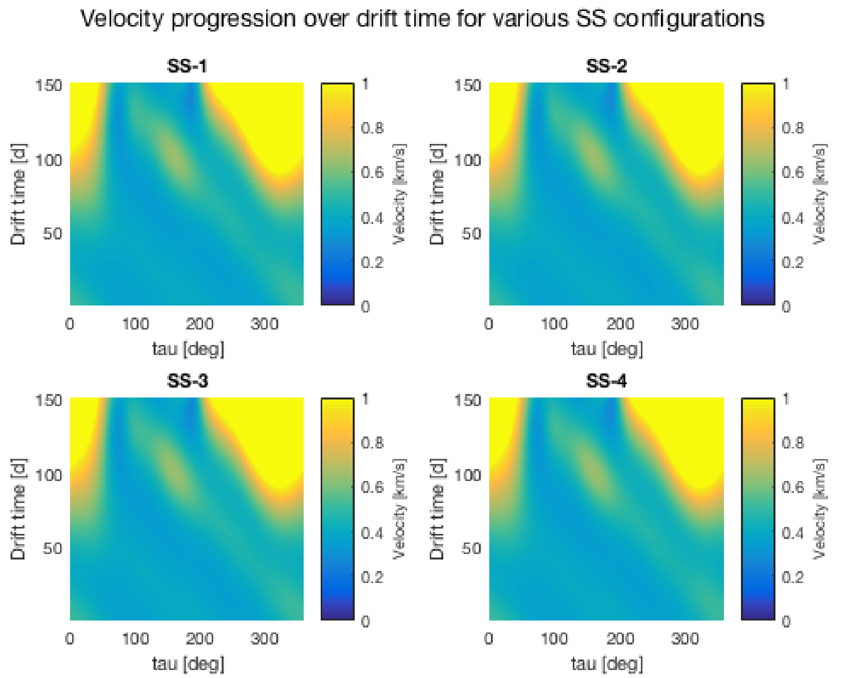

Figure 5.6: Velocity experienced over time of drift in relation to the initial drift location of τ for the test case using four different S^3 configurations.

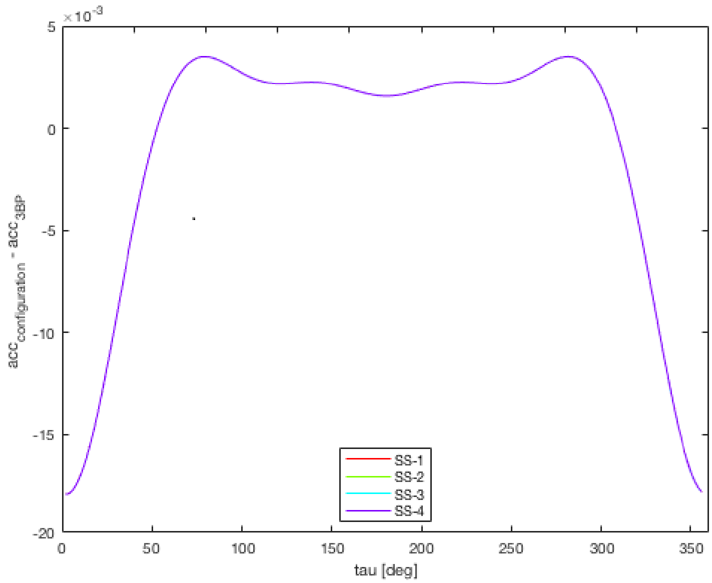

Figure 5.7: Difference between the acceleration needed to stay on target for each configuration and the third-body perturbations experienced due to the Moon. The value for τ has been normalized and represents one halo orbit.

a variation in the days that can be reached as a maximum value. This is to be expected because both configurations are in the linear regime with a slight variation in their position in the z-direction. This affects the number of days that can be drifted before the relative distance constraint has been met.
Configurations SS-2 and SS-4 show a quasi-symmetric behavior around the value τ of 180°. This can be explained due to the relative geometries of SS-2 and SS-4 in relation to the telescope. For the case of τ between 0° and 180° SS-2 has an offset that sets its position to the outside of the nominal telescope orbit. For 180° and 360° the configuration SS-2 lies relative to the telescope within the orbit of the halo orbit. This explains why the behavior for the values left and right of tau 180° is symmetric but varies in the maximum value. These same dynamics can be seen for SS-4. If we take the values of τ between 0° to 180° for SS-2 and 180° to 360° for SS-4, then we have a setup that is always shifted towards the outside of the halo orbit, except for the points of symmetry at 180° and 360°. This creates a symmetric behavior. This same symmetry can be observed when taking the values of τ between 0° to 180° for SS-4 and 180° to 360° for SS-2. Through this analysis we get an interesting insight on the behavior that the Starshade configurations have regarding their offset in relation to the telescopes nominal orbit.
Next, let us analyze the β constraint applied to the test case as shown in Figure 5.9. Here we can see a very clear symmetry for all cases along the value τ of 180°. The behavior of antisymmetry as in Figure 5.8 cannot be observed due to the absence of values for τ higher and lower than the symmetry along the x-axis. An analysis for higher values of β when using the test case constraints has been performed, but resulted only in a variation of height of the spike observed in Figure 5.9. This is to be expected when maintaining the relative distance constraint constant, because the only driving constraint is in this case the angle, where bigger angle boundaries lead directly to a higher number of allowable days of drift.
Figures 5.8 and 5.9 show the expected behavior and we can therefore say that the test case analysis was performed successfully. A further analysis on how the relative distance and the angle constraint influence each other would be an interesting additional analysis, but was deemed to be out of scope for the purpose of this body of work.

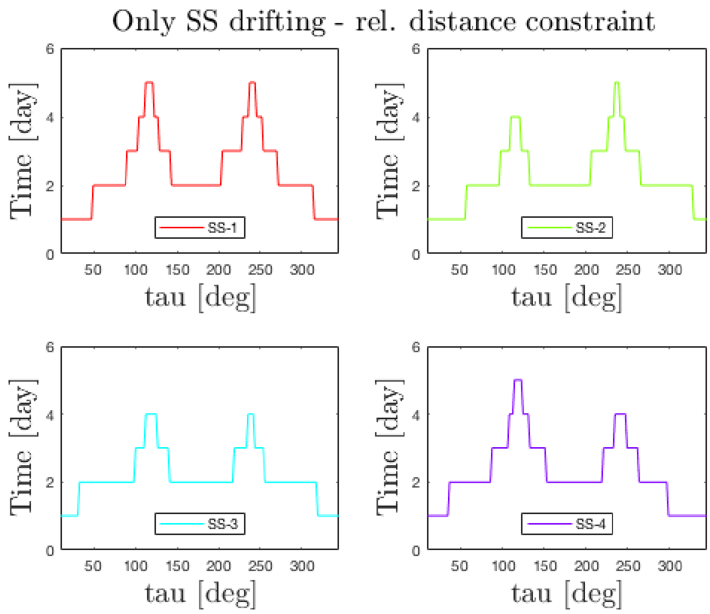

Figure 5.8: Relative distance constraint analysis for the test case using four different Starshade configurations.

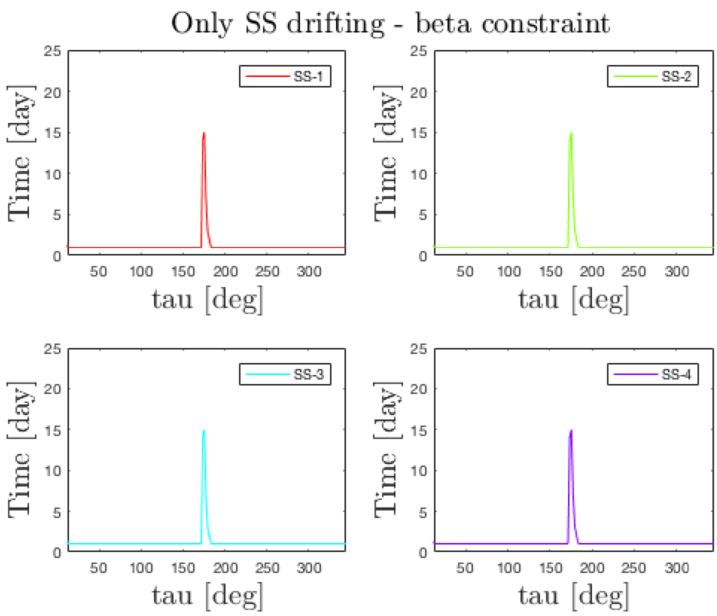

Figure 5.9: β angle constraint analysis for the test case using four different Starshade configurations.

6

NOMINAL CASE: STARSHADE UNLIMITED DRIFT

For this section we will make use of the nominal configuration as described in Section 4.4. For the ease of the reader we shall briefly mention them again here and they are as follows:

- Initial relative distance = 70000 km
- Initial $\beta = 0°$
- Relative distance variation allowed: ≤ 20 % of the initial distance
- Angle variation allowed: $-15° \leq \beta \leq 45°$
- Starshade is allowed to drift
- Telescope does not deviate from the nominal halo orbit
- Four equally spaced Starshade configurations

Analogous to the test case analysis we will first observe the effect that the dynamics has on the potential, acceleration and velocity before we move to the actual constraint analysis. Figure 6.1 shows the potential for the four used S^3 configurations. The offset between the nominal telescope potential and the various Starshade configurations is much greater than for the analyzed test case. This was to be expected since the nominal relative distance between STS and S^3 is much greater. The observed offset is analogous to the variations determined for the test case in Figure 5.8. There is a symmetric component for SS-1 and SS-3 whereas SS-2 and SS-4 are shifted to the left and right of the value of τ 180°, as seen in Figure 6.1. This increase in potential energy deviation is surely expected to have a considerable effect on the relative distance constraint. Due to the symmetry we do not notice an increased effect on the β angle.
As a next step we shall analyze the variation of the potential, acceleration and velocity as a progression of drift time and drift starting location on the halo orbit, defined by τ . For this we generated Figures 6.2, 6.3 and 6.4. As for the test case also in this case where only the S^3 drifts the values along the x-axis of Figure 6.2 equal to the value given in right plot in Figure 6.1. Except for the velocity in Figure 6.4, these plots show little to no similarities. For the velocity there is also only similarities at drift times below 50 days, values beyond are very different between the four S^3 configurations. This leads to believe that the linear behavior around a Halo orbit might be smaller than the nominal distance between telescope and Starshade of 70000 km. At what distances from the halo orbit the non-linearity becomes prevalent deserves a deeper analysis that unfortunately is out of scope for this first-order analysis, but should definitely be investigated when considering further analysis in a formation flying mission at a Lagrangian point.
When computing the difference between the acceleration needed to stay on target and the main perturbing force, the third-body perturbation, we can generate Figure 6.5. Here we see a shift in the acceleration difference that is directly related to the shift in the potentials shown in Figure 6.1. The configurations SS-1 and SS-3 vary in their magnitude, but are both symmetric around the τ value of 180°. For the case of SS-2 and SS-4 there is only a symmetry around a τ value of 180°. The same relative dynamics applies here as has

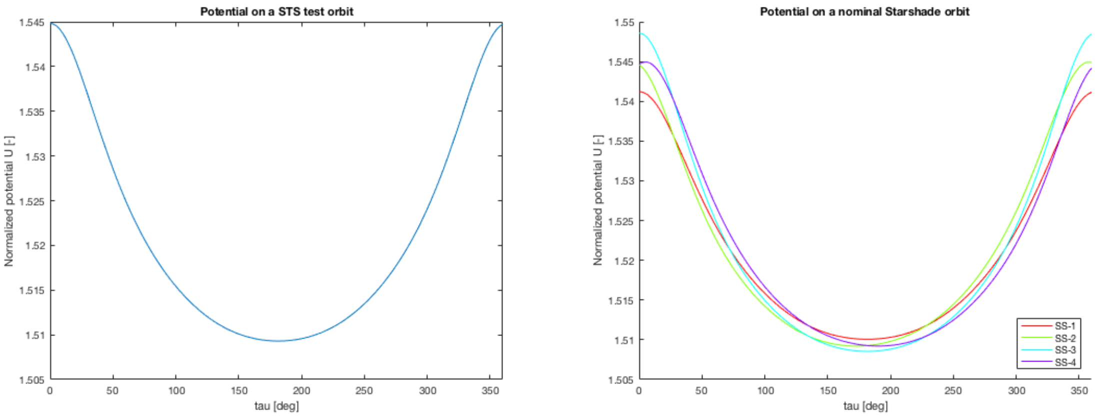

Figure 6.1: Comparison of the normalized potential experienced by the STS on the nominal orbit and the STS configurations along their nominal case orbit.

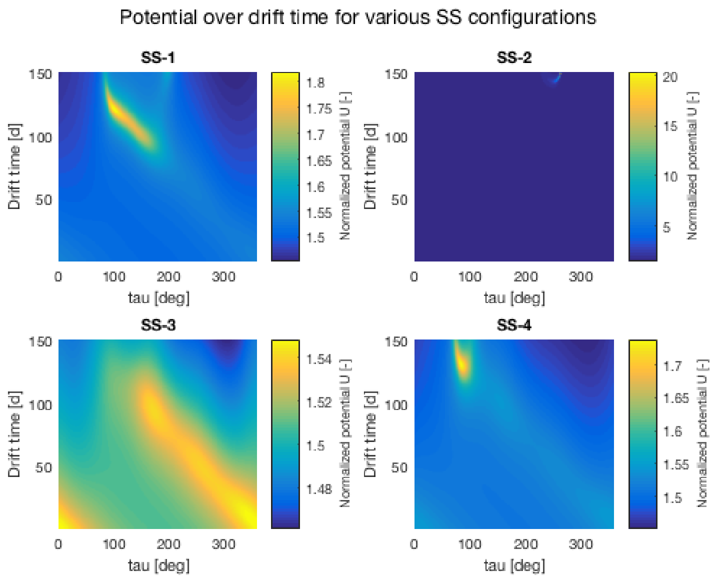

Figure 6.2: Normalized potential experienced over time of drift in relation to the initial drift location of τ for the nominal case using four different S^3 configurations.

been explained for the case of SS-2 and SS-4 in Figure 5.8. A similar behavior can be seen in the difference in acceleration due to the Moon and the acceleration needed to stay in a specific configuration (SS-1 to SS-4), as given in Section 4.4, is plotted in Figure 6.5. From this difference we can infer information on the general behavior that is to be expected during the constraint analysis. This difference in accelerations shows that there is a symmetry to be expected around the middle of the Halo orbit for the SS-1 and SS-3 configuration. In contrast to those two configurations, SS-2 and SS-4 have an antisymmetric behavior around τ 180°.

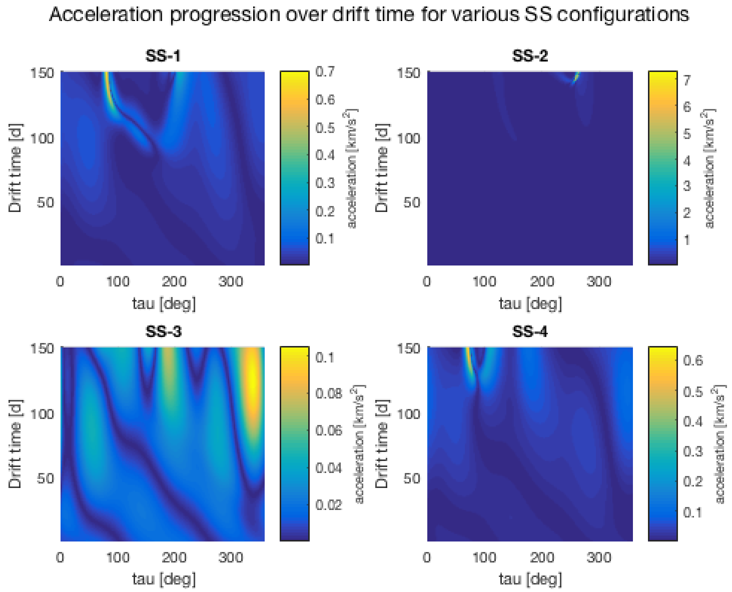

Figure 6.3: Acceleration experienced over time of drift in relation to the initial drift location of τ for the nominal case using four different S^3 configurations.

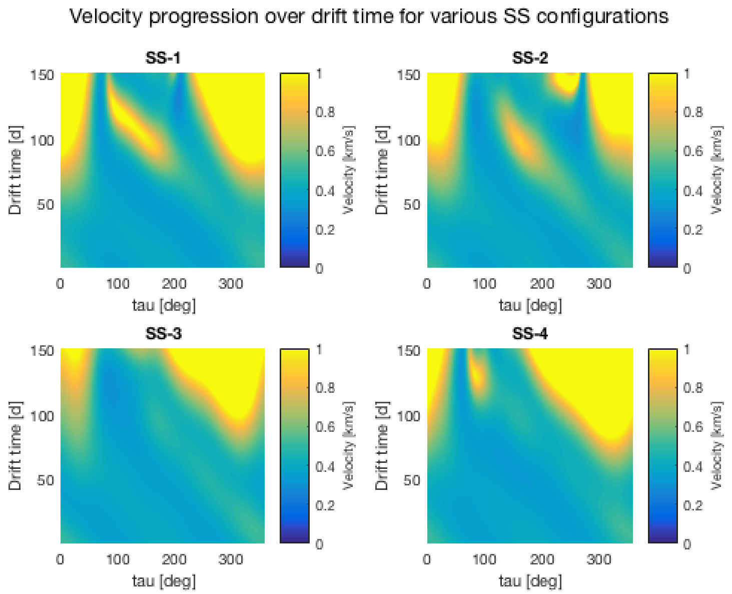

Figure 6.4: Velocity experienced over time of drift in relation to the initial drift location of τ for the nominal case using four different S^3 configurations.

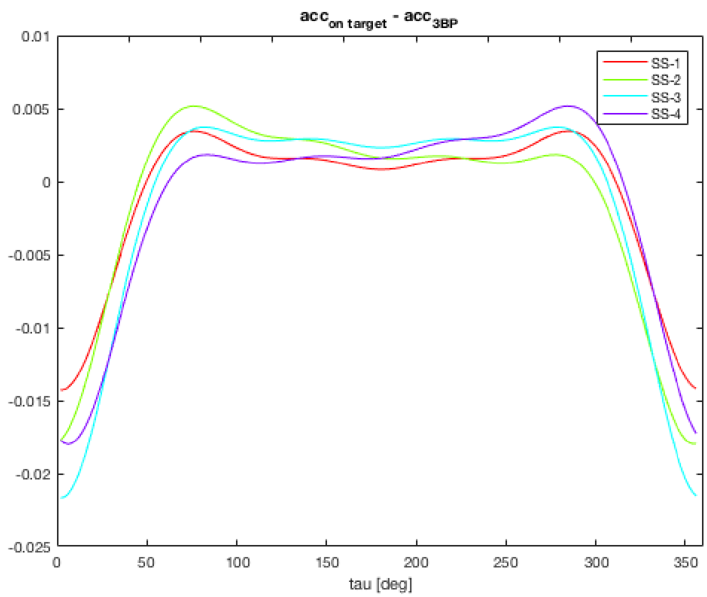

Figure 6.5: Difference between the acceleration needed to stay on target and the third-body perturbation due to the Moon.

6.1. NOMINAL CASE: STARSHADE DRIFT CONSTRAINT

As for the test case we will analyze the constraints for the nominal case separately. In addition we will also merge both the relative distance and the angle constraint relations in order to show an overall constraint behavior. This will be later used in Chapter 9 for the Δ V analysis of the return trajectory for the nominal case. The first constraint that we will analyze for the nominal case is the relative distance. The simulation has been done just like in the test case but with the adaptations to the setup mentioned at the beginning of Chapter 6. From this procedure we generate Figure 6.6. Here we can notice that there is a slight symmetry for SS-1 and SS-3 around τ equal to 180°. The resulting symmetry is distorted probably due to the Starshade reaching into the non-linear regime. The configurations SS-2 and SS-4 do not show such a strong symmetry as in the test case in Figure 5.8. Some hints on symmetry can be found when observing the SS-2 and SS-4 configurations. An example for this is the spike at SS-4 on τ 20° and at SS-2 at τ 330°. Another illustration of this phenomenon is the dip that can be found observing SS-2 at τ equal 50° and at τ equal 310° at SS-4. Yet these plots are not conclusive enough to prove a symmetry. This high distortion of the symmetry could follow from the fact that these configurations are reaching or have already reached the non-linear regime. This would set the boundary between the linear and the non-linear regime at around 20 days of free drift.

As mentioned in Section 6 this distortion could also follow from the increased relative distance between the telescope and Starshade, which could be either already out of the linear regime around the halo orbit or alternatively, that the constraint bounds allow the Starshade to leave the linear regime later on. The range variations that are allowed are between of 20% of the nominal value of 70000 km. This is equal to a minimum and maximum distance to the location of the telescope on the nominal Halo orbit of 56000 km and 84000 km respectively.

For the β angle constraint analysis the nominal constraints are set at $-15°$ and 45° . This leads to an even greater allowable drift time, before one of the two angle bounds are reached, as shown in Figure 6.7. The drift time in these simulations reaches over 100 days. Overall the relative distance is the dominant constraint. The high drift times leads to a regime that is obviously non-linear anymore. Yet there are also small values of drift time that show a similarity between the four Starshade configurations. This is true for very low values and very high values of τ. This corresponds to the section of the Halo orbit with the highest values for initial position in the z-axis. Since this area is the one with lowest values of drift time for the β constraint is equivalent to that the same area on the Halo is also the most unstable in relation to angle constraints.

An example to further clarify this situation can be seen in Figure 6.8. Here the location at the start of the drift maneuver on the Halo (τ) is shown in relation to the three-dimensional behavior that the relative Starshade configuration experiences. When we analyze the given figures it is most useful to observe the projection on the xz-plane; the third column. Here we can see that the drifting trajectories match the nominal case quite

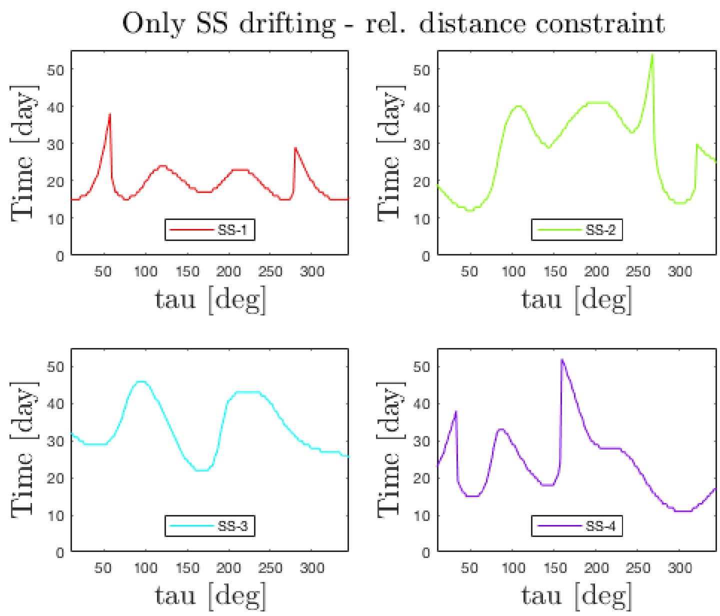

Figure 6.6: Relative distance constraint analysis for the nominal case using four different Starshade configurations.

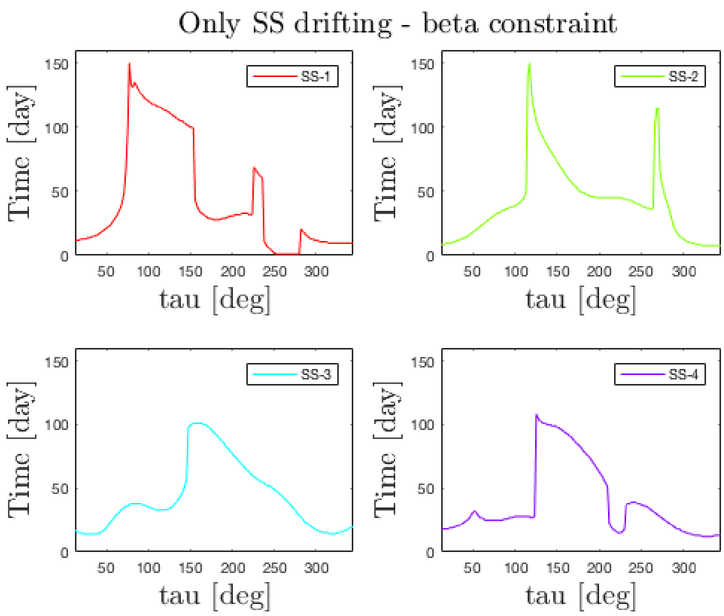

Figure 6.7: β angle constraint analysis for the nominal case using four different Starshade configurations.

well, except for the case where τ is $0°$. Here the deviation is relatively rapid for all Starshade configurations. This stands directly in relation to the angle constraint behavior previously analyzed in Figure 6.7. When superpositioning Figures 6.6 and 6.7 we get Figure 6.9. It is not surprising that these resulting plots are for the most part similar to the results obtained with the relative distance constraint only. This is because for most initial locations on the Halo orbit (τ) the relative distance is the limiting factor. This constraint is mostly affected by the dynamics in the y-direction, the angle β on the other hand can be affected by the dynamics in all directions depending on where the drift is initiated on the halo orbit. The symmetry in Figure 6.9 is lost as in the previous case due to the non-linear regime.
Now that both the relative distance and the angle β have been analyzed, we can see how this affects the pointing vector of the NWO system for this case where only the Starshade drifts. For this analysis we make use of Figure 6.10. Here we can see that the portion of the sky that is being covered is quite limited, when using

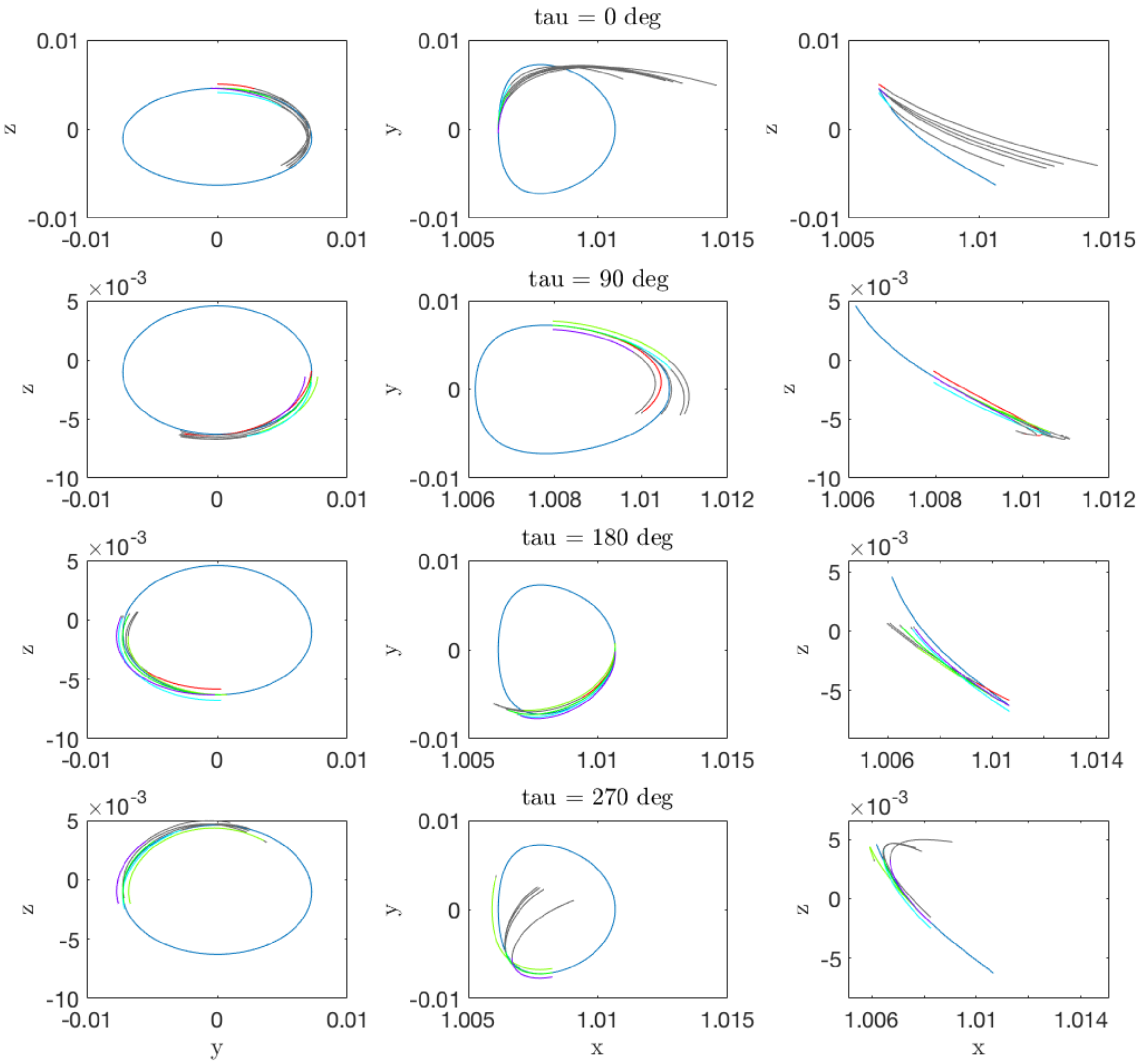

Figure 6.8: Three-dimensional visualization of the relation between location where drift starts (τ) and the angle variation. The blue halo orbit represents the nominal Halo orbit. The colors used to represent the various Starshade configurations are consistent with the previous definitions. The black line represents positions where the Starshade configuration is outside the bounds of the angle constraints. The label has been omitted to aid in the visualization.

this setup and constraints. We should reiterate that SS-1 and SS-3 point both to the northern and southern celestial hemisphere, where SS-2 and SS-3 point in the horizontal plane, as shown in Figure 4.5. This explains their respective pointing vector behavior.

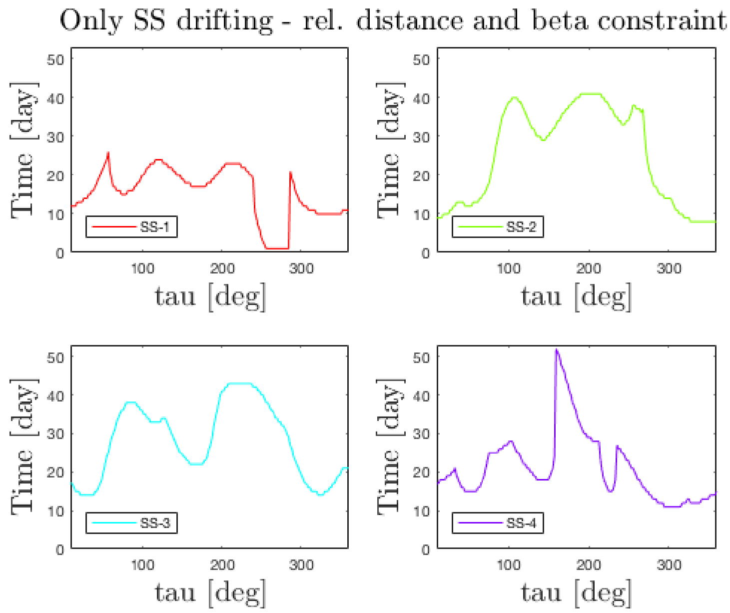

Figure 6.9

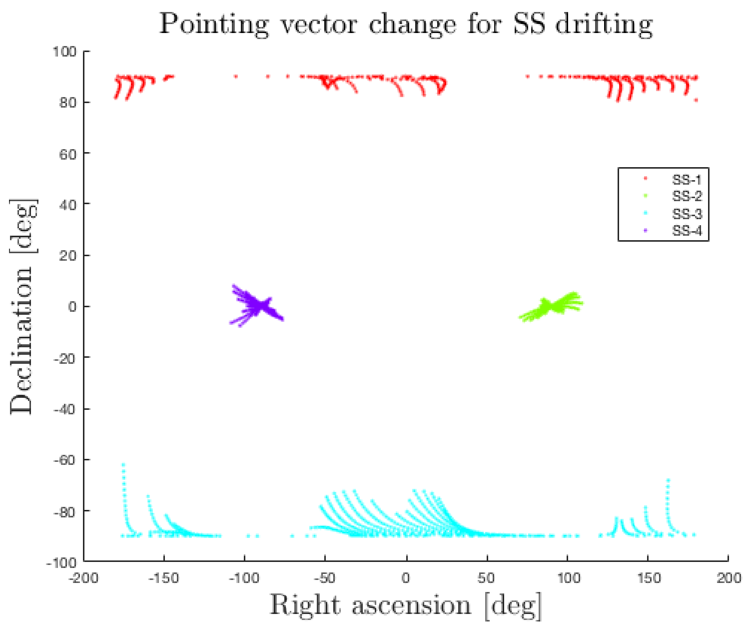

Figure 6.10: Pointing vector projection on the sky map using the nominal conditions, both the relative distance and the β constraint for the four different Starshade configurations.

7

Alternate case : STS and S^3 unlimited drift

As an alternative scenario we will analyze a simulation setup where both the Starshade and telescope drift simultaneously. In the previous example the STS's orbit was defined by the Halo and the S^3 was propagated numerically to simulate drift. In this case both NWO spacecraft drift simultaneously, which is simulated by a simultaneous numerical propagation. For this analysis we will skip the potential analysis for the Starshade since it has been covered thoroughly in Section 6 and remains mostly unchanged for this new case variation. The major change comes from the addition of the telescope as a drifting body, but since we are going to analyze the constraint behavior to a drifting telescope the potential plots will not be as useful to be extracting information from. Therefore we shall immerse ourselves straight in the constraint analysis. Figure 7.1 shows the relative distance constraint for the the new case variation.

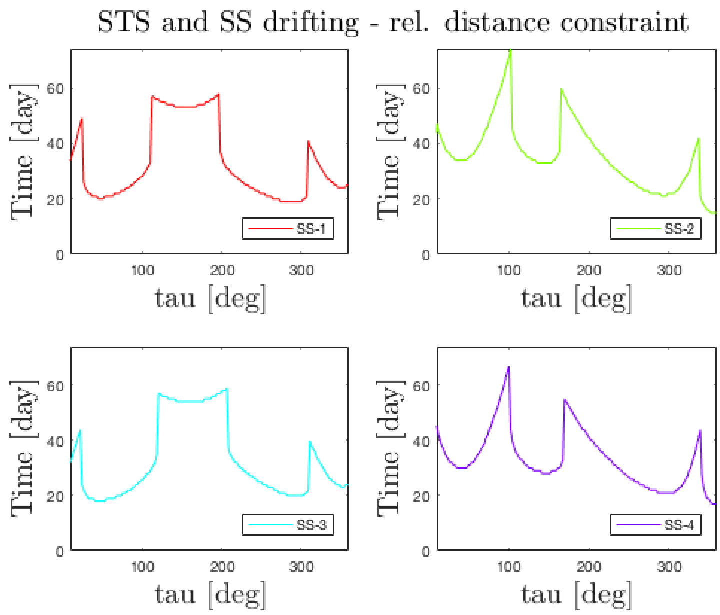

Figure 7.1: Relative distance constraint analysis for the alternate case, where both NWO spacecraft drift simultaneously.

In this case both spacecraft are released from their controlled orbit and drift at the same time and enter a free drift maneuver at the same time. The drift times that are allowable before hitting one of the two constraints are for this alternative case, where both NWO spacecraft drift, generally longer than when only S^3 drifts (see Chapter 6). This is because when both spacecraft drift they drift together in roughly the same direction in contrast to having one spacecraft orbit on a nominal Halo orbit and the other being drifting. This simultaneous drift allows them to reach the constraint at a much later epoch than in Chapter 6. The configurations SS-2

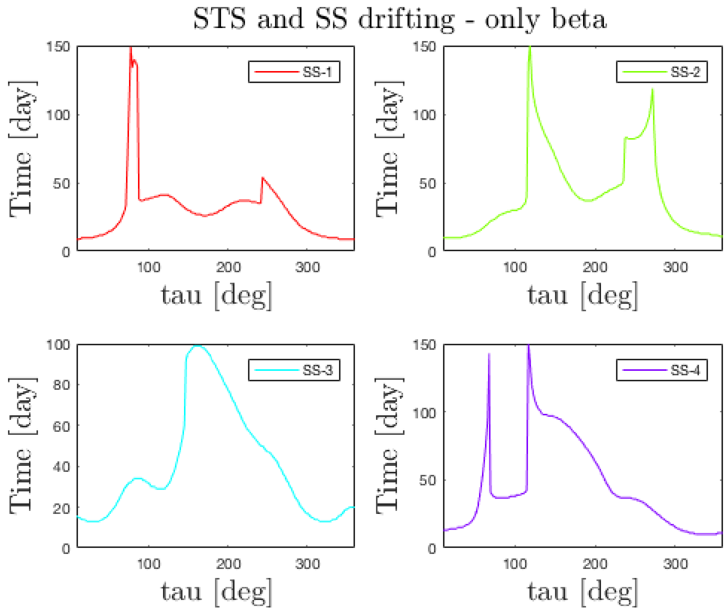

Figure 7.2: Angle constraint analysis for the alternate case, where both NWO spacecraft drift simultaneously.

and SS-4 show a very similar, but not identical, behavior. Since they both share the same offset configuration in the xy-plane a very similar behavior is to be expected. The same can be said for SS-1 and SS-3.
For the angle β variation in Figure 7.2 we can see low values for a value of τ close to 0°. When plotting the three-dimensional plots as has been done previously in Figure 6.8 but this time for this alternate case we get the plot shown in Figure 7.3. It is curious to notice that the angle constraint behavior for SS-2 and SS-3 in the alternate case remains very similar to those configurations in the nominal case. The biggest changes are for the configurations SS-1 and SS-4. This leads to believe that when the telescope is using a drift maneuver, which the case here, it does not vary too much from its nominal orbit. Therefore the results for the angle constraint are quite similar to those of the nominal case.
When both constraints are superpositioned we obtain Figure 7.4. When we compare this to Figure 6.10 we see that the average number of days of drift within the constraints are on average higher than in the nominal case where only S^3 was drifting, as was observed already when comparing Figures 6.6 and 7.1. This increase in allowable drift time reflects directly on the pointing vector in Figure 7.5 when analyzed in comparison to Figure 6.10. Such an increase in the change in pointing vector means that drift can be used to reach stars that are further away from each other on the sky map. This is very promising.

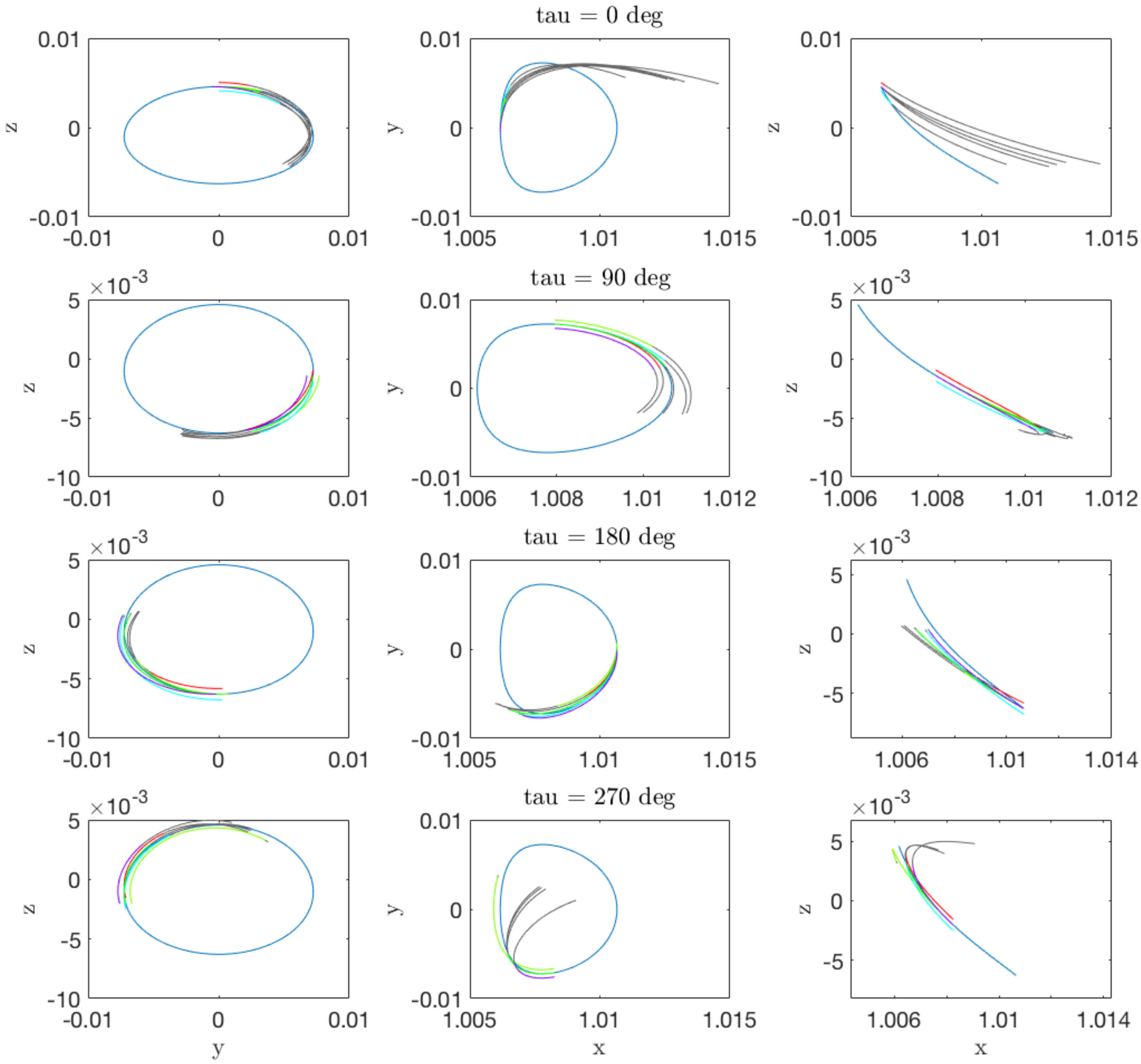

Figure 7.3: Three-dimensional visualization, using the alternate case, of the relation between location on where drift starts (τ) and the angle variation. The blue halo orbit represents the nominal Halo orbit. The colors used to represent the various Starshade configurations are consistent with the previous definitions. The black line represents positions where the Starshade configuration is outside the bounds of the angle constraints. The label has been omitted to aid in the visualization.

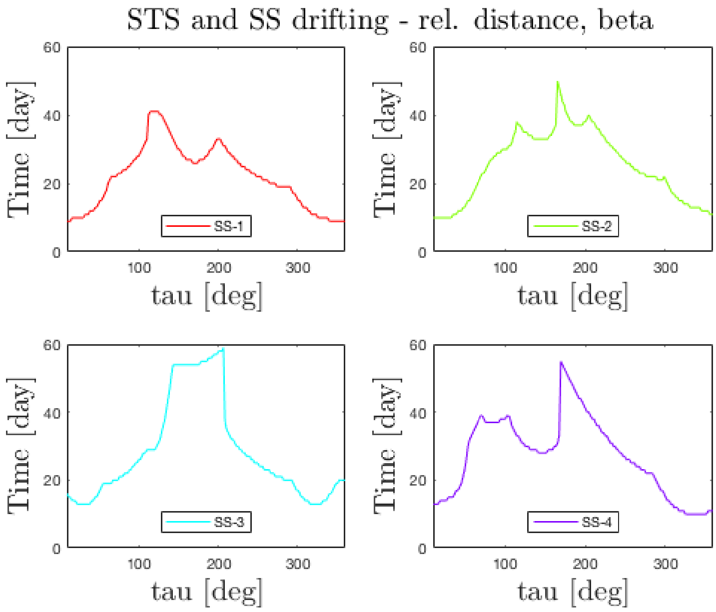

Figure 7.4: Superposition of the relative distance and angle constraint analysis for the case variation, where both NWO spacecraft drift simultaneously.

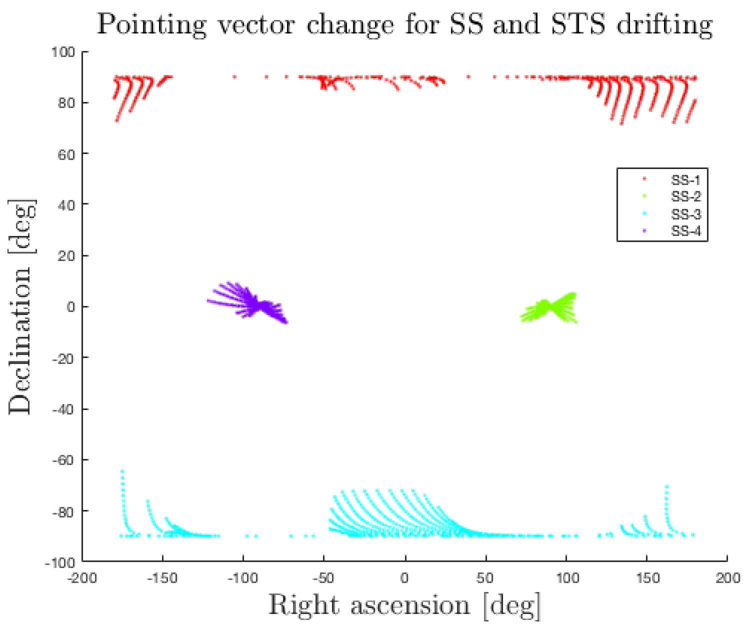

Figure 7.5: Pointing vector analysis in the case where both STS and S^3 drift simultaneously.

8

Constraint sensitivity analysis

In this section we shall analyze how sensitive our results are to the relative distance and angle constraint. The main reason to do this is to examine how a variation in the given constraints and therefore possibly in the overall NWO design might lead to a better use of the drift methodology. This analysis will be conducted for both the nominal case where only the S^3 drifts as well as for the alternative case where both the STS and the S^3 drift simultaneously. The variations that shall be analyzed are a change in relative distance between STS and S^3 from a nominal case of 20% to 10% and 30%. The change to the angle β constraint from the bounds of $-15°$ and $45°$ to two variations; namely $\pm 45°$ and $\pm 60°$.

8.1. Nominal case: Relative distance sensitivity

For the first case we compare the relative distance variation between 10%, 20% and 30% of the nominal relative distance for the nominal case. Figure 8.1 shows the results. The variance between the original setup of 20% to 30% show slight differences in the day that the system is allowed to drift before meeting a constraint, but these differences are not relevant enough to motivate a change of initial constraint value. For the constraint of 10% there is a considerable difference with respect to the setup of 20% that can lead to a decrease of around 10 days of available drift time. For this nominal the variation in nominal distance of 20%, instead of 10% and 30%, is therefore best trade-off choice.

8.2. Alternative case: Relative distance sensitivity

Next, we analyze the effect the same relative distance variations that have been analyzed for the nominal setup but applied to the alternative case. For this we make use of Figure 8.2. In this case the decrease of the relative constraint to 10% shows a change in the constraint plots for SS-1 and SS-3. The results for SS-2 and SS-4 are not affected by it. This is most likely due to the fact that SS-2 and SS-4 are more stable than then SS-1 and SS-3, since they are in the same orbital plane as the nominal Halo orbit. This means that they are also mathematically in a more stable orbit. On the other hand an increase from 20% to 30% has an affect on all four S^3 configurations.

8.3. Nominal case: Angle sensitivity

In this section we analyze Figure 8.3, where the angle variation from the nominal case in relation to two setups of $\pm 45°$ and $\pm 60°$. As expected the increase of the angle constraint shows an increase of the available days of drift. The main increase between $\pm 45°$ and $\pm 60°$ lies in the SS-2 configuration. All other configurations show a slight increase but not to the extent as SS-2.

8.4. Alternative case: Angle sensitivity

Using Figure 8.4 we see that this sensitivity shows essentially the same growth as in the previous section which was analyzing the nominal case, but with higher values for each configuration. A change of β of $\pm 60°$ would allow for a much higher range of drift days to be reached. It should be noted that the constraint of the relative distance should be analyzed in parallel to the angle constraint. Only the best combination of both will give the best case variation.

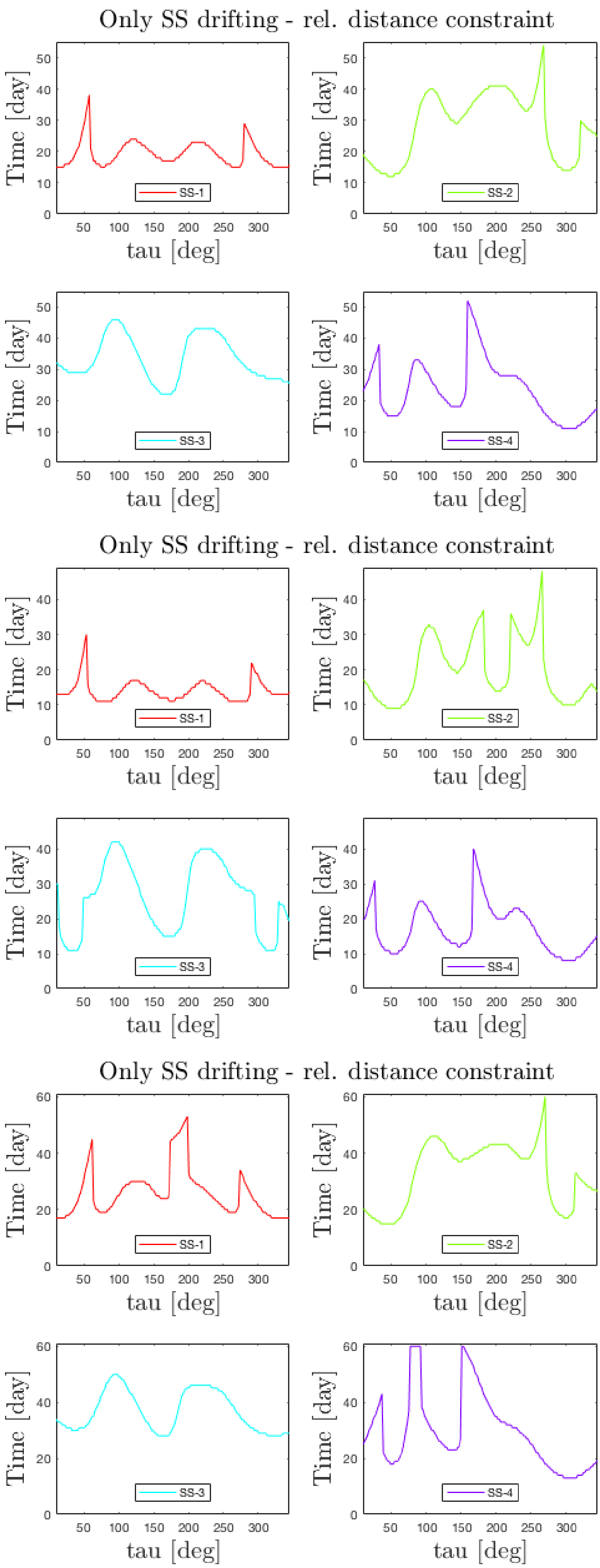

Figure 8.1: Sensitivity analysis of the relative distance for the nominal case. The top figure shows the nominal constraint setup of 20% of the relative distance. The middle figure shows the case of 10% and the bottom one for the nominal case using 30% of the relative distance.

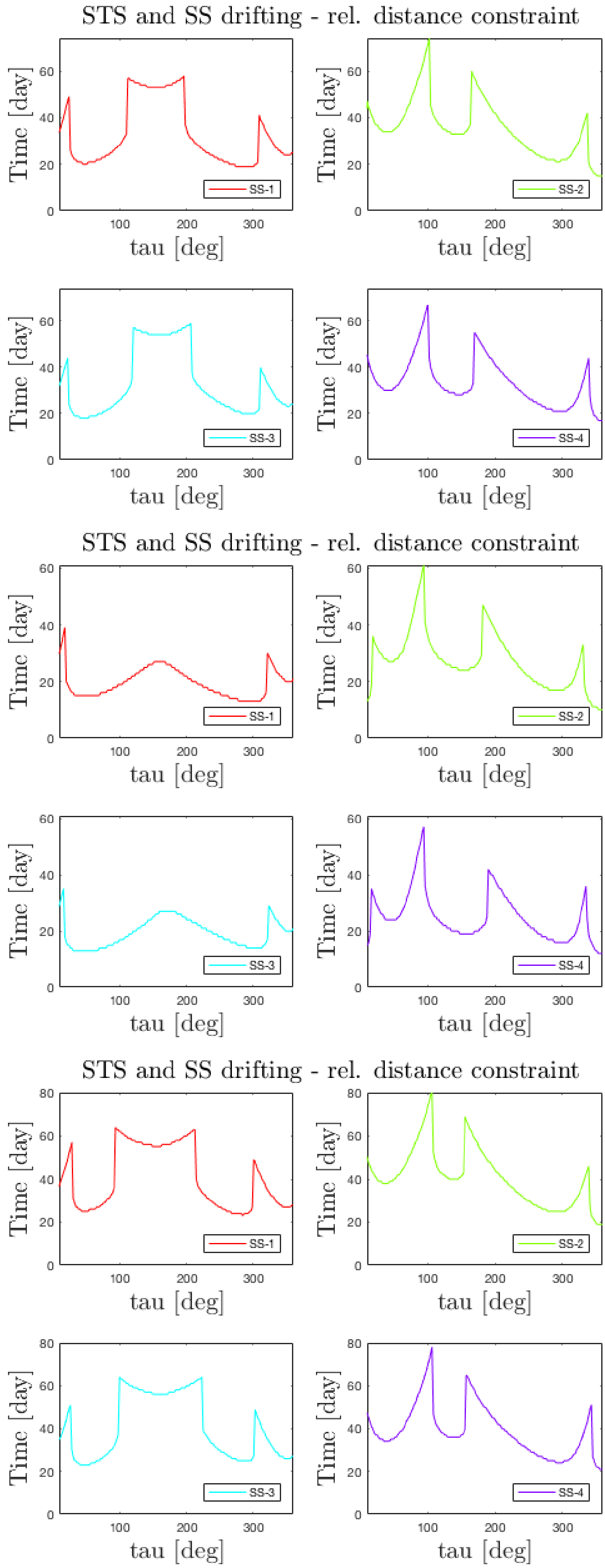

Figure 8.2: Sensitivity analysis of the relative distance for the alternative case. The top figure shows the alternative constraint setup of 20% of the relative distance. The middle figure shows the case of 10% and the bottom one for the alternative case using 30% of the relative distance.

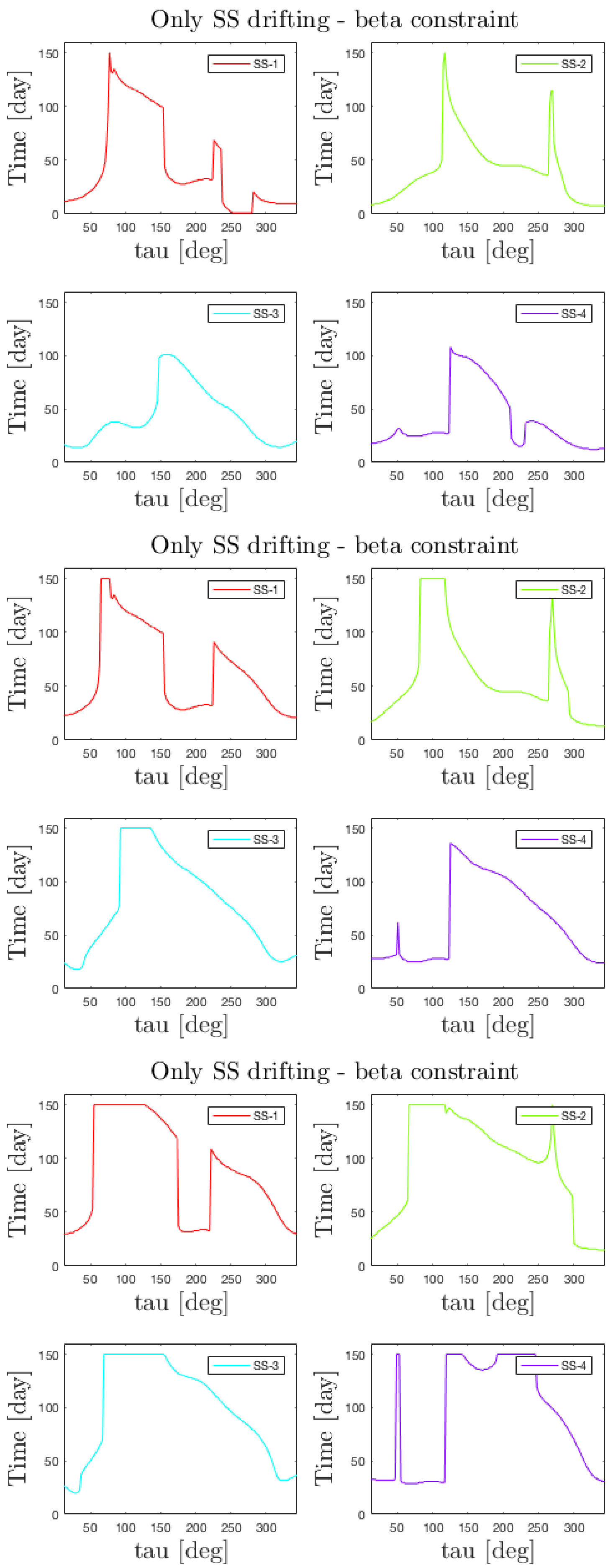

Figure 8.3: Sensitivity analysis of the angle β for a nominal case. The top four plots show the nominal setup of β between $-15°$ and $45°$. The middle four plots show the variation to an β constraint of $\pm 45°$, where as the bottom four plots use a value of $\pm 60°$.

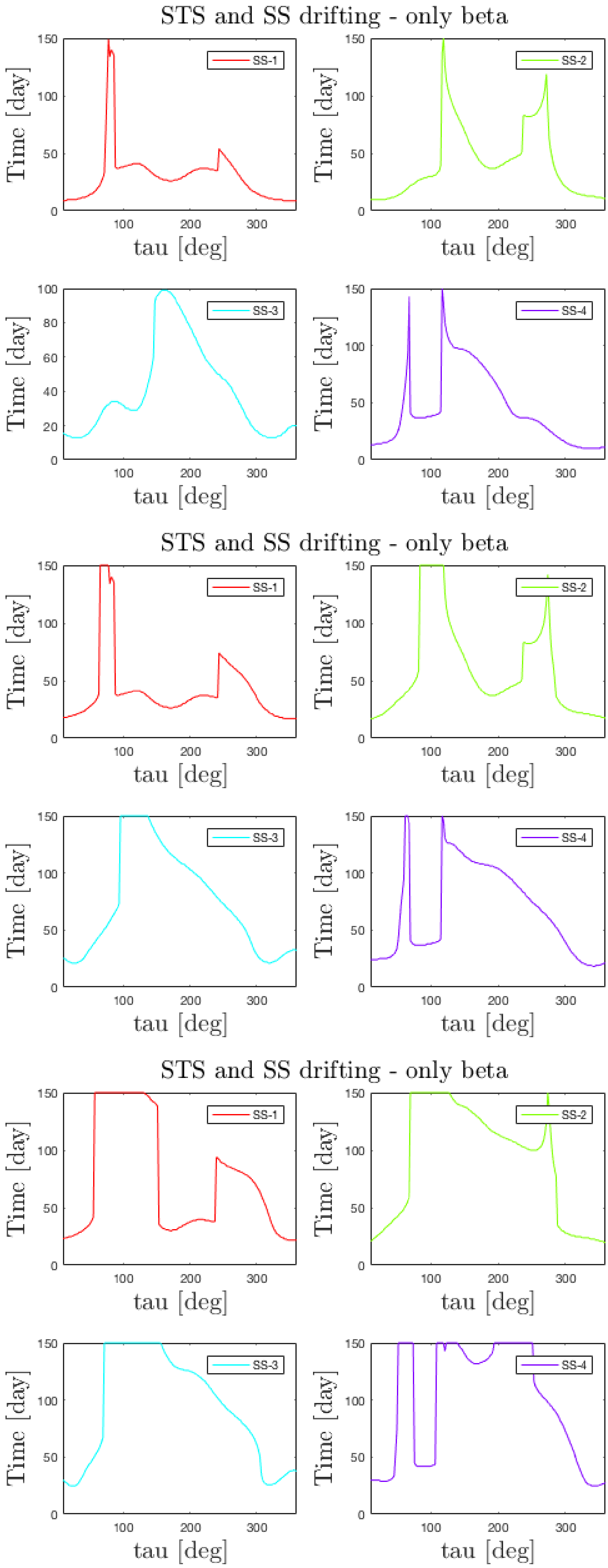

Figure 8.4: Sensitivity analysis of the angle β in the case where both NWO spacecraft drift simultaneously. The top four plots show the nominal setup of β between $-15°$ and $45°$. The middle four plots show the variation to an β constraint of $\pm 45°$, where as the bottom four plots use a value of $\pm 60°$.

8.5. NOMINAL CASE: POINTING VECTOR SENSITIVITY

For this section we look into the change in the pointing vector in relation to the changes in relative distance and β that have been described at the beginning of this section. Figures 8.5 and 8.6 show the pointing vector projected on the visual field that the NWO formation is pointing to. Observing Figure 8.5 shows the effects of the relative distance variations on the pointing vector and Figure 8.6 the effect of the change in β on the pointing vector. As the reader can already deduce from the previous sensitivity analysis the setups with 30% of the relative distance and the change in β of $\pm60°$ will show the greatest area of the field of view where NWO can move its pointing vector to. This same behavior can be seen in Figures 8.5 and 8.6. Due to the compactness of the spread of the pointing vector for the case of 30% of the relative distance, this is the most preferable configuration. This is especially the case since the configuration of β $\pm60°$ only allows to move the pointing vector in a few specific directions and not in between them.

8.6. ALTERNATIVE CASE: POINTING VECTOR SENSITIVITY

In this last subsection of the sensitivity analysis we analyze the variation of the pointing vector in relation to the relative distance and the angle beta for the case where both NWO spacecraft drift simultaneously. Observing Figure 8.7 we notice that for the case of 30% variation the pointing vector has reached its maximum coverage in right ascension and declination variance yet. It even made it possible for two configurations, (SS-3 and SS-4) to reach the same area of the plot. Unfortunately SS-1 and SS-3 do not reach as far as their counterpartner SS-2 and SS-4.
For the case of varying angle we make use of Figure 8.8. Here we see that both in the case of $\pm45°$ and $\pm60°$ specific setups of SS-2, SS-3 and SS-4 have a tendency to move the pointing vector towards the same area of the plot.

8.7. SKY COVERAGE

All pointing vector plots generated in the course of this thesis only cover a very limited area of the represented sky. So it is normal to wonder how this technique of free drift is supposed to cover the majority if not the whole visible sky. During the process of this thesis a simplified case has been assumed, in order to simplify the analysis. This assumption states that only four different possible Starshade locations shall be analyzed. In reality there are infinite possible locations where the Starshade can be located and still comply with the nominal setup, namely on any point on a circle around the telescope with radius of the nominal relative distance. If we increase the number of possible Starshade locations we see that depending on where on the sky the target star is located there is always an appropriate configuration that can reach that location. Since the origin of the pointing vector assumes a specific time the origin of the NWO pointing vector will move over time in the direction of the right ascension. Unfortunately this also means that not all stars are always available to be seen at any time. Therefore an element of scheduling needs to be introduced when designing the mission plan to go to from star to star. An example of what can be achieved using 32 Starshade configurations can be seen in Figure 8.9. Here we can see that the whole sky can be covered using a large amount of configurations. For this example we made use of the four configurations shown in Figure 4.5 with the addition of 28 additional configurations that are uniformly spread in between the four main configurations.

8.8. CONCLUSIONS

In conclusion we can say that the test case chosen has been crucial in understanding the (linear) dynamics that surround the Lagrangian environment. From the nominal case we have obtained an indication where the boundary is between the linear and the non-linear regime. Regarding the reachability of possible star targets using the nominal condition we see from Figure 6.10 that a variation on the constraints should be strongly considered in order to be able to reach all areas of the sky map. This has been shown in Section 8.7. Through the sensitivity analysis we have seen that slight variations can have a significant impact on the days of drift that are available before one of the constraints has been met. Depending on what the final mission design will be, this will surely have an impact on the feasibility of the drift method in order to change the pointing vector in an efficient way. This constraint analysis has shown that the drifting method can be applied to the given constraint, yet a variation of these will prove to be more fruitful for the drifting methodology. An inclusion of this study in an iterative redesign of NWO would allow for potentially a more extensive use of the drift method in the observation phase of the NWO mission design. From this extensive constraint analysis the next chapter shall introduce us on the ΔV required in order to return to the nominal Halo orbit.

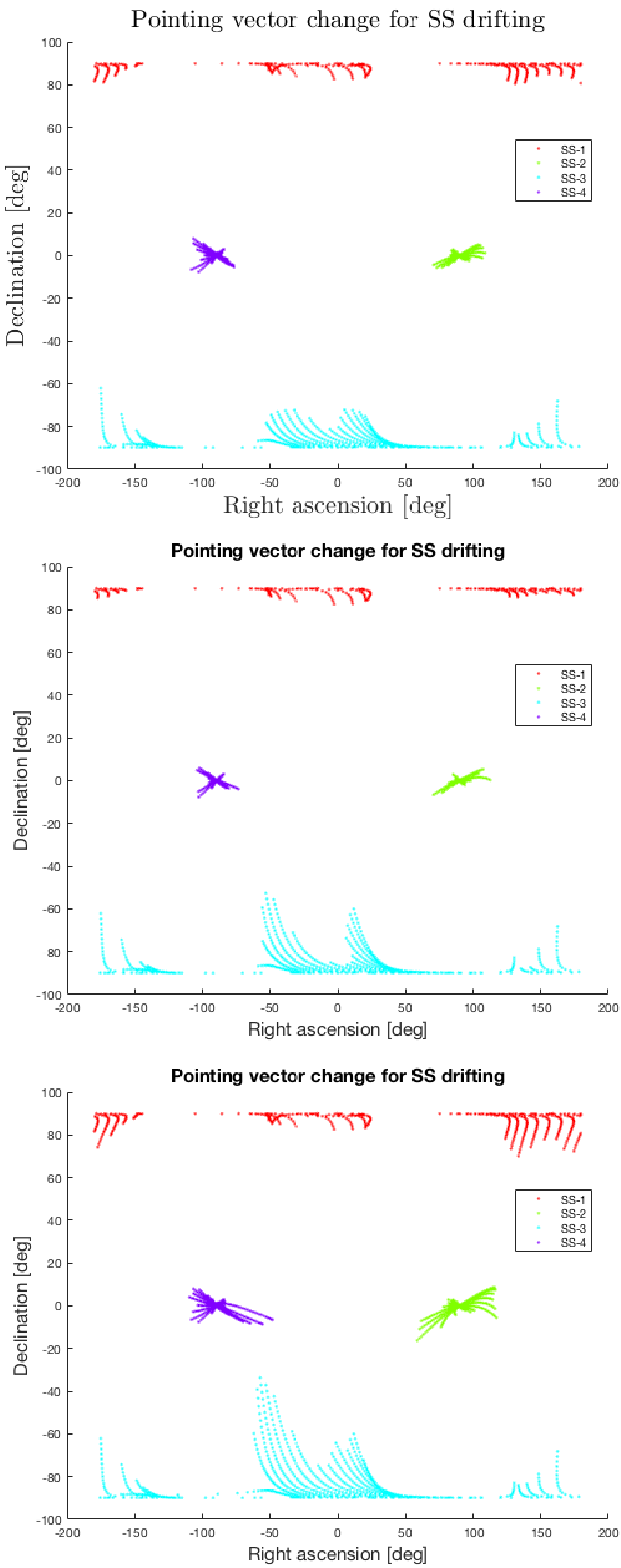

Figure 8.5: Sensitivity analysis of the pointing vector in relation to a varying relative distance between telescope and Starshade. The top figure shows the pointing vector behavior for a nominal relative distance constraint setup of 20%. The middle figure shows the case for 10% and the bottom one for the nominal case using 30% of the relative distance for the distance constraint.

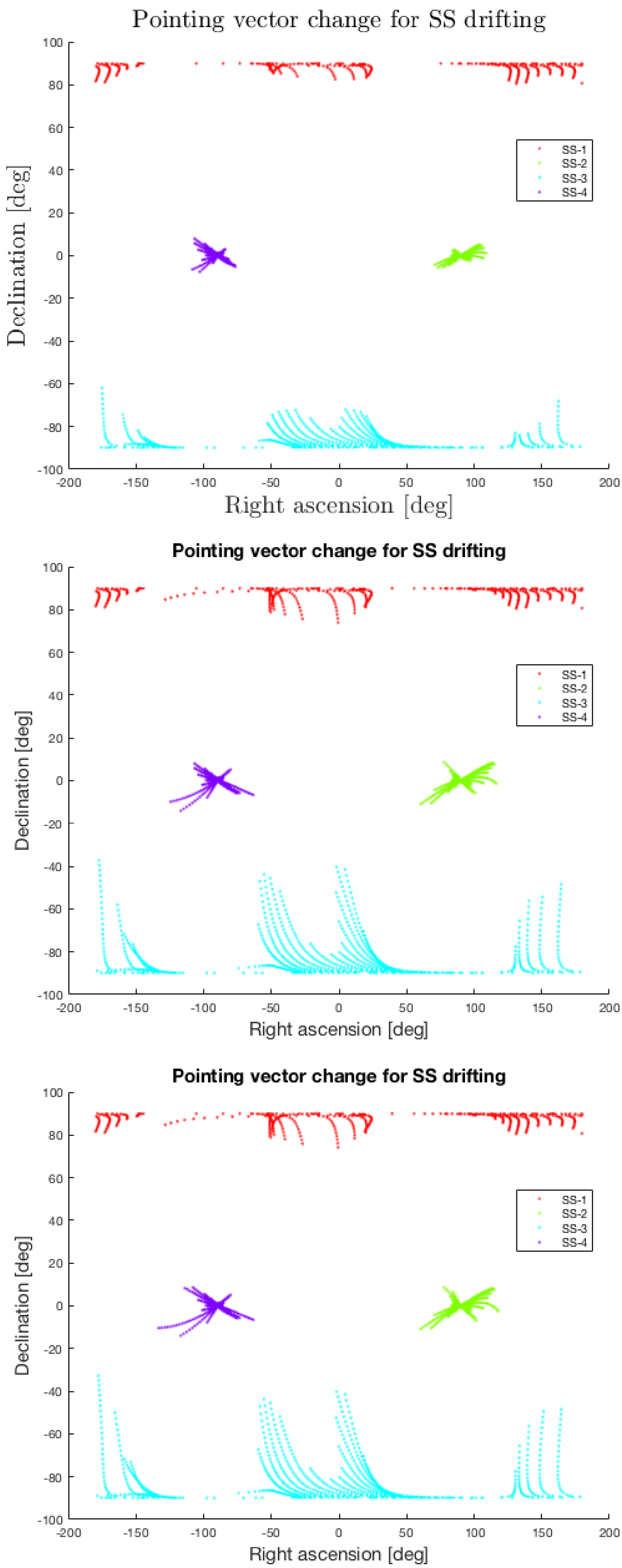

Figure 8.6: Sensitivity analysis for a nominal case of the pointing vector in relation to a varying angle β. The top plot show the pointing vector using the nominal setup for β of $-15°$ and $45°$. The middle plot shows the pointing vector variation making use of an β constraint of $\pm45°$, where as the bottom plot uses a value of $\pm60°$.

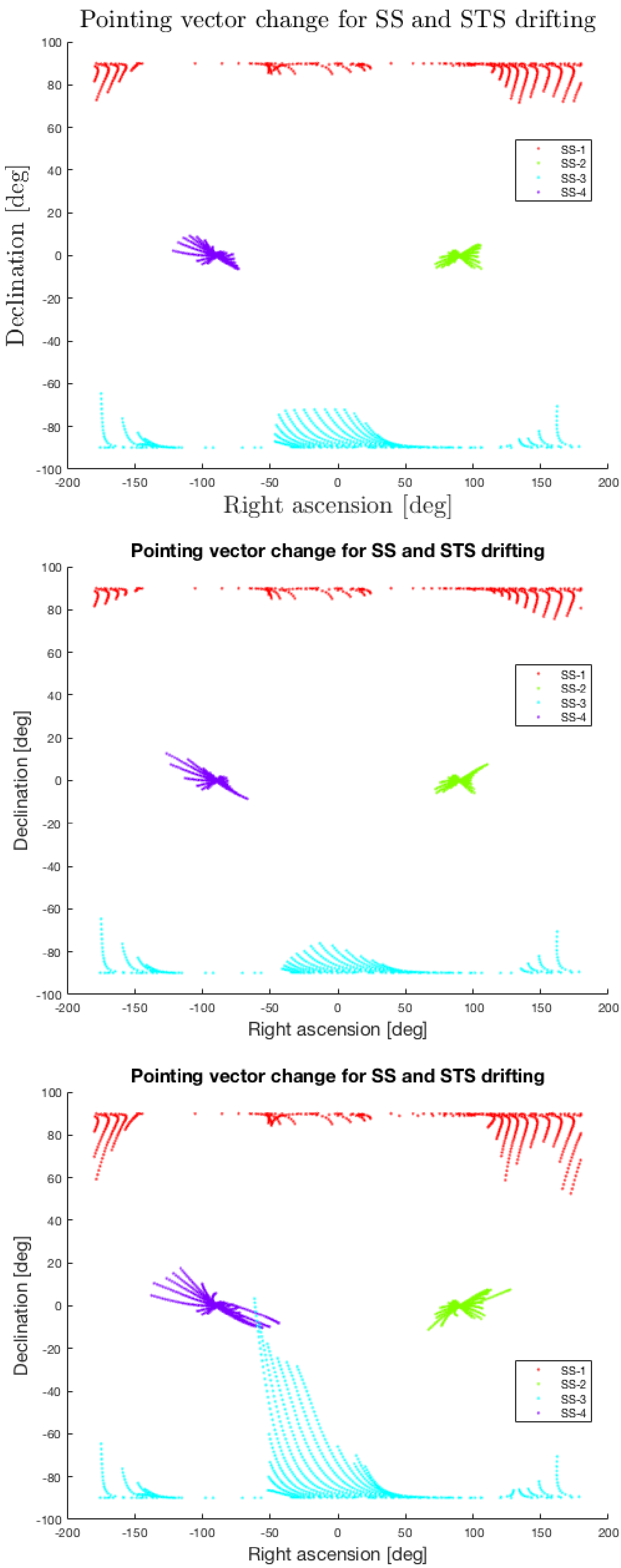

Figure 8.7: Sensitivity analysis of the pointing vector in relation to a varying relative distance between telescope and Starshade. The top figure shows the pointing vector behavior for an alternative relative distance constraint setup of 20%. The middle figure shows the case for 10% and the bottom one for the alternative case using 30% of the relative distance for the distance constraint.

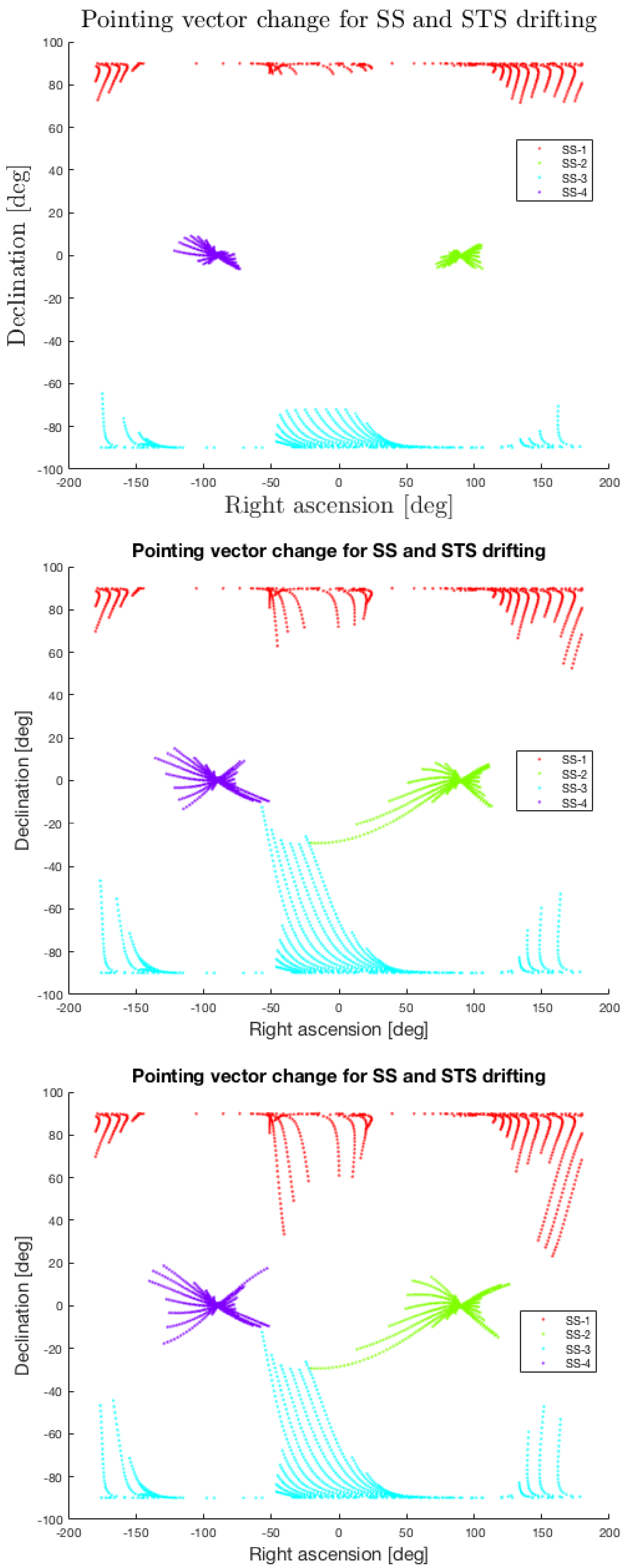

Figure 8.8: Sensitivity analysis for a alternative case of the pointing vector in relation to a varying angle β. The top plot show the pointing vector using the nominal setup for β of $-15°$ and $45°$. The middle plot shows the pointing vector variation making use of an β constraint of $\pm 45°$, where as the bottom plot uses a value of $\pm 60°$.

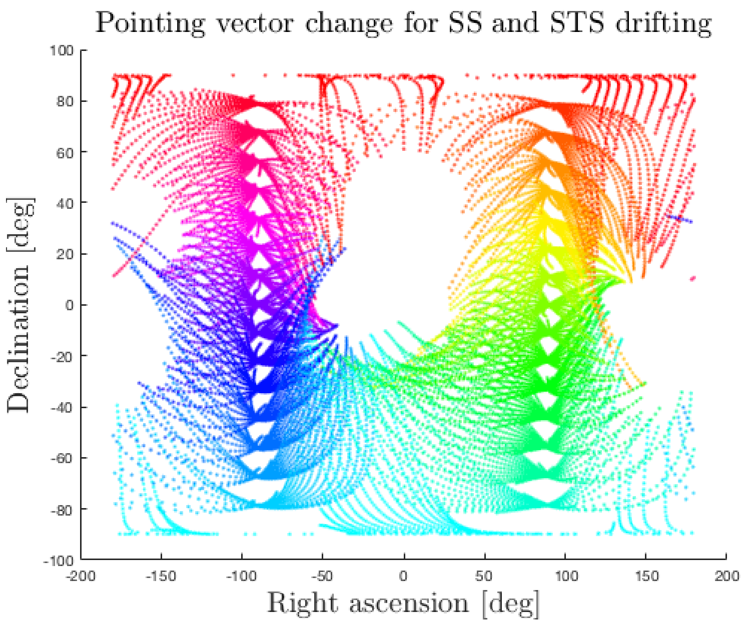

Figure 8.9: Pointing vector for the case of STS and S^3 drifting simultaneously with the distance relative distance constraint of 30% the nominal value of 70000 km and the angle β varying ±60 using 32 possible Starshade configurations. Each color represent a different configuration that uses an initial β of 0° and is uniformly distributed along a ring around the telescope, as as was done for the four configurations in Figure 4.5.

9

RETURN TRAJECTORY ANALYSIS

Section 4.3 gave an overview of the overall drift method, which is separated in two main sections. The first is the free drift arc. The drift behavior has been analyzed in chapters 5, 6 and 7. The second section is the controlled return trajectory back to the nominal Halo orbit. This second section is the focus of this chapter. For this return trajectory we make use of the differential correction algorithm described in Section 4.2 and the propagation method described in Section 4.3.1. This chapter concludes the results part of this body of work. Here the Δ V required to return to the nominal Halo trajectory shall be analyzed.

9.1. RETURN TIME

In Section 4.3 the time for the return trajectory has been selected as a first order assumption to be equal to the time used to drift away from the system. As can be seen from Figure 9.1 the value for ΔV_{min}, marked by a red star in the plot, varies only by 0.2E-5 between the timing variation selected. The white missing areas on the right side of the subplots (a) , (b) and (c) of Figure 9.1 are due to the single shooter not being able to have reached convergence. In order to analyse how a variation of the return travel time in comparison to the drift time would impact the subplot (a), we created two variations of the travel time due to the return trajectory varying 10 and 20 days in comparison to the drift time. The white area on the left of the subplots (b) and (c) origin in this addition of return travel time in comparison to the drift time. As it can be seen from Figure 9.1 an addition of extra days in the return trajectory increases also the time needed to return to the nominal Halo orbit for the case of ΔV_{min}. In the case of Figure 9.1(a) the return travel time for ΔV_{min} is equal to 21 days. For the cases of Figure 9.1(b) and (c) this increased to 26 and 30 days respectively. It should be noted that in Figure 9.1 (a) the range between zero and ten travel time is not black due to high values but to the proximity of the contour lines. A more in-depth visualization can be found in Section 9.2.

9.2. UNCONSTRAINED RETURN TRAJECTORY

In this section we will analyze the ΔV plots for the return trajectories of the STS and $\boldsymbol{S^3}$ without considering the constraints of relative distance and β. In Section 9.3 we will later on include these constraints for the nominal case.

The next step in the return trajectory analysis is the analysis of the unconstrained drift of the telescope and Starshade separately in relation to the values of ΔV reached in order to return to the nominal trajectory. This analysis has been done making use of the nominal values for relative distance and angle β described in Chapter 6. The telescope's unconstrained Δ V plot can be seen in Figure 9.2. Subplot (a) gives an overview of the overall Δ V required to return to the halo orbit. Subplots (b)-(d) show a close-up of various intervals in greater resolution between one day and five days for the return trajectory. The red cross marks the combination of τ to travel time where we find ΔV_{min} for the telescope. Subplot (b) to (d) show a linear regime, whereas subplot (a) shows that the border between linear and non-linear regime lies between 10 and 20 days. Next, we compute the ΔV plots for the nominal case for the four $\boldsymbol{S^3}$ configurations, again without considering the constraints of relative distance and β. The resulting plots can be seen in Figure 9.3. In these subplots we can see that any Δ V generated at higher values of around 10 days of travel time is not in a linear but much rather in a non-linear regime.

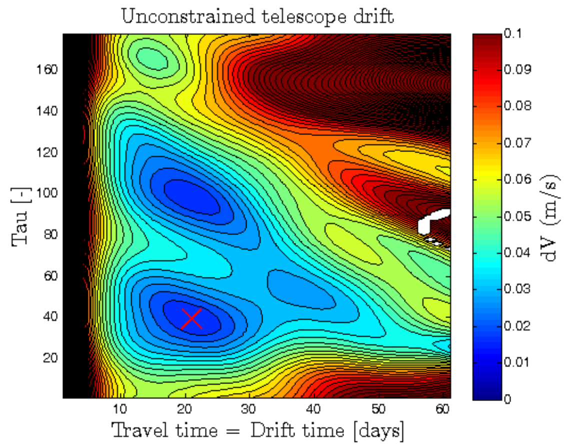

(a) ΔV_{min} = 1.62E-5 m/s

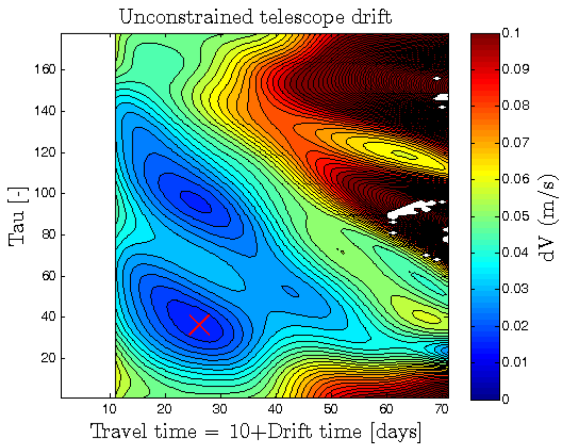

(b) ΔV_{min} = 1.43E-5 m/s

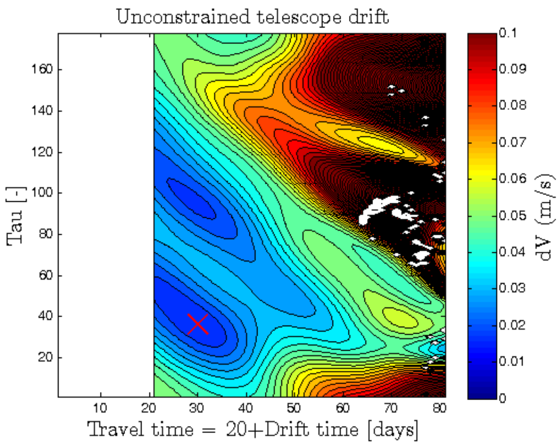

(c) ΔV_{min} = 1.61E-5 m/s

Figure 9.1: Timing variation for the return trajectory.

9.3. CONSTRAINED RETURN TRAJECTORY

For this section we shall analyze the constrained return trajectory. This means that we will apply the relative distance and β constraint using the nominal (S^3 only drifts) and alternate setup (both NWO satellites drift) that resulted from Chapter 6 and 7 to the unconstrained return trajectory in Section 9.2. This will act as a mask that is superpositioned on the Figures 9.2(a) and 9.3 giving the resulting ΔV plots for the return trajectory for both analyzed cases.

For the case where only the Starshade drifts, Figure 9.4 shows the ΔV necessary to return to the nominal trajectory and at what values of τ, travel and drift time as well as Starshade configuration that is an available option. The required ΔV to return from a Starshade-only drift depends on the specific case itself and can range between 0.01 and 0.1 m/s. In Figure 9.5 we can see the ΔV that are necessary to return the Starshade in the scenario where both NWO spacecraft drift as explained in the previous chapters. The range of ΔV required is very similar to the Starshade-only case. But we should not forget that in this alternative case the telescope drifts too.
This means that to the values of ΔV in Figure 9.5 we need to add the ΔV in Figure 9.2 to get the ΔV needed for the case where both NWO spacecraft drift. Additionally, we need to add at least another 50% to the total ΔV as a safety factor. This is where the trade-off starts. On one hand we have the nominal configuration that is easier to control since only one spacecraft drifts and uses less ΔV, but on the other hand its pointing vector is also less free in its movement than the alternative case with both spacecraft drifting, see Figures 6.10 and 7.5. It should also be noted that the case where both NWO spacecraft drift simultaneously allows for a higher number of days of possible drift overall.

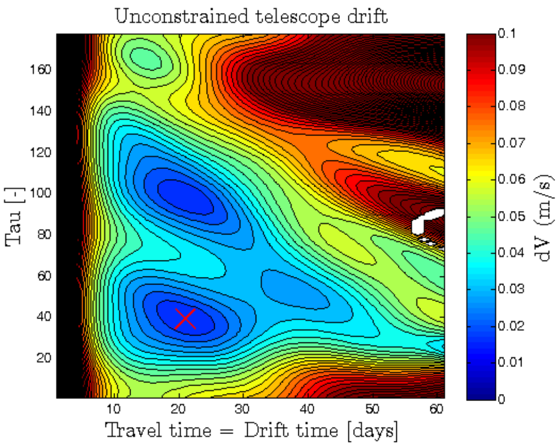

(a) Overview of the whole time period

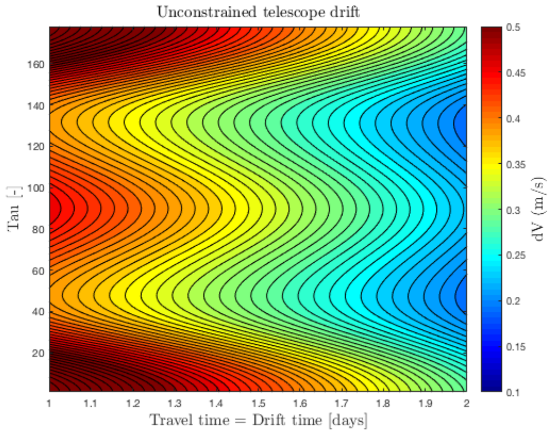

(b) Close-up of the interval between 1 and 2 days

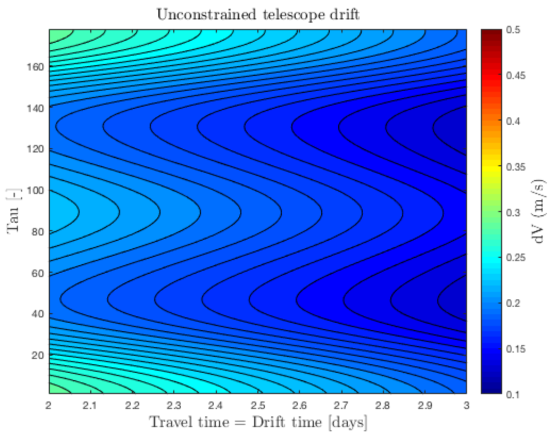

(c) Close-up of the interval between 2 and 3 days

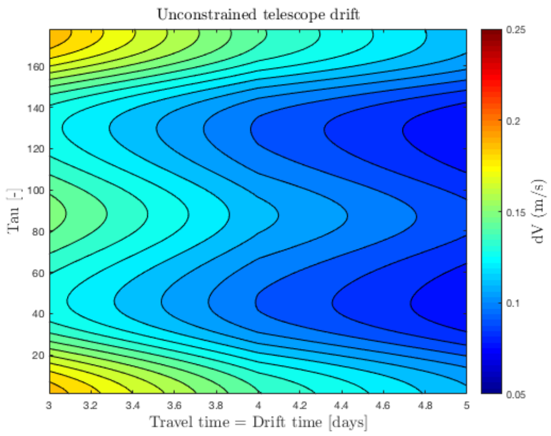

(d) Close-up of the interval between 3 and 5 days

Figure 9.2: Δ V required to return to nominal orbit for the nominal case where only STS uses the drift method.

9.3.1. COMPARISON TO PRELIMINARY STUDY

Table 9.1 shows a preliminary budget originating for a concept study that did not consider the use of free drift. This mission design was designed to use an average ΔV of 142.8 m/s per target for a mission lifetime of 10 years. Using free drift we can, if the geometry and timing allow it, target a variety of stars using for a fraction of the same ΔV for a longer mission lifetime.

Table 9.1: Preliminary ΔV budget for the S^3. [7]

NWO-2 S³ DELTA-V BUDGET (Chemical)					
	Maneuver	Delta V (m/s)	ACS Tax	Margin	Effective ΔV (m/s)
1	Launch Window	0.0	0.0%	0.0%	0.0
2	Mid-Course Correction (MCC) #1	30.0	0.0%	30.0%	39.0
3	Mid-Course Correction (MCC) #2	3.0	0.0%	30.0%	3.9
4	L2 Injection & Attitude Slew, phase w/ STS	71.0	0.0%	30.0%	92.3
5	Target Station-keeping (Orbit & Pointing)	142.8	0.0%	30.0%	185.7
6	Momentum Unloading	14.2	0.0%	30.0%	18.5
	Total Delta-V Budget	261.0	0.0%	30.0%	**339.4**

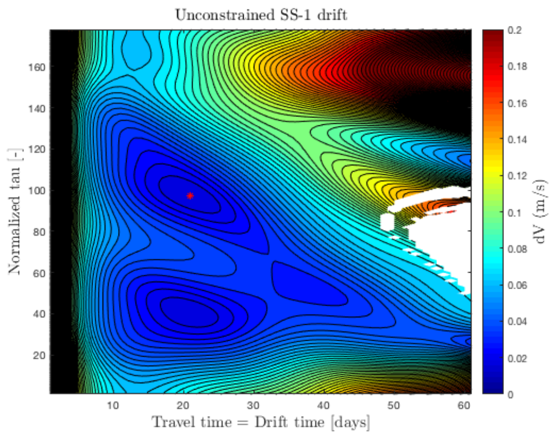

(a) SS-1

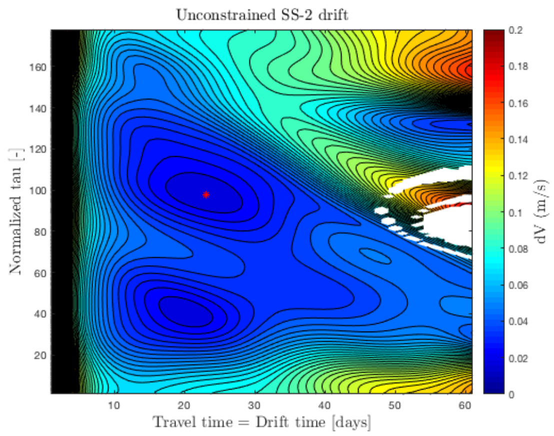

(b) SS-2

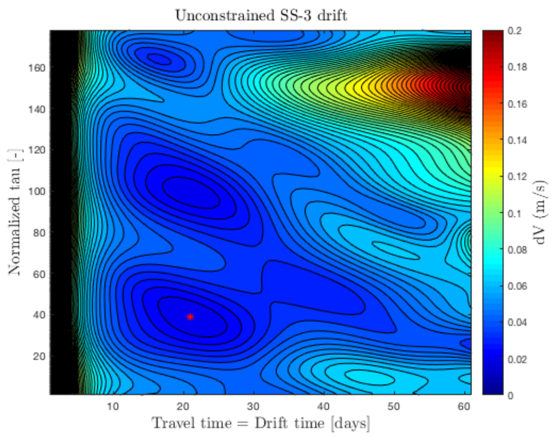

(c) SS-3

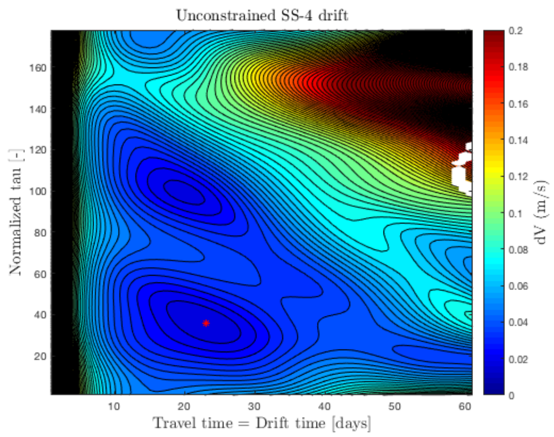

(d) SS-4

Figure 9.3: Δ V required to return to nominal orbit for the nominal case where only S^3 uses the drift method.

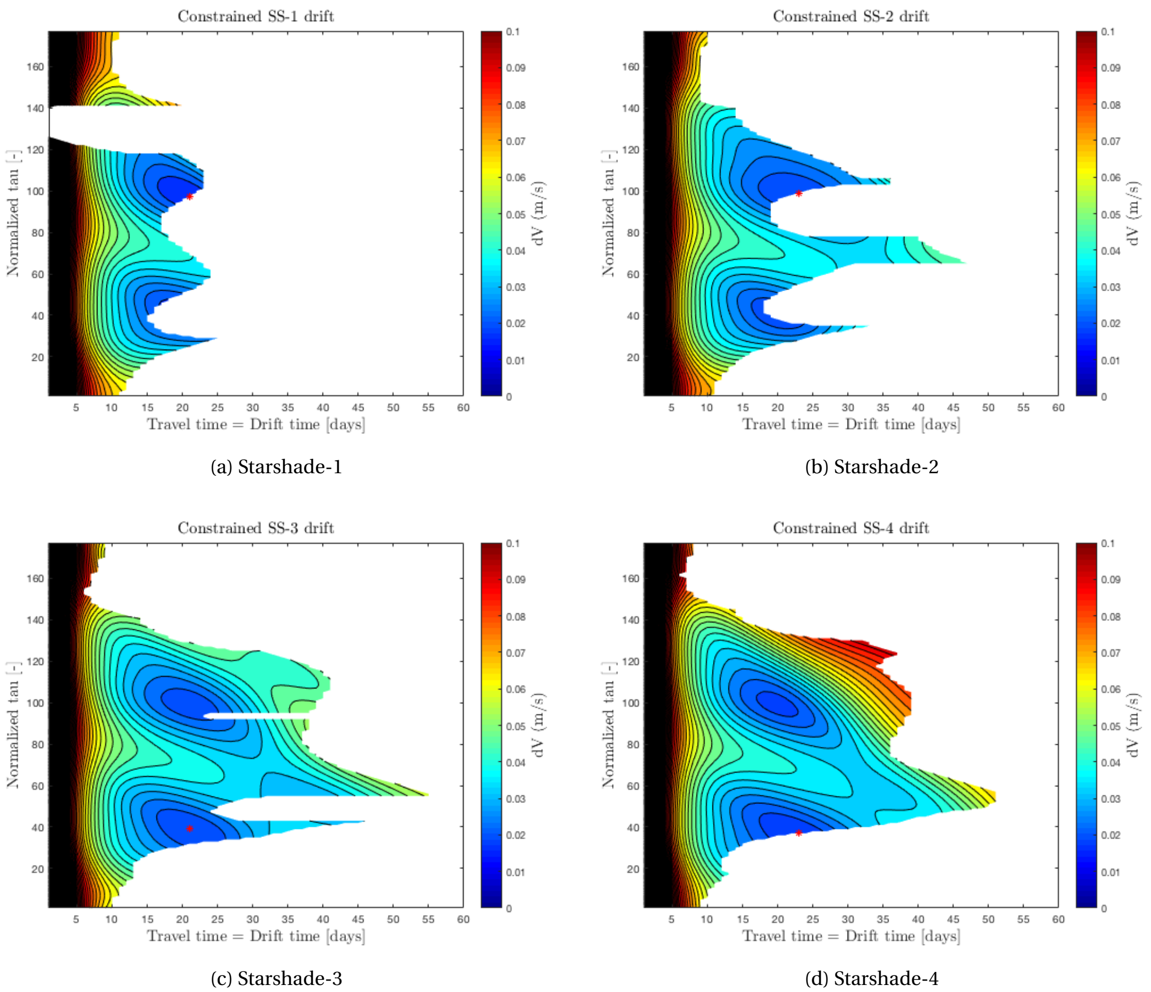

(a) Starshade-1

(b) Starshade-2

(c) Starshade-3

(d) Starshade-4

Figure 9.4: Δ V required to return to nominal orbit for the case where the Starshade drifts only and the overall constraint is applied.

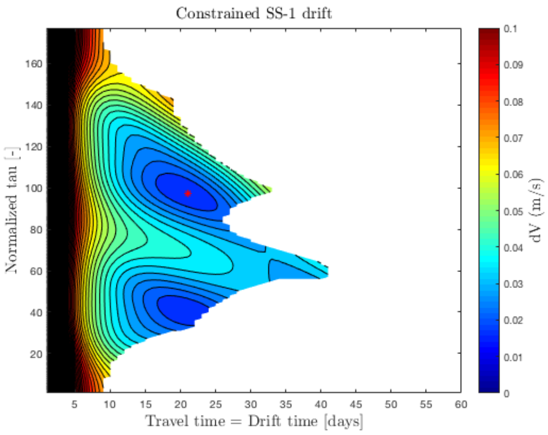

(a) Starshade-1

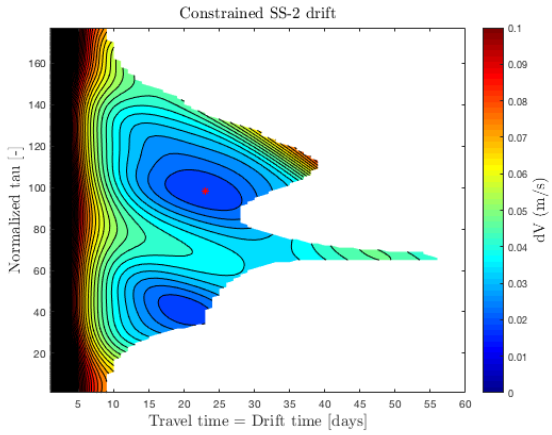

(b) Starshade-2

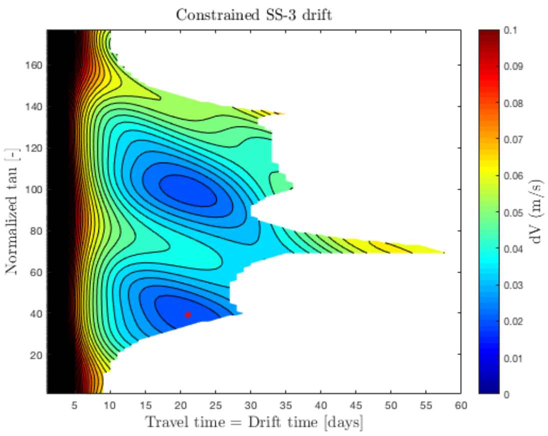

(c) Starshade-3

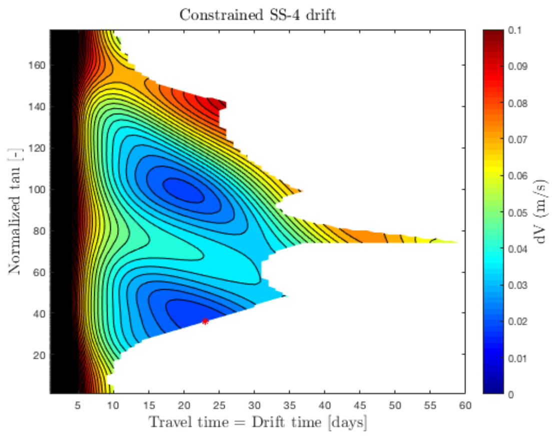

(d) Starshade-4

Figure 9.5: Δ V required to return to nominal orbit for the case where both the Starshade and the telescope drift simultaneously and the overall constraint is applied.

10

CONCLUSIONS AND RECOMMENDATIONS

As part of this conclusion let us remember the research questions that lead to this body of work.

"Can the dynamical environment of a lagrangian point be used to redirect the pointing vector of the NWO in order to aid in its operation during its observation campaign?"

As we have seen in Chapters 6 and 7, the dynamical environment around SE-L2 could indeed be successfully used to redirect the pointing vector of NWO in order to aid in its observation campaign. A small change in its constraints or relative distance and angle β, as shown in Chapter 8 could even improve that same capability. This being said this ability comes with its drawbacks. The main one being that this drift methodology is dependent on the geometry of the pointing vector of the NWO satellites at a specific moment in time. This means that even though all stars can be reached using the drift method, as shown in Figure 8.9, this does not mean that all stars can be reached at any time during the mission duration. This constraint follows from the duration that it takes for the SE-L2 point to rotate around the Sun. In one orbital period of the Halo, which is approximately six months, all stars can be seen at least once by NWO using the drift method using at least four $\boldsymbol{S^3}$ configurations. If a list of stars that NWO should visit are known beforehand, this scheduling issue can be included in an optimization problem in order to visit the given set of target stars.
In conlcusion we can say that non-linear dynamics can be used as a part of the NWO mission proposal or any other formation flying mission around a Lagrangian point. The end of each research question leads to always new questions and paths that need to be explored. This has been definitely been the case for this thesis. Some of the points that should be explored further in detail are:

- Analytic analysis of the behaviour of the artificial SS orbits. This would allow for a deeper understanding on how specific parameters are dependent on each other.
- Characterize the boundary between the linear and non-linear regime. This would give a clear division on where the linear regime begins and the non-linear starts. This could be useful in case one would have a different mission architecture that requires to stay only within the linear regime.
- Integrate the drift approach as part of an optimization problem to decrease mission time, propellant consumption or extend mission lifetime.
- Include a more accurate SRP model that is not based on the cannonball model [33]. This model is based on a spherical satellite. The shape of the Starshade is far from spherical. An improvement of this model would give a higher realism to the NWO simulations.
- Include solar sail capabilities in the mission design. This addition could allow to use the shape of the Starshade to manuever both during drifting as well as during the return trajectory to the nominal Halo orbit leading to potentially an additional decrease of ΔV and therefore an increase mission duration.
- Applicability for other formation flying mission around Lagrangian points
- Study techniques to remain aimed at a specific target for multiple days of observation, within the 1 m constraint described in Section 2.4.3.

- Optimize the NWO configuration using a redesign of both spacecraft by merging both spacecraft into one. In this case the satellite would function as both a telescope and an occulter at the same time. Multiple such spacecraft would decrease the scheduling problem drastically.

Last but definitely not least, it should be mentioned that the use of non-linear dynamics has never been used during mission operations and would need extensive experimental and operational testing during a possible precursor mission.
These are only a few of the research paths that can be taken. There are mostlikely many more that are not visible at first glance, but the provided list provides the interested reader with a good start to continue the research in an area that is fascinating and has yet been fully researched.

BIBLIOGRAPHY

[1] P. J. Mohr, D. B. Newell, and B. N. Taylor, *CODATA recommended values of the fundamental physical constants: 2014,* Journal of Physical and Chemical Reference Data **45**, 043102 (2016).

[2] P. K. Seidelmann, *Explanatory supplement to the astronomical almanac* (University Science Books, 2005).

[3] J. Rodriguez, *Flower power: NASA reveals spring starshade animation,* (2014), http://planetquest.jpl.nasa.gov/video/15, accessed: March 1, 2017.

[4] I. De Pater and J. J. Lissauer, *Planetary sciences* (Cambridge University Press, 2015).

[5] A. Sandberg and L. Betz, *Probing seven promising worlds with NASA's James Webb Space Telescope,* (2017), https://exoplanets.nasa.gov/news/1422/probing-seven-promising-worlds-with-nasas-james-webb-space-telescope/, accessed: March 1, 2017.

[6] J. Demarines, W. Cash, P. Oakley, and G. Arney, *Detecting biosignatures in an evolving earth-like atmosphere via new worlds observer,* in *AGU Fall Meeting Abstracts* (2008).

[7] W. Cash, S. Kendrick, C. Noecker, J. Bally, J. DeMarines, J. Green, P. Oakley, A. Shipley, S. Benson, S. Oleson, D. Content, D. Folta, S. Garrison, K. Gendreau, K. Hartman, J. Howard, T. Hyde, D. Lakins, J. Leitner, D. Leviton, R. Luquette, B. Oegerley, K. Richon, A. Roberge, S. Tompkins, J. Tveekrem, B. Woodgate, M. Turnbull, D. Dailey, K. Decker, R. Dehmohseni, B. Gaughs, T. Glassman, M. Haney, R. Hejal, C. Lillie, A. Lo, D. O'Conner, G. Oleas, R. Polidan, R. Samuele, S. Shields, J. Shirvanian, D. SooHoo, G. Tinetti, B. Dorland, R. Dudik, R. Gaume, and B. Mason, *The New Worlds Observer: the astrophysics strategic mission concept study,* in *UV/Optical/IR Space Telescopes: Innovative Technologies and Concepts IV Howard A. MacEwen; James B. Breckinridge* (San Diego, CA, August 26, 2009) dOI:10.1117/12.827486.

[8] A. Wolszczan, *Discovery of pulsar planets,* New Astronomy Reviews **56**, 2 (2012).

[9] NASA Exoplanet Archive, *Exoplanet plots,* http://exoplanetarchive.ipac.caltech.edu/ exoplanetplots/, accessed: March 1, 2017.

[10] M. Mayor, C. Lovis, and N. C. Santos, *Doppler spectroscopy as a path to the detection of earth-like planets,* Nature **513**, 328 (2014).

[11] L. Spitzer, *The beginnings and future of space astronomy,* American Scientist **50**, 473 (1962).

[12] C. J. Copi and G. D. Starkman, *The big occulting steerable satellite (BOSS),* The Astrophysical Journal **532**, 581 (2000).

[13] W. Cash, *Detection of earth-like planets around nearby stars using a petal-shaped occulter,* Nature **442**, 51 (2006).

[14] W. Cash, J. Kasdin, S. Seager, and J. Arenberg, *Direct studies of exo-planets with the New Worlds Observer,* in *Optics & Photonics 2005* (International Society for Optics and Photonics, 2005) pp. 58990S–58990S.

[15] J. Kasting, D. Whittet, and W. Sheldon, *The effect of ultraviolet radiation on planetary habitability,* in *Lunar and Planetary Science Conference*, Vol. 27 (1996) p. 655.

[16] W. Cash, S. Kendrick, C. Noecker, J. Bally, J. Demarines, J. Green, P. Oakley, A. Shipley, S. Benson, S. Oleson, *et al.*, *The New Worlds Observer: the astrophysics strategic mission concept study,* in *SPIE Optical Engineering+ Applications* (International Society for Optics and Photonics, 2009) pp. 743606–743606.

[17] J. Binney and S. Tremaine, *Galactic dynamics* (Princeton university press, 2011).

[18] Cash, W and NWO Team et al., *Detailed Spectroscopy of Exoplanets Using the New Worlds Observer,* in *Molecules in the Atmospheres of Extrasolar Planets*, Vol. 450 (2011) p. 209.

[19] K. Wakker, *Fundamentals of astrodynamics,* Delft University of Technology, University Lecture Notes, Delft Repository (2015).

[20] J. S. Parker and R. L. Anderson, *Low-energy lunar trajectory design* (John Wiley & Sons, 2014).

[21] K. Davis, *Interplanetary mission design,* University of Colorado Boulder, University Lecture Slides (2015).

[22] R. W. Farquhar, *The control and use of libration-point satellites,* National Aeronautics and Space Administration Technical Report (1970).

[23] R. W. Farquhar and A. A. Kamel, *Quasi-periodic orbits about the translunar libration point,* Celestial Mechanics **7**, 458 (1973).

[24] D. L. Richardson, *Analytic construction of periodic orbits about the collinear points,* Celestial Mechanics **22**, 241 (1980).

[25] D. L. Richardson, *Halo orbit formulation for the ISEE-3 mission,* Journal of Guidance, Control, and Dynamics **3**, 543 (1980).

[26] National Aeronautics and Space Administration, *ISEE-3/ICE Gallery,* (March 1, 2017), https://heasarc.gsfc.nasa.gov/docs /heasarc/missions/images/isee3images.html, accessed: February 1, 2017.

[27] D. Viswanath, *The Lindstedt–Poincaré Technique as an Algorithm for Computing Periodic Orbits,* SIAM review **43**, 478 (2001).

[28] J. S. Parker and R. L. Anderson, *Low-energy lunar trajectory design,* Pasadena: Jet Propulsion Laboratory (2013).

[29] K. C. Howell, *Three-dimensional, periodic,'halo'orbits,* Celestial Mechanics **32**, 53 (1984).

[30] O. Montenbruck and E. Gill, *Satellite Orbits: Models, Methods and Applications* (Springer, Berlin, 2001).

[31] C. M. A. Deccia, *Designing an induced asteroid collision,* (2017), Literature study, Delft University of Technology.

[32] C. M. A. Deccia, E. Villalba, J. S. Parker, W. Cash, G. H. Born, and R. Noomen, *Surfing the L2 gradient with the Starshade in search of extraterrestrial life,* in *AIAA/AAS Astrodynamics Specialist Conference* (2016) p. 5666.

[33] D. Vokrouhlicky, P. Farinella, and F. Mignard, *Solar radiation pressure perturbations for earth satellites ii. an approximate method to model penumbra transitions and their long-term orbital effects on lageos,* Astronomy and Astrophysics **285** (1994).